Supramolecular nanomotors for biomedical applications

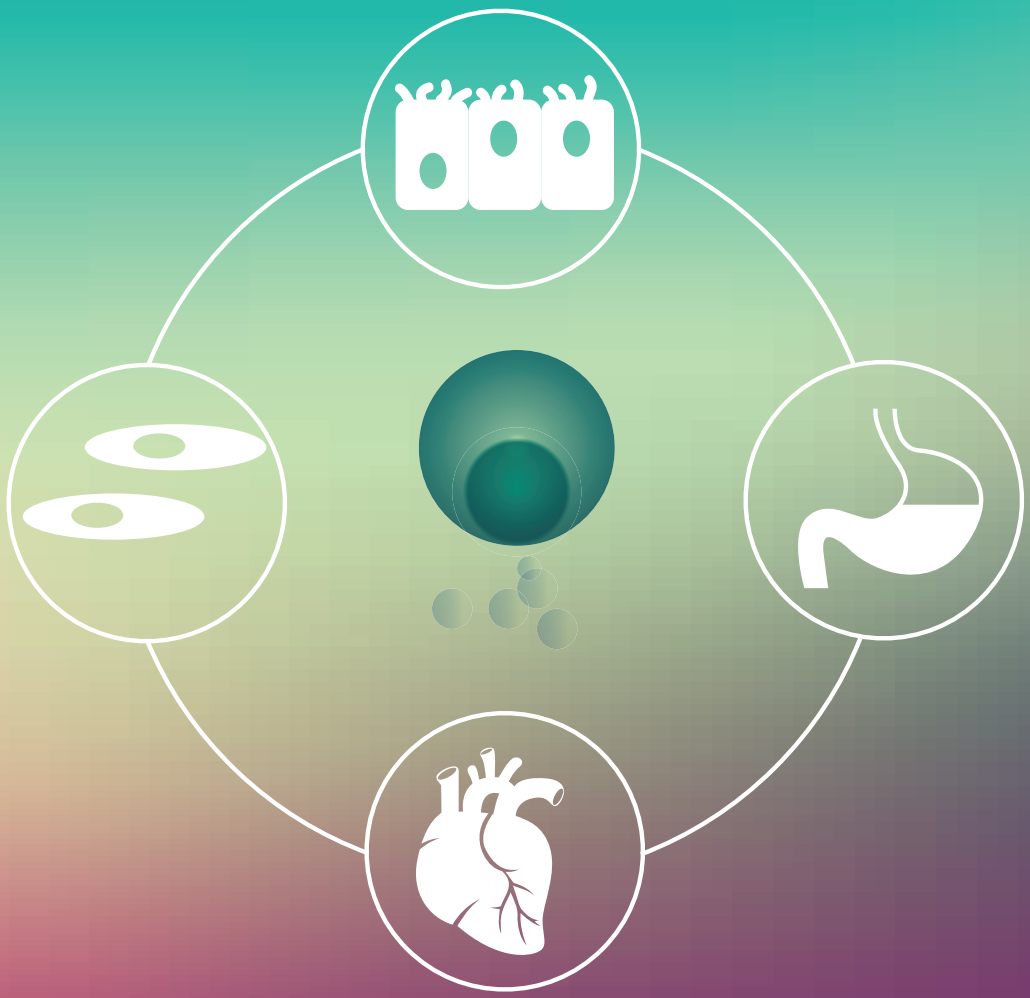

Fei Peng

SUPRAMOLECULAR NANOMOTORS FOR BIOMEDICAL APPLICATIONS

ISBN/EAN: 978-94-92679-05-5
Layout and printing: Print Service Ede

Supramolecular nanomotors for biomedical applications

PROEFSCHRIFT
ter verkrijging van de graad van doctor
aan de Radboud Universiteit Nijmegen
op gezag van de rector magnificus prof. dr. J.H.J.M. van Krieken,
volgens besluit van het college van decanen
in het openbaar te verdedigen

op donderdag 15 juni 2017
om 16.30 uur precies

door
Fei Peng
geboren op 21 november 1988
te Hengyang (China)

Promotoren
Prof. dr. D. A. Wilson
Prof. dr. J. C. M. van Hest

Manuscriptcommissie
Prof. dr. R. J. M. Nolte
Prof. dr. J. J. L. M. Cornelissen (Universiteit Twente)
Prof. dr. A. Cambi

Paranimfen
Yingfeng Tu
Min Bao

Table of contents

1 Micro/nanomotors towards in vivo application

This chapter has been accepted for publication:
F. Peng, Y. F. Tu, D. A. Wilson, *Chem. Soc. Rev.*, 2017, accepted.

1.1. INTRODUCTION

In nature, highly efficient biological motors perform complicated tasks by converting fuel, typically adenosine triphosphate (ATP), into mechanical motion.[1] These natural motors are involved in almost every aspect of cell life including division, growth and migration.[2] Inspired by this and in an attempt to realize controlled manipulation at micro/nano/molecular regime, scientists from multiple disciplines have focused their research enthusiasm on developing miniaturized motors. For controlled motion at a molecular level, sophisticated molecular machines with complex structures, such as molecular cars and molecular elevators have been engineered.[3] These interesting studies and their profound application potential have been warranted with a Nobel prize for chemistry in 2016. To achieve motion at nanometer or micrometer scale, profound efforts have been devoted and interesting advances are being made. Early works include the integration of natural motors with synthetic components. Montemagno's team integrated biomolecular motor F1-ATPase enzyme with nickel rod nanopropeller.[4] The F1-ATPase enzyme was found to convert ATP into rotary toque. Then a centimeter sized synthetic motor prototype was devised by Whitesides' group in 2002. [5] The motor comprised of a poly(dimethylsiloxane) (PDMS) plate with integrated platinum coated glass. By decomposing hydrogen peroxide into oxygen gas, thrust was generated and the motor was pushed forward. After that scientists at Pennsylvania State University proposed to shrink the size of motors to micron scale.[6] Other interesting systems include the one engineered by Zettl's team.[7] They attached a metal plate rotor to a multi-walled carbon nanotube. The nanotube was anchored to a supporting pad, which were both conductive. With applied voltage, the metal plate demonstrated controlled rotation. These works were quickly followed by development of various synthetic micro[8]/nanomotors[9] based on different materials[10] and different shapes (tube,[11] Janus sphere[8] and irregular[12]). These artificial machines converted external fuel into movement including rotation[13] and shuttling[14] at micro- or nanometer scale, promising microscopic transportation in an efficient and effective manner. To further improve the cargo transporting abilities[15] and expand applications [16] of the micro/nanoswimmers, last decade has witnessed substantial efforts devoted to explore diverse fabrication methods[17]/fuels[18]/control methods[19] as well as to gain in-depth understanding of the propulsion mechanisms.[20] For instance, early metal based motors were in general produced with a non-assembling approach, which was usually limited by material choice, complicated instrumentation and output. In 2012 Wilson/Van Hest *et al*[21] and He's team[22] pioneered the motor fabrication with assembling approach. The versatile approach makes it feasible for large scale motor production, easy motor functionalization and readily cargo loading.[23] With regard to fuel source, the input energy for motors now is not only limited to chemical fuel hydrogen peroxide.[24] Hydrogen peroxide is a common fuel for early catalytic metal based motors yet it may present oxidative pressure on environment. In addition in biological media hydrogen peroxide is found at relatively

low concentrations. For catalytic motors, more biocompatible energy source including glucose,[25] urea[16a, 26] and even water[27] were recently introduced. For motors that utilize the energy from external environment, light, magnetic, ultrasound and electric field are all great options.[28] The external factors including light,[29] magnetic field,[30] topography[31] and temperature[32] etc can also be used as stimulus to achieve movement control.

With these advances, motors demonstrate tremendous potential to revolutionize various fields including environmental remediation,[33] battery[34] and transportation of cargos.[35] Extending the application of the motor systems and translating initial proof-of-concept research into realistic practice has become a central issue for researchers in the field. Biomedical application *in vivo*, a major concern for general people, has been and continues to be a strong research interest. Motors with strong towing power and functionalities promise to be highly attractive platforms for addressing complicated *in vivo* problems. For instance, current therapeutic process *in vivo* involves the usage of macroscopic medical devices which leads to high chances of postoperative complications, tissue trauma and patient discomfort.[36] Available micro/nanometer sized motors and the ongoing efforts to shrink the nanomotors even further provide an excellent opportunity to develop minimal invasive tools for surgery. Another nice example involves drug delivery. Due to the hydrophobic nature of cell membranes and tissue barriers,[37] it is difficult for common drug delivery vehicles such as liposomes, polymersomes, dendrimers or micelles to access and enter the targeted diseased tissue. Micro/nanomotors with efficient cargo towing and effective penetrating abilities make them excellent candidates for next generation of therapeutic carriers *in vivo*.

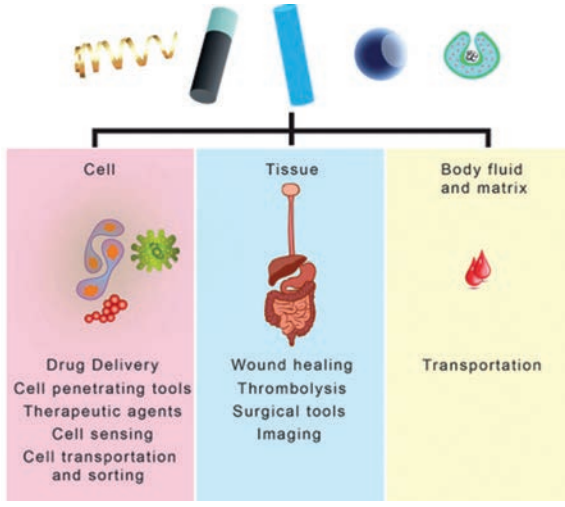

Figure 1.1. Summary of various applications for motor systems at cellular, tissue level and in body fluid/matrix.

Here we present an overview of emerging applications of motors towards *in vivo* application (at different levels including cellular level, tissue level and body fluids/matrix) (Figure 1.1) and highlight recent efforts in translating initial proof of concept into clinical practice. In the end an outlook of current challenges and future prospects is also provided.

1.2. DESIGN OF MOTORS

In this section we will provide a brief introduction of current design and fabrication methods for micro/nanomotors before we discuss their applications towards *in vivo*. For in-depth knowledge of the motor fabrication approach, other comprehensive reviews are strongly recommended. [19, 38] When functioning at a micro/nanometer regime and in a viscous biological environment, Brownian motion becomes dominant and inertia driven motion is no longer possible. Therefore careful design is important and fundamental for realization of practical applications. First of all, to achieve directed motion asymmetric geometry is crucial for asymmetric accumulation of catalytic products which form the net driving force. The experienced drag force in biological media is expected to be influenced by motor geometry/shape as well as surface chemistry. Easiness to scale-up and cost are also important factors to consider for future realistic use. Here we intend to illustrate various fabrication techniques with representative examples and discuss the respective advantages/disadvantages for different production strategies. In general synthetic motor engineering strategies can be classified as non-assembling and assembling approach. There are also ongoing efforts to develop new motor production methods by combining these two approaches.

1.2.1. NON-ASSEMBLING APPROACH

The first microsized platinum-gold catalytic motor was prepared by deposition technique.[6] This important non-assembling approach provides the possibility for fabricating structures with varied geometries,[8, 59] different materials[58] and diverse dimensions ranging from nanometer to micrometer. In general, both chemical deposition and physical deposition are used. For chemical deposition, desired materials (usually metal) are deposited onto a template via a redox reaction.[39] For preparation of rod motors, commonly used templates include cylindrical pores containing polycarbonate membranes and alumina membranes. Firstly the porous membrane template is pre-deposited with conductive metal at one side to act as working electrode. Then the template is placed in a plating chamber for deposition. The deposition process takes place inside the membrane pores (Figure 1.2I).[40]

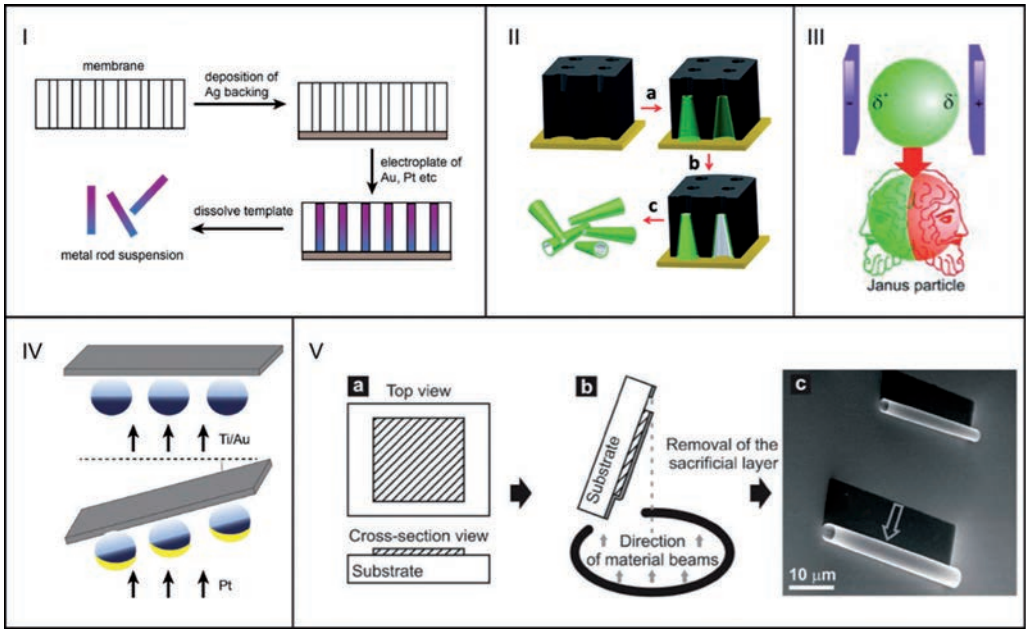

Figure 1.2. (I) Fabrication of metal wire motors through an aluminum membrane template based on chemical deposition, adapted from reference[39b]. (II) PANI/Pt tube motors prepared through a 2-step chemical deposition, electropolymerization of aniline and electro chemical reduction of platinum in a polycarbonate membrane, reproduced with permission[42], Copyright 2011, American Chemical Society. (III) Schematic diagram of the fabrication of Janus sphere motor via bipolar electrodeposition, reproduced with permission[43], Copyright 2012, American Chemical Society. (IV) Formation of Janus sphere motors by vapor deposition with vapor flux coming at a vertical/glanced angle to the substrate, adapted from reference[44]. (V) Schematic illustration of the rolled-up technology. Metal is evaporated and deposited at a tilting angle on a patterned photoresist sacrificial layer. The shadow window produces a gap for etching the sacrificial layer and guides the roll-up of the stressed membrane, reproduced with permission[45], Copyright 2008, Wiley-VCH.

Besides single metal deposition, sequential deposition of multiple metals is also possible. After dissolution of the membrane template, bi-metal or multi-stripe metal rods can be obtained. This method allows the production of rigid rod motors with good yield and high uniformity. By tuning the pore diameter and external charge, both the diameter and length of the rod can be varied. For segmented metal motors with catalytic platinum/palladium, they can propel in hydrogen peroxide mainly via self-electrophoresis mechanism.[41] For instance, in the Au-Pt biometal rod motors, hydrogen peroxide is oxidized at the Pt segment and reduced at the Au section. Due to anisotropic ion distribution throughout the rod, the self generated electricity field can propel the motor forward. Yet with increased solution conductivity (high ionic biological environments), the mobility of this type of motors will

be undermined. To explore other propulsion less affected by biological environment, such as magnetic field propulsion, researchers introduced flexibility in the segmented rod motors by selectively etching the metal section in the middle.[46] When incorporated with magnetic responsive metal like nickel, the wire motors with flexible hinges were actuated by an external rotating magnetic field. The field can induce planar bending and undulation, thus propulsion. Another possibility to power rod motors is ultrasound. Etching away the sacrificial layer in rod motors and introducing concave structure enable acoustic propulsion as the concave resulted asymmetric distribution of acoustic pressure can cause motion.[47] The moving abilities of such external field powered motors are not compromised in biological media. Besides rod like motors, tubular motors can also be fabricated with the electrodeposition approach.[42, 48] In a typical approach, a layer of polyaniline is formed in a porous membrane by electropolymerization from its monomer, followed by subsequent deposition of a metal layer as inner wall of the tube (Figure 1.2II). By catalytic decomposition (typically hydrogen peroxide) or alkali metal oxidation (in water), the propulsion of the tubular motors relies on the ejection of gas (oxygen or hydrogen) bubbles from the opening. With relatively high speed and little influence from biological medium, motors propelling by bubble recoil promise great potential in biomedical applications.[49] In addition to rod and tubular motors, Janus sphere motors can also be prepared through chemical deposition. Instead of using a static membrane as template, conductive beads when placed between two electrodes can undergo polarized electrochemical deposition at one hemisphere of the bead, giving rise to Janus particle (Figure 1.2III).[43] Metals or semiconductor materials can be deposited in this way. The Janus motors developed have been found to be driven by different mechanisms, bubble recoil, self-electrophoresis and self-diffusiophoresis.[19] Self-diffusiophoresis is a process in which a colloid can be propelled in the gradient of products from an asymmetric reaction, due to unbalanced interaction between solute and the colloid.[50] As both self-electrophoresis and self-diffusiophoresis would be influenced by the highly ionic and complicated biological media, bubble propelled Janus motors are more favourable. Besides chemical reduction, physical deposition technique is a commonly used method for motor production. The vapor deposition is a major technique for generating Janus sphere motors.[18, 44, 53] In this method metal atoms are vaporized and released into gas by bombardment of either an electron beam or ionized argon gas. Then the material in the vapor phase can condensate on the surface of target silica/polystyrene sphere and form a thin metallic film. Partial shielding of the sphere is required to ensure the asymmetry of the sphere. The resulting asymmetry of sphere motors, thus the anisotropic accumulation of products, is a key factor for directional motion. The vapor flux/substrate angle can be varied from 90 degrees to tilting angle (glancing angle).[17a, 44, 54] For the glancing angle deposition, partially sputtered sphere motors can be easily obtained due to the self-shadowing effect (Figure 1.2IV). Combining deposition at an oblique angle with substrate rotation,

the glancing angle deposition or dynamic shadow growth strategy allow the fabrication of motors more complicated in shape including V-shaped,[55] tadpole shaped[56] or helical shaped[57] with good homogeneity. The helical shaped motors with a magnetic component incorporated allow efficient propelling in biological media under rotating magnetic field. For both types of deposition approaches, the main component is a metal scaffold with limited functionalization and biodegradability possibilities. To incorporate functional units, mixing polymers during deposition may provide a solution. Yet subsequent steps are required. In addition to the deposition approach, the rolled-up technique is a versatile approach for the production of tubular motors (Figure 1.2V).[45] In this technique, multiple layers of membranes are physically deposited on a photolithography sacrificial layer. Then the sacrificial layer is etched to release the multilayer.[58] Making use of the inherent strain difference of different layers, the expansion of the bottom layer and shrinking of the top layer during the etching process generate the rolled-up architecture. The top layer which becomes the inner tube wall usually consists of catalytic metal while gold is frequently used for subsequent functionalization with biological molecules. By changing the thickness of each layer, the diameter of the opening can be well tuned in the micrometer range. Yet the complicated fabrication procedure, the ability to scale the production up and the accompanying costs are remaining challenges to be addressed.

1.2.2. ASSEMBLING APPROACH

For micro/nano architecture fabrication, the assembling approach provides an easy and effective strategy to integrate diverse miniature and multicomponent elements, ranging from lipids, polymers to catalytic entities such as enzymes and inorganic nanoparticles.[23] As the units are integrated via non-covalent interactions, the resulting responsiveness to environmental clues affords motors with multiple functionality. The morphology and size of the assembled structures can be well controlled. Another advantage of the supramolecular approach is the readily encapsulation of drug and nanoparticles, facilitating various delivery purposes. Wilson/Van Hest *et al* pioneered a fully assembling approach using the self-assembly of amphiphilic polymeric molecules poly(ethylene glycol)-*b*-polystyrene and the controlled shape transformation from sphere polymersomes to bowl-shaped stomatocytes.[21]

During the transformation process, catalytic platinum nanoparticles (PtNPs) can be efficiently entrapped into the outer cavity of the stomatocytes (Figure 1.3IV). Fuel molecules enter into the cavity through a nanometer sized opening and are decomposed, providing forward propulsion. He's group reported the fabrication of sphere/tubular vesicles based motors with a layer-by-layer technique. This technique relies on the alternating deposition of two oppositely charged materials onto a sacrificial template.[59] After removing the template, hollow sphere/tubular shaped vesicles can be obtained (Figure 1.3I, II). Then the capsules were equipped with catalytic nanoparticles or enzyme asymmetrically. In the

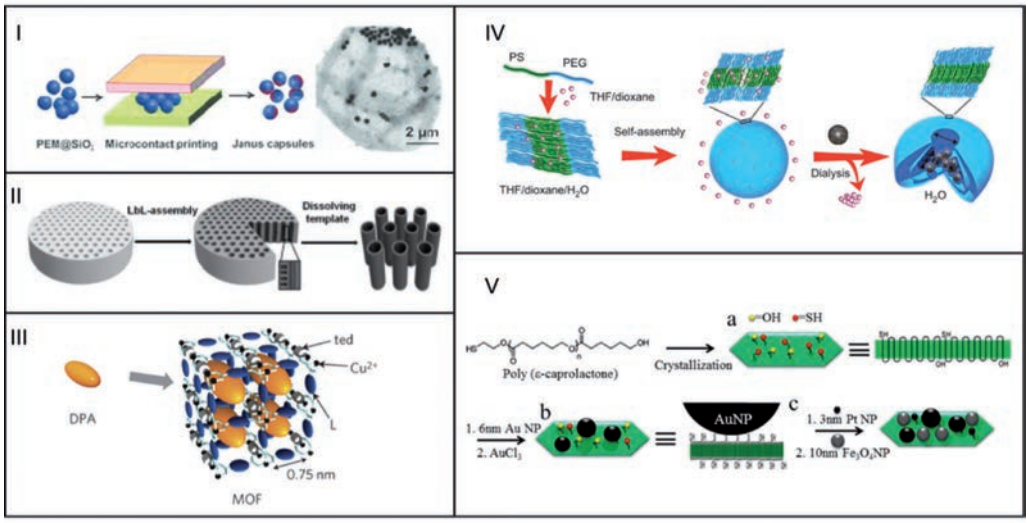

Figure 1.3. (I) Preparation of Janus sphere motors. The capsule formed from polystyrene sulfonate (PSS)/polyallylamine hydrochloride through layer-by-layer technique. Then asymmetric functionalization of catalytic dendritic platinum nanoparticles was achieved by microcontact printing, reproduced with permission[22], Copyright 2012, American Chemical Society. (II) Polycarbonate membrane assisted layer-by-layer assembly of positively charged chitosan (CHI) and negatively charged sodium alginate (ALG) based tubular motors. Platinum nanoparticles were co-mixed into the polyelectrolyte multilayers during the assembly, reproduced with permissin[51], Copyright 2013, Wiley-VCH. (III) With the assembly of copper ions and chelating ligands, a metal organic framework based motor is fabricated, reproduced with permission[52], Copyright 2012, Nature Publishing group. (IV) Formation of catalytic platinum nanoparticle loaded stomatocyte polymersome motor through the self-assembly of amphiphilic polymer poly(ethylene glycol)-*b*-polystyrene and nanoparticles, reproduced with permission[21], Copyright 2012, Nature publishing group. (V) Schematic illustration of the formation of polycaprolactone based polymer single crystal and the functionalization with catalytic platinum particles, reproduced with permission[10b], Copyright 2013, American Chemical Society.

presence of fuel, the catalytic particles/enzymes generate thrust, achieving autonomous motion.[22] Using silica precursor and surfactants via a "sol-gel" process, Sanchez's group successfully prepared mesoporous silica nanoparticles of difference sizes.[24] With electron beam evaporation technique and platinum deposition at one side, silica nanoparticles could be turned into platinum half coated motors. The mesopores were used for cargo loading. Besides solid silica nanoparticles, they also made use of hollow mesoporous silica nanoparticles (HMSNP).[16a, 25] The hollow structures promise high cargo loading capacity. After shielding one side with silicon dioxide, amine functionalized HMSNP could be readily modified with different enzymes (catalase, urease, glucose oxidase). The enzyme motors were powered by biocompatible fuel including glucose and urea. In addition to the silica sphere motors, the same group also devised other shape motors including hollow reverse Janus and tube motors via "sol-gel" chemistry on silver nanowire template.[60] Different

from previous tube motors powered by bubble recoil, the biocatalytic reaction triggered by urease on the internal/external surface of the tube propelled the nanotube motors via a jet of liquid. With this mechanism, accumulation of bubbles in the environment is avoided, making it advantageous for practical applications in biological environments. Another assembling approach for motor fabrication involves the self-assembly of inorganic nanoparticles (including catalytic PtNPs) on polymer single crystals (Figure 1.3V). The polymer single crystal was fabricated through crystallization of polycaprolactone.[10b, 61] Alternative building blocks for self-assembled motors include metal–organic framework (MOF) (Figure 1.3III). Matsui's team reported the fabrication of a $[Cu_2L_2ted]_n$ based MOF motor (Cu is copper, L is 1,4-benzenedicarboxylate, ted is triethylenediamine). It was found the hydrophobic diphenylalanine (DPA) peptide could assemble into the nanometer sized pore of the coordination framework at the water/MOF interface. By means of the Marangoni effect, the caused surface tension difference drives the MOF motor forward.[52] Recently there has also been increasing efforts to integrate the synthetic motors with natural motile units. Wang's team explored to integrate magnetic nanoparticles into red blood cells.[62] The asymmetric distribution of nanoparticles inside the cells enables ultrasound propulsion. Another interesting example is flexible synthetic flagella or a chain of magnetic iron oxide particles linked by double stranded DNA.[63] The artificial flagella can propel forward under a rotating magnetic field.

1.3. MICRO/NANOMOTORS TOWARDS IN VIVO APPLICATION: CELL, TISSUE AND BIOFLUID

Over the last decade, various micro and nanomotors have been fabricated and tested in various environments including sea water or organic solvent.[33b] Yet there is relatively little knowledge about the performance and behaviour of motor systems in a biological cell culture, tissue and biofluid. More work in this field is now being carried out in order to bridge the micro- and nanomotors with clinical practice.

1.3.1. APPLICATIONS AT CELLULAR LEVEL

1.3.1.1. Drug delivery

Catalytic motors for drug delivery

One of the main challenges of nanomedicine is to overcome the limited efficiency of delivering therapeutic agents to cell,[64] in particular in areas related to the treatment of cancer, heart and vasculature diseases.[65] To address the issue, micro/nanomotors with efficient cargo towing and transporting abilities have been given growing attention.

He's group proposed the first example of tubular polyelectrolyte based motor created with the lay-by-layer technique and used it as a drug delivery carrier to cells (Figure 1.4I). The fabricated multilayered nanotube motors were porous and allowed easy incorporation of catalytic platinum nanoparticles, magnetic iron oxide particles and antitumor model drug doxorubicin into the inner layer of tubular motors. The loading of iron oxide particles facilitated directional control of the motor with an external magnetic field. In a human cervical cancer (Hela) cell culture (the medium was supplemented with 3% hydrogen peroxide), the nanorocket displayed bubble recoiled propulsion. Under magnetic navigation, the tubular motor moved towards the cell and attached to it. It was shown by SEM that the polyelectrolyte nanorocket was bound to the outer surface of the cell membrane. Upon sonication, the intactness of polyelectrolyte nanorockets was lost, resulting in fast release of the doxorubicin from the outer layer of the nanotube motors.[51]

The same group later compared the efficacy of using active motors or passive carriers for drug delivery. They made use of platinum sputtered mesoporous silica nanoparticles as Janus nanomotors while unsputtered particles were used as passive control (Figure 1.4II). Doxorubicin could be loaded by physical absorption into the porous channels of silica particles. In the presence of 0.2% hydrogen peroxide containing Hela cell culture, more uptake was observed for platinum capped mesoporous silica nanoparticles than unsputtered mesoporous silica nanoparticles. It exhibited the advantage of active drug delivering method. Upon entering into Hela cells, egg phosphatidylcholine bilayer covered on the surface of silica nanoparticles was slowly degraded to release the doxorubicin.[66]

Sanchez's team reported the platinum sputtered mesoporous silica nanomotors of different sizes (40 nm, 65 nm and 90 nm).[24] Model cargo FITC, Rhodamine B and methylene blue were loaded to the nanomotor by covalent linking or incorporation into mesopores. For Rhodamine B and methylene blue loaded into mesopores, sustained release was observed in the presence/absence of hydrogen peroxide. With a ratchet shaped microchip, the nanomotors can be actively guided to a target chamber. Compared to passive mesoporous silica nanoparticles, the active nanomotors showed enhanced accumulation at the target chamber.

For realistic applications *in vivo*, biocompatibility is however an important issue to consider. To increase the biocompatibility of the motors, He's group utilized a biodegradable micromotor for drug delivery. A bovine serum albumin/poly-L-lysine (BSA/PLL) based multilayer tube motor was fabricated and loaded with gelatin, gold nanoparticles (near infrared agent), magnetic particles (for external steering), doxorubicin (antitumor drug) and catalase (motor). The main body of the protein based micro-rocket was degradable in presence of α-chymotrypsin. With the hydrogen peroxide decomposing abilities of catalase, the tubular motors were propelled forward. When precisely guided with an external magnetic field to the vicinity of Hela cells, doxorubicin was released under near infra-red trigger (Figure 1.4III). This is because gold nanoparticles generate heat locally with

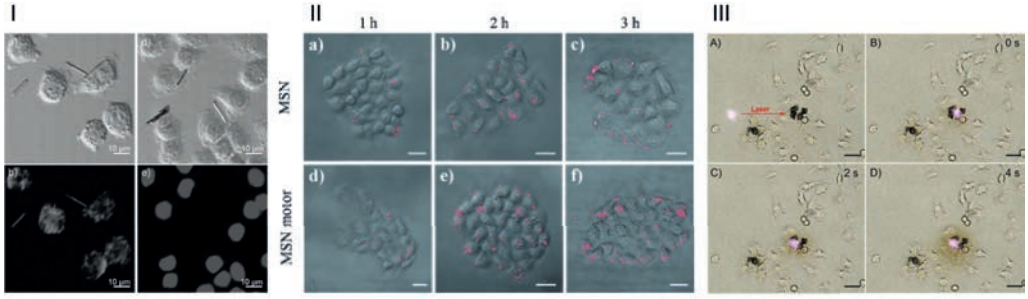

Figure 1.4. (I) Fabrication of $(ALG/CHI)_2$-Fe_3O_4-$(CHI/ALG)_{14}$-Pt NP tubular motors with layer-by-layer technique; the tubular motors penetrated into Hela cells and the doxorubicin incorporated in the tube wall was released upon ultrasound treatment, reproduced from reference[51], Copyright 2013, Wiley-VCH. (II) Preparation of Janus mesoporous silica nanomotors by platinum sputtering onto single layer of mesoporous silica spheres (MSN); doxorubicin was released once the egg PC bilayers on surface of uptaken nanomotors degraded in Hela cells. Active MSN motors exhibit more cell entry than the passive MSN particles, reproduced with permission[66], Copyright 2014, Wiley-VCH. (III) Near infrared irradiation triggered release of doxorubicin from $(PLL/BSA)_{10}$-DOX-CAT-AuNPs-gelatin motors to cells. The diffusing out red doxorubicin can be clearly seen, reproduced with permission[67], Copyright 2015, American Chemical Society.

near infrared irradiation, facilitating the sol-gel transition of gelatin and thus release of doxorubicin.[67]

Despite the fact that some of the present motor systems are considered safe towards cells,[68] the toxicity of the fuel itself hydrogen peroxide (the most commonly used fuel for propulsion) and other chemical fuels has been under much debate.[69] As hydrogen peroxide is considered to induce oxidative stress to cells and causes protein denaturation, it is considered to limit the long-term application towards cells and *in vivo*. For successful *in vivo* application, the fuel source of motors needs to be extended towards more biofriendly molecules at biologically relevant concentrations.

The use of locally available chemicals or bio-relevant molecules as fuel source for micro- and nanomotors provides an excellent solution to the biocompatibility problem. Attempts involved the use of glucose and urea as fuel source.[16a, 25, 60a, 70] Sanchez's team introduced a catalytic enzyme (glucose oxidase and urease) functionlized Janus hollow mesoporous silica nanomotor.[25] The biocatalytic reaction with biocompatible and nontoxic substrate (glucose and urea) was used to power the motor. This possibility shed new lights to the development of motors in the biomedical context. Städler *et al.* reported a poly(dopamine) (PDA) coated silica based motor.[70] Via a wax-in-water Pickering emulsion technique, one hemisphere of PDA silica nanoparticle was PEGylated while the other half was used for catalase and glucose oxidase modification. With the cascade reaction of enzymes, glucose can be used to propel the silica motor. In tumour tissues anaerobic glucose metabolism produces lactic acid as byproduct, leading to an acidic tumor microenvironment.[71] Guix

and Schmidt *et al.* created a calcium carbonate microparticle with cobalt partially deposited on the surface, generating a Janus micromotor. In the acidic environment produced by Hela cells, the Janus micromotor demonstrated a continuously directed motion with a speed of 0.544 μm/s. The motion was attributed to the gradual dissolution of calcium carbonate microparticles in acid.[72] Molecules such as glucose, urea, lactate can be found in cell microenvironment and do not present toxicity to the cell. However either the concentration required for propulsion is usually higher than the level available *in vivo* making the motors propel at a relatively slow speed. Motors with higher conversion efficiency are required for practical purposes.

Another important factor to consider for propulsion of catalytic motors[73] in a cell medium is the propulsion mechanism. It is generally accepted that motors can be propelled via four mechanisms: generated bubble thrust (bubble propulsion), inhomogeneous distribution of reaction products (diffusiophoresis)/surface tension around motors or electric gradients (electrophoresis) inside the metal motors.[20] As motors based on electrophoresis and diffusiophoresis would be influenced and even paralyzed in high ionic strength medium (such as cell culture medium which is complex in its composition), motors propelled by bubble propulsion are functional for realistic applications in/towards cells.

Fuel free motors for drug delivery

Motors propelled by external field (ultrasound field, magnetic field, optical field and electric field etc) have received increasing attention.[74] When eliminating the use of chemical fuel source, the application of motors is not restricted by the adverse influence of fuel or lack of local fuel supply.

Using electrophoretic and dielectrophoretic forces, Levchenko and coworkers manipulated a gold nanowire and precisely transported it into a target Hela cell. After coating the gold nanowire with cytokine tumor necrosis factor alpha (TNFα), the team successfully stimulated canonical nuclear factor-kappaB signaling in a single cell (Figure 1.5I).[75]

Among the external fields, magnetic field is the most attractive concerning its flexibility, tunable force and minimal invasiveness to cells. Nelson reported a helical microswimmer resembling bacterial flagella. Under the control of three orthogonal electromagnetic coil pairs, the microswimmer can be manipulated to push a polystyrene microsphere.[76] Fischer's group devised helical nanoswimmers with shadow growth technique and the swimmers show great potential in cargo delivery.[57] Wang and co-workers used external magnetic field to manipulate motor for drug delivery. Magnetic nickel containing alloy nanorods were able to pick up magnetic payloads of different sizes (100 nm–3.0 μm) through magnetic attraction. The cargos could be transported and delivered along a determined route.[77]

By incorporating a nickel segment into a Ru-Au nanorod, Mallouk *et al.* gained directional control over the acoustically powered rod motors with an external magnetic field. With

the steering of magnetic field, Ru-Ni-Au nanorod motors can target to Hela cells with micrometer precision.[78]

Another interesting example was proposed by Liu and coworkers. They fabricated a wormlike mesoporous silica nanotube. By depositing magnetic $CoFe_2O_4$ nanoparticles onto the tube surface, the nanotubes were imparted with magnetic properties. Via free diffusion, the dye carboxyfluorescein was loaded into the nanopores of silica nanotubes. Then the nanotube surface was covered with a layer of DNA G-quadruplexes, which can fold into G-quartets structures to prevent the leakage of carboxyfluorescein. With an alternating magnetic field to heat up $CoFe_2O_4$ locally, the G-quadruplex structure underwent a conformational change to random single strand structure leading to release of carboxyfluorescein from nanopores of silica nanotubes into Hela cells within 1 hr (Figure 1.5II).[79]

Alternatively, ultrasound field has also been considered safe and used extensively in the biomedical field such as cross section imaging *in vivo*.[80] Wang's group devised a porous gold nanowire based motors by etching away the silver component from the silver-gold nanowires. Under ultrasonication, the local pressure gradient resulted from concave geometry at one end of the wire propelled the nanostructure forward (Figure 1.5III). The porous structure as well as anionic polymer poly(acrylic) acid (PAA) coating on the nanowire surface ensured an efficient loading of cationic model drug doxorubicin. After approaching the Hela cells, controlled release of doxorubicin was triggered with a sudden increase in temperature from 20°C to 40°C by near infrared irradiation.[81] Besides chemical drugs, the nanomotors can also be used for delivering bioactive genes and cytokines to cells. Wang's group and Chen *et al.* modified gold nanowire with small interfering RNA (siRNA). The siRNA, an important tool for gene therapy, is used for formation of RNA-induced silencing complex in cells to avoid the expression of undesirable proteins. Gene modified MCF-7 cells expressing green fluorescent protein (GFP) were used as model cells. With ultrasound propulsion, the siRNA modified nanowires were rapidly delivered into a model MCF-7 cells (Figure 1.5IV). The siRNA was engineered to target for GFP expression. A 13 fold improvement of gene silencing was observed compared to static nanowires.[82]

The external fields could provide not only propulsion but also offer further directional control of the movement. At the micro/nanometer regime, the Brownian randomization significantly interferes with the moving direction of motors and undermines their potential for practical uses. Therefore directional control is necessary. The external fields such as electrical field, magnetic field and optical field can provide possibilities for such directional control. Other steering approaches besides external fields have also been explored and to be mentioned in the next section.

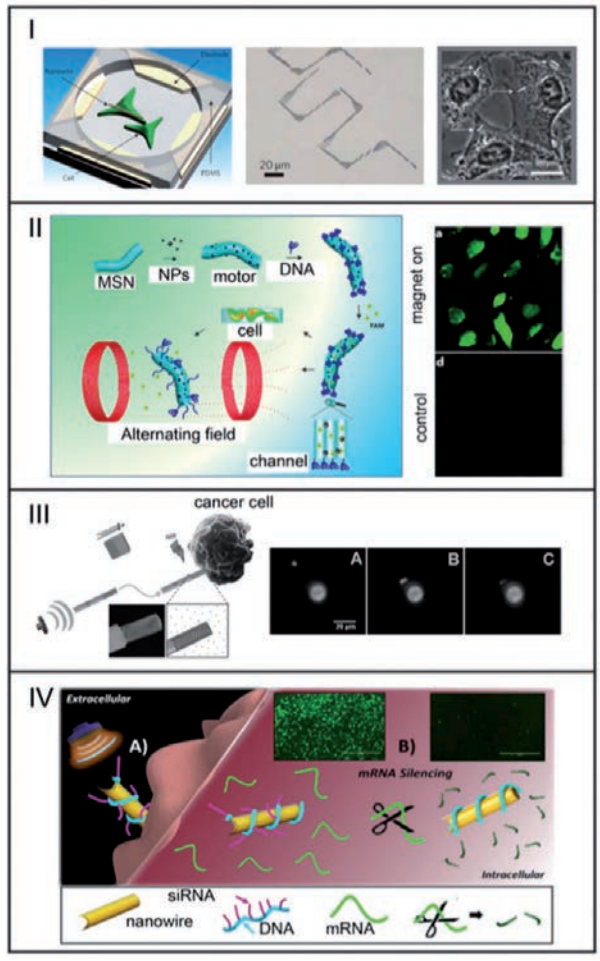

Figure 1.5. (I) With an electric field, gold nanowire was precisely manipulated and cytokine tumor necrosis factor alpha was delivered into cells, reproduced with permission[75], Copyright 2010, Nature Publishing Group. (II) Preparation of $CoFe_2O_4$ nanoparticles loaded wormlike silica nanotubes; alternating magnetic field triggered release of carboxyfluorescein into cells, reproduced with permission[79], Copyright 2015, American Chemical Society. (III) Fabrication of porous gold nanowire motor and its propulsion under ultrasound exposure. Upon near infra-red irradiation the locally increased temperature led to release of doxorubicin from the motor surface, reproduced with permission[81], Copyright 2014, Wiley-VCH. (IV) Rapid delivery of small interfering RNA into cells via ultrasound propelled gold nanowires and subsequent silencing of GFP expression, reproduced with permission[82], Copyright 2016, American Chemical Society.

Targeted drug delivery

For nanoparticle mediated drug delivery, precise and targeted delivery of therapeutic cargo to diseased cells remains a hurdle and a bottleneck.[83] Current targeting delivery strategies rely on passive deposition of therapeutic nanoparticles in the vicinity of diseased tissues. For instance, tumor targeting therapy uses the enhanced permeation and retention effect. That is, in the fast growing tumor area (especially in an experimental model of tumor bearing immune defect mice, tumor usually develops in a very rapid manner), the tumor vasculature is leaky and therapeutic particles get retained there. Yet such targeting therapy achieved limited clinical success due to the much less leaky vasculature system in general patients that develop tumors over a prolonged period of time. The systematic toxicity caused by drugs failing to reach the target tissues is high. By combining self-powered motor systems with external fields or stimuli gradients, precisely navigated motors promise to be efficient delivery vehicles capable of reaching the exact diseased cells, thus reducing side effects caused by off target drugs.

External fields can not only provide the propulsion source but also offer the opportunity of guiding the motors and achieving noncontact manipulation. Wang and coworkers developed a flexible nickel-silver nanoswimmer. Under a weak external rotating magnetic field, the nanoswimmers could be propelled forward at a relatively high speed (more than 10 $\mu m\ s^{-1}$). The nickel segment permitted the pick-up of drug loaded magnetic pol(D,L-lactic-co–glycolic acid) (PLGA) microparticles through magnetic interaction (Figure 1.6I). With this it was demonstrated that motors could generate high enough force to load even heavy particle cargoes. Via precise magnetic guidance, PLGA loaded nanoswimmers were able to transport from the loading reservoir through a channel to the predetermined chamber where Hela cells were seeded.[84] In this case, the use of chemical fuel was circumvented and the presence of magnetic field facilitated directed delivery.

Mhanna and Nelson *et al.* at ETH exploited artificial bacteria flagella (ABF) for precise drug delivery. With rotating magnetic field, the magnetic actuated helical microdevices could be propelled forward (Figure 1.6II). Through physical absorption to the surface of ABF, model drug calcein incorporated into liposomes were loaded to the microswimmer. After reaching the target C2C12 mouse myoblasts cells under magnetic guidance, the model drug calcein could be released precisely into the target single cell by fusion with the cell membrane or uptake via endocytosis.[85] By using temperature-sensitive dipalmitoylphosphatidylcholine (DPPC)-based liposomes, the same group showed efficient controlled release of calcein after elevating the temperature from 37°C to 41°C.[86]

Taking advantage of the local chemical stimuli gradient has proven to be an alternative approach for steering motors towards cells. Wilson's group demonstrated that stomatocyte nanomotors could move and be guided by a gradient of hydrogen peroxide. This will be described in detail in Chapter 2. Interesting future direction would involve the usage of other disease signal chemical gradients. Combining multiple targeting strategies would also be beneficial for improving the targeting efficiency.

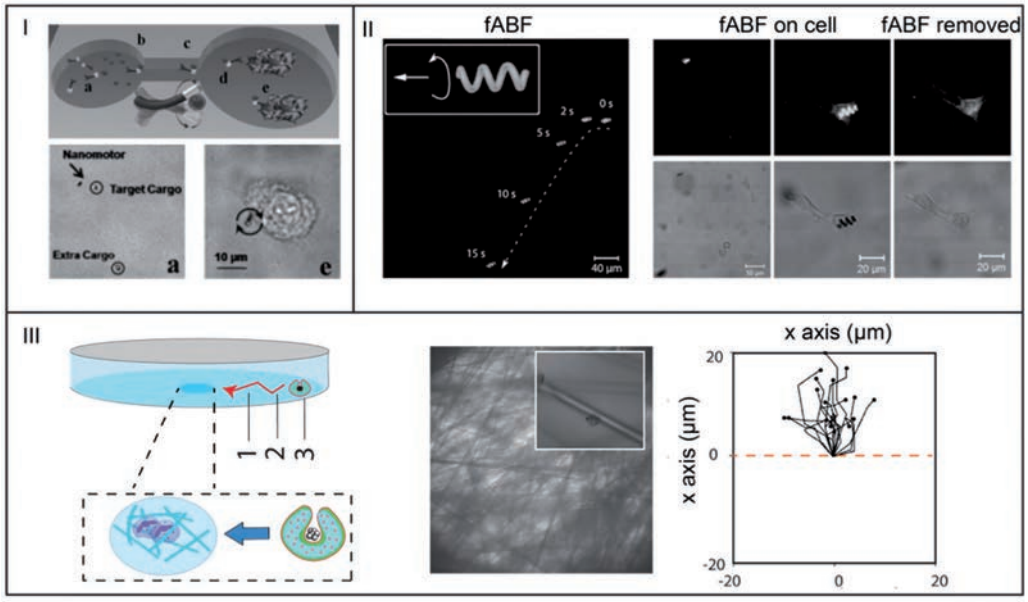

Figure 1.6. (I) Flexible magnetic nickel-silver nanoswimmers approached, picked up and transported drug loaded magnetic pol(D,L-lactic-co–glycolic acid) (PLGA) particles from the left reservoir to the right chamber. The particle cargo was then delivered to the vicinity of a target cell, with the steering of an external magnetic field, reproduced with permission[84], Copyright 2011, Wiley-VCH. (II) Under a rotating magnetic field, helical microdevices transported calcein loaded liposomes precisely to target cell. Through fusion with the cell membrane or endocytosis, calcein can be delivered into the cell. Even after the removal of liposome functionalized artificial bacteria flagella (fABF), the fluorescence inside the cell was still visible, reproduced with permission[85], Copyright 2014, Wiley-VCH. (III) Doxorubicin loaded stomatocytes nanomotors moved along the hydrogen peroxide gradient towards neutrophils cells. The neutrophils were seeded on a substrate network, reproduced with permission[87], Copyright 2015, Wiley-VCH.

These micro/nanoshuttles transporting therapeutic payloads to predetermined areas following remote guidance or locally environmental stimuli show great potential in selective and precise delivery. To further increase the efficacy, functionalization of motors with targeting ligands or moieties will be beneficial.[88] Stimuli sensitive linkers besides physical adsorption between cargoes and motor systems are to be introduced to avoid unwanted release of carried cargoes during transportation. It is also necessary to improve the drug loading efficiencies (especially for metal rod based motors). With micro/nanomotors carrying multiple therapeutic/imaging agents, synergistic therapeutic efficiencies are to be tested.

1.3.1.2. Cell penetrating tools

Micro- and nanomotors can accomplish propulsion inside and towards cells. With the great thrust generated, the motors penetrate, cleave and stab into cells as a cell penetration

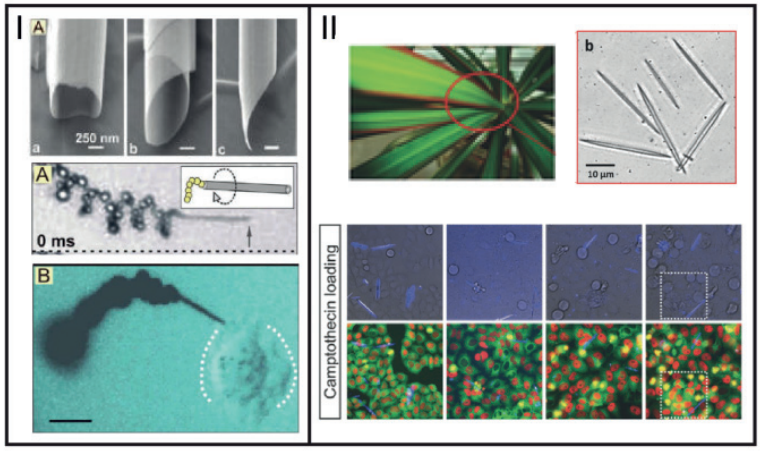

Figure 1.7. (I) Fabrication of InGaAs/GaAs/Cr/Pt tubular motors with sharp tips. By roll-up at an angle, tube motors with a sharp tip can be obtained. In the presence of hydrogen peroxide fuel, the motors can penetrate into a fixed Hela cell, reproduced with permission[90], Copyright 2012, American Chemical Society. (II) Iron and titanium coated microneedles (derived from plant Dracaena sp.) drilled into Hela cells with a rotating magnetic field, reproduced with permission[92], Copyright 2015, Wiley-VCH.

tool. The micro/nano motors are extremely promising to overcome cell barrier and directly deliver drug payloads to target cells. Compared to passive drug loaded nanoparticles, micro/nanomotors may be superior in accessing for instance solid tumor tissue cells where the high pressure built-up basically blocks the entry of external molecules.

Cai *et al.* reported the fabrication of carbon nanotube with a nickel tip via plasma enhanced chemical vapour deposition.[89] Responsive to a rotating magnetic field, the nanotubes could spear into cells on a substrate. Then with a static gradient field, the nanotubes could further penetrate deeper into the cells. By attaching plasmid DNA containing enhanced green fluorescence protein (EGFP) sequence to the nanotube, the penetration of nanotubes into cells led to high transduction efficiency for different cell lines including Bal17 B lymphoma, primary B cells and primary neurons.

With a rolled-up technology, Sanchez' group prepared InGaAs/GaAs/Cr/Pt based tubular motors. The catalytic tubular motors demonstrated propulsive motion when immersed in the hydrogen peroxide solution (20% v/v). With a thin layer of iron, the motion could be controlled with an external magnetic field. By exploiting the corkscrew motion pattern, the tubular motors with a sharp tip could penetrate a fixed Hela cell (Figure 1.7I).[90] This is a nice example of tubular motors as cell-penetrating tool however the hydrogen peroxide level used in the experiment is too high for realistic cellular delivery.

Due to the asymmetric scattering of sound waves at the convex end of gold nanorods, the nanorod motors prepared by Mallouk's group showed fast axial propulsion in cells. After

24 hours of incubation with Hela cells, the nanorods could enter into the cells and remain ultrasound responsive after their uptake. Without additional chemical fuel, propulsion inside the cells was observed.[91]

Developing motor systems based on the natural occurring micro/nano structures has become a new approach for motor fabrication. Srivastava and Schmidt *et al.* derived calcified porous microneedles (40–60 µm in length) from *Dracaena* sp. (a type of plant). With electron beam deposition method, the microneedles were coated with a layer of iron and titanium. By incubating with camptothecin (antitumor drug) for 3 days, the drug was loaded into the porous microneedles. Under a rotating magnetic field, the Fe-Ti coated microtubes drilled into the Hela cells (Figure 1.7II). The penetration of microneedles into the cell membrane resulted in cell death as confirmed with cell viability assay. Without external magnetic field, the drug-loaded microneedles could inhibit Hela cell growth and lead to aberrant cell divisions. By combining the cell penetrating abilities and drug transporting properties, the microneedle motors demonstrated potentials as new drug delivery vehicles.[92]

For cell penetration micro/nanomotors manipulated or actuated with a rotating magnetic field, the moving direction could be precisely controlled with the rotation field. In this way it was possible to precisely locate target areas and perform surgery tasks. For other type of surgery tools (powered for instance by ultrasound), precise directional/temporal control and targeting to surgery cells remain questions to be answered.

Wilson's group reported the conjugation of natural cell penetrating peptides (tat) to the surface of stomatocytes polymersomes motors. It was found the peptide modified stomatocytes motors enhanced the penetrating efficiency of the delivery agents into intact Hela cells.[93] This part will be described later in Chapter 3.

1.3.1.3. Therapeutic agents

Besides acting as delivery agents for therapeutic molecules, the motors themselves can perform as therapeutic agents.

He and coworkers described an approach to produce platinum nanoparticles loaded polyelectrolyte microtube motors with gold nanoshells and a tumor targeting peptide T7 (containing the HAIYPRH sequence) coated on the surface. After localizing to the vicinity of tumor cells, micromotors recognized and targeted selectively the HeLa cells. When mixing red blood cells (as control cells) with the tumor cells, no binding to the red blood cells was observed. The dissipated heat resulted from the gold plasmon resonance upon using near infra-red led to a temperature increase of approximately 10 °C in a 70 µm range around the micromotors. A subsequent apoptosis of the targeted cells was observed. In this case, the micromotors demonstrated their application as a photothermal agent for selective eradication of cancer cells.[94]

1.3.1.4. Cell sensing

Current sensing techniques involve time consuming sample preparation. Fast/selective targeting and sensing in unprocessed biological samples are particularly interesting. Utilizing autonomously moving motors functionalized with bioreceptors was demonstrated to be a promising approach.

Wang's team described a method using motors for detecting rRNA released from *E. coli 16S* bacteria. A nucleic acid containing sample was firstly incubated with a surface bound oligonucleotide followed by addition of a silver nanoparticle-tagged detector probe. At higher target nucleic acid concentration, more silver nanoparticles were captured. With addition of hydrogen peroxide and Au-Ni-Au–Pt nanomotors, the silver particle quickly dissolved into silver ion and accelerated the motion of the nanomotors. As the moving speed of nanomotors correlates with the level of rRNA and corresponding bacteria concentration, the motion readout provides a new approach for detection of rRNA or other biomolecules.[95]

Besides detecting RNA secreted by cells, motor system has proven capable of detecting RNA in a cell. The same team described a single step method for rapid detection of target miRNA inside cells with ultrasound powered nanomotors. With EDC-NHS conjugation, a graphene-oxide sheet was introduced to a cysteamine functionalized gold nanowire. Single strand DNA-fluorescein amidine (fluorescent dye, FAM) was absorbed onto the graphene-oxide surface through π-π stacking interactions between the nucleotide bases ring (in the single strand DNA) and the graphene-oxide sheet. Due to this close distance between fluorescein amidine and grapheme oxide, the fluorescence of fluorescein amidine was rapidly quenched via fluorescence resonance energy transfer. Driven by ultrasound propulsion, the DNA-FAM functionalized grapheme oxide/gold nanowires were delivered to intact cells within a few seconds. As single stranded DNA has a higher affinity for miRNA in cells, the DNA-FAM was displaced from the surface of graphene-oxide and bound to target miRNA, leading to fluorescence recovery. As the fluorescence signal was correlated with the amount of target miRNA-21 which was overproduced in metastatic breast cells, the proof of concept experiments demonstrated a fast and precise cancer screening with MCF-7 cells.[96]

Fan's team employed a one dimensional (1D) plasmonic-magnetic (PM) nanotube for in situ cell membrane composition sensing.[97] The nanotube was incorporated with nickel nanomagnets and dual-surface-coated plasmonic silver nanoparticles. The embedded nanomagnets and silver nanoparticles facilitated magnetic maneuvering and surface-enhanced Raman scattering (SERS) detection, respectively. With external magnetic field, the PM nanotube transported to the target single CHO cell and came into contact with the cell membrane. The resulted SERS spectra showed characteristic peaks of lipid and protein. This precise and sensitive method is also expected to be applicable to other adherent animal/human cells.

In general, the addition of external chemical fuel may interfere with the detection results.

Therefore motor systems that can make use of sample media or components are highly desirable. However the possible impact of motor reaction products or resulting pH changes on the sensing results shall be taken into future consideration.

1.3.1.5. Cell transportation and sorting

With the cargo towing abilities, the motors not only transport small molecule drugs, genes, cytokines but also demonstrate capabilities to pickup and transport cells in a biological environment. With complicated biological samples, motors with built-in recognition moieties or external control demonstrate a possibility for fast transportation and selective isolation of target cell cargoes.

Sanchez *et al.* proposed the idea of using micromotors for loading, transporting and delivering cells.[98] They fabricated microtube motors with rolled-up technology. The diameter of the tubular motors was optimized to accommodate the model murine CAD cell. As the bubble generation and migration inside the tubular motors would induce fluid pumping, it was expected the cell would be sucked and picked up. With the alignment of an external magnetic field, the cell loaded microtube motors transported the cell under guidance. By abruptly changing field direction, the cell could be released and delivered.

The team later also used rolled-up nanotubes for transporting of yeast cells.[90] It was expected that the yeast cell attached to the outer surface of the nanotubes through van der Waals interaction. After loading three yeast cells, the tubular motor experienced a speed decrease. As the drag force during motion weakened the interaction, the cells eventually got released.

Zhang and Nelson *et al.* reported a nickel nanowire demonstrating a tumbling motion with a rotating magnetic field. For cell manipulation, flagellated microorganisms or red blood cells were loaded to the nickel based nanowires through entanglement and attachment. The blood cell was transported and positioned on the top of an epidermal cell.[99] This provides a new strategy for precise cell transportation and manipulation.

Schmidt and Sanchez *et al.* successfully trapped bull sperm cell inside a conically shaped magnetic Ti/Fe microtube. While the sperm cell provides the propulsion, the magnetic microtube allows remote magnetic control (Figure 1.8I). With an external magnetic field, the cell loaded microtube could be oriented and was able to move from a reservoir chamber to a collecting chamber.[100]

Later the same group fabricated a polymer micro-helix with a NiTi bilayer coating. Sperm cell could be captured by the synthetic helical micromotor with its tail confined inside the inner part of the micro-helix and its head sticking out at the front end of the helix. By a rotating magnetic field, the helix-sperm hybrid motors became actuated (Figure 1.8II). By transporting an immotile sperm cell to the oocyte cell and releasing the sperm cell, the motor system showed great potential in treating infertility.[101] Additional systematic screening and selecting of the sperm cells may be needed.

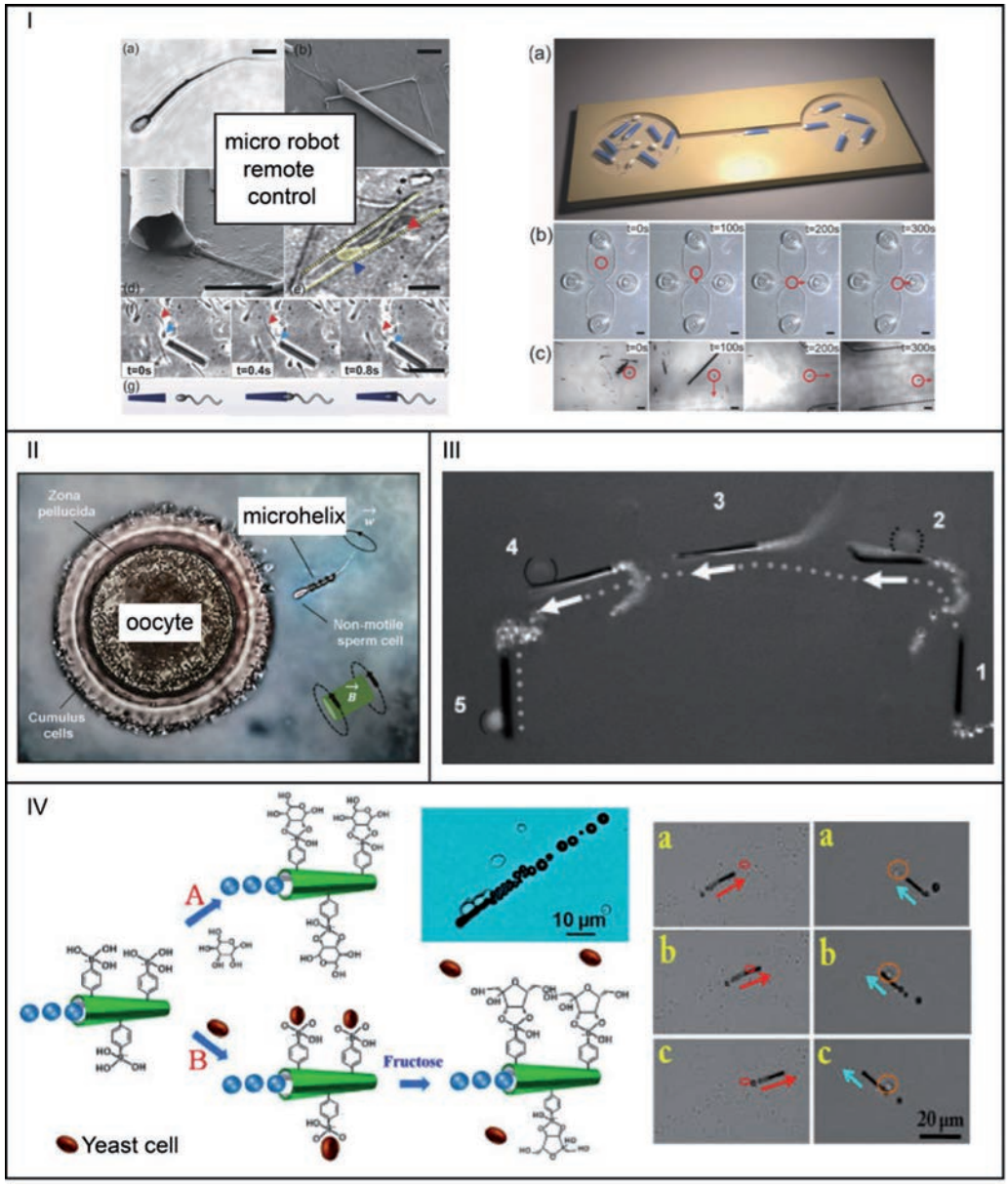

Figure 1.8. (I) Sperm cells trapped inside a conically shaped Ti/Fe microtube were transported and isolated, reproduced with permission[100], Copyright 2013, Wiley-VCH. (II) Immotile sperm cell captured by microhelices was delivered to an oocyte cell, reproduced with permission[101], Copyright 2016, American Chemical Society. (III) An anti-carcinoembryonic antigen (anti-CEA) monoclonal antibody tubular motor specifically picked up a CEA+ pancreatic cancer cell, reproduced with permission[104], Copyright 2011, Wiley-VCH. (IV) Poly(3-aminophenylboronic acid) (PAPBA)/Ni/Pt microtubular motor selectively sorted yeast cell out, reproduced with permission[105], Copyright 2012, American Chemical Society.

The selective interaction between metal and bacteria cell can be used to form the cell-motor hybrid. Sanchez's team reported *Escherichia coli* (*E. coli*) preferentially adhered to Pt cap of Janus particles over Fe, Ti or Au.[102]

Suzuki *et al.* fabricated a polystyrene based micromotor with platinum and zinc hemispheres formed. Autonomous movement of the microparticle was powered by reaction of zinc and water on the particle surface. Hydrophobic interactions were used to capture *Escherichia coli* (*E. coli*) cell which adhered to a self-assembled monolayer of alkanethiolates on the platinum part of the micromotor. By adjusting the free zinc ion in solution and controlling the dissolution of zinc from the micro motor, *E. coli* cells were shown to be released in a controlled manner.[103]

Besides using physical interaction between motors and cells, functionalization of motors with specific groups facilitates selective binding of motors to cells and subsequent sorting.

Circulating tumor cells are primarily responsible for tumor metastasis. Wang's team successfully functionalized tubular microswimmers with an anti-carcinoembryonic antigen (anti-CEA) monoclonal antibody specifically for a surface antigen over-expressed in approximately 95% of colorectal, gastric and pancreatic cancer cells. The inner platinum layer of the micromotor was responsible for propulsion in hydrogen peroxide containing medium (including dilute serum). After capturing CEA+ pancreatic cancer cell in diluted human serum, the high speed of micromotors was only slightly decreased from 85 μm s^{-1} to 80 μm s^{-1} and the trajectory was not compromised. Additionally, in a mixture of cell suspensions, anti-CEA functionalized micromotors could selectively bind and pickup target cells (Figure 1.8III).[104]

The same group reported the preparation of a poly(3-aminophenylboronic acid) (PAPBA)/Ni/Pt microtubular motor. The boric acid in the motor could be used for recognition and interaction with monosaccharide moieties. Yeast cells with glucose residues on the cell walls were selectively recognized and picked up by the (PAPBA)/Ni/Pt microtube (Figure 1.8IV). In the presence of 3% hydrogen peroxide, the microtube was able to transport yeast cells with speed of 20 μm s^{-1}. After addition of fructose (with higher affinity for boronic acid), the yeast cells detached due to the competitive binding of fructose.[105]

With the new capabilities of motors discussed above, it would be interesting to transport not only circulating cells in suspension but also move and manipulate cells that are adherent to surfaces. It would also be exciting to integrate these cell sensing and sorting functions into a micro/nanochip or electronic device which might represent a significant step towards biologically integrative systems combining functions from diagnostic to post-therapy evaluation.

1.3.2. APPLICATIONS AT TISSUE LEVEL

1.3.2.1. Wound healing

During a natural injury or surgery process, wounds are introduced into the human or animal body. The open tissues highly increase the chances of bacterial infection and implicated syndromes. To heal the wound, a complicated process is involved with several stages including clotting, wound contraction, tissue formation etc.[109] Recent exploration of wound healing with motors presents excellent examples of healing assistance in different stages.

The early stage of wound healing involves blood clotting. Kastrup's group developed a porous calcium carbonate microparticle based motor system to assist this process. The microparticles developed were mixed with protonated tranexamic acid, the fuel. By reacting with the acid and releasing CO_2, the motor could propel laterally while rising buoyantly (Figure 1.9I). At a relatively high speed at maximum 5.9 mm/s, the motor system was capable of transporting against blood flow. When loading the porous calcium carbonate based micromotor with thrombin (a serine protease that activates the coagulation system *in vivo*), the motors were found penetrating deep into the wound (amputated mouse tail) and shortened the bleeding time significantly from 14 min (for non propelled thrombin) to 4 min.[110]

Next stage of wound healing associates wound closure. To assist this process, He's group fabricated a silica nanoparticle based Janus motor through layer by layer self-assembly (Figure 1.9II).

A layer of gold was sputtered onto the silica surface. When administered to the wounded tissue area, the particles and particle agglomeration would generate local heating under NIR laser irradiation. The heat leads to melting of blood cells and formation of a film. Additionally, at this elevated temperature, collagen in local tissue was denatured, leading to tissue melting and subsequent wound condensation and closure upon cooling. This motor particle assisted tissue welding was demonstrated in beef liver, beef meat and chicken meat. This approach demonstrated advantage with wound healing of a mouse when compared with medical sutures and laser only welding.[107] The nanomotor based approach is not only minimally invasive (as it is not introducing new trauma and wounds as conventional stitches) but also controllable at nanometer scale (tissue glues are usually not controllable and correctable once applied at the wound area).

To achieve bone crack area targeted drug delivery and spur growth of new bone tissues, Sen's group utilized positive ion gradients generated by bone cracks for guiding of charged therapeutic particles (Figure 1.9III). Negatively charged particles (quantum dots and enzymes urease) moved towards cracks while positively charged particles moved away from cracks. When loading negatively charged poly(lactic-co-glycolic acid) (PLGA) nanoparticles with sodium alendronate, drug for treating osteoporosis, the particles could migrate towards the bone crack and achieve targeted delivery.[108]

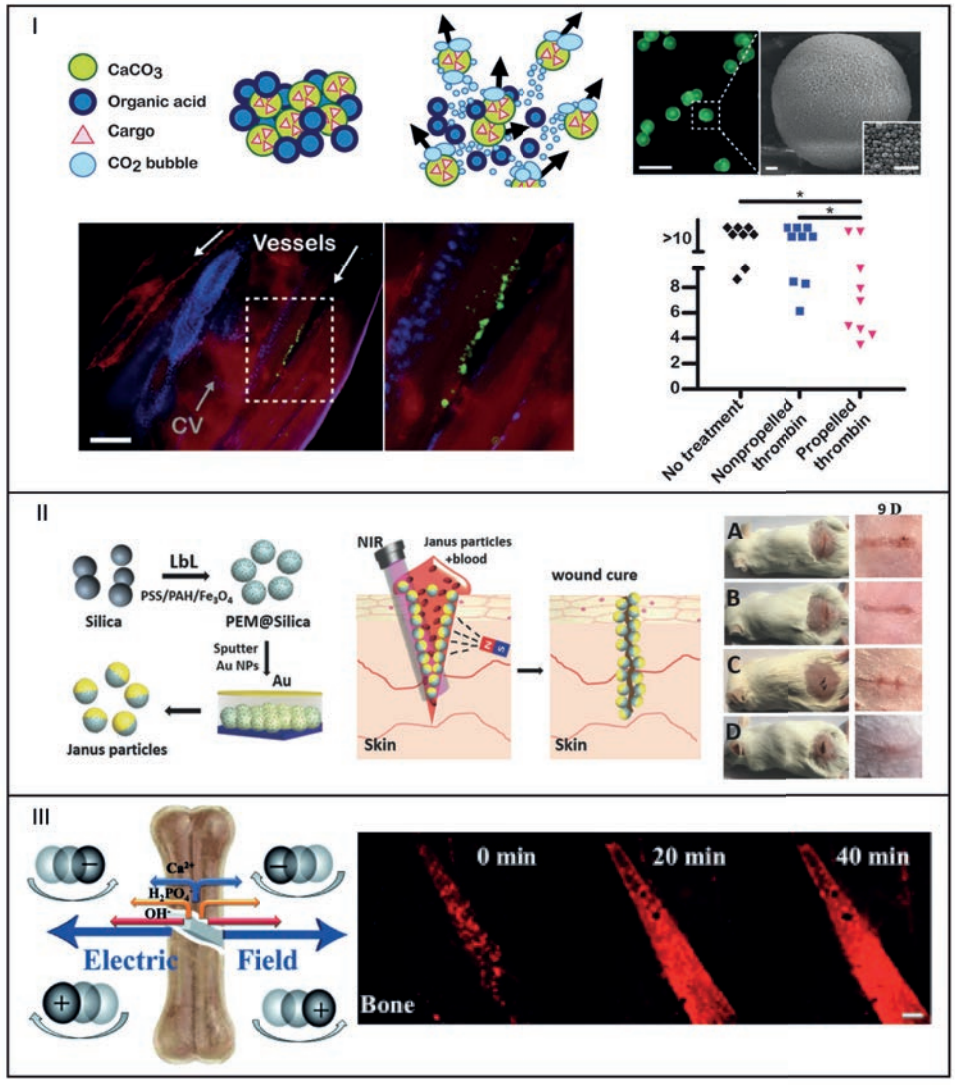

Figure 1.9. (I) Protonated tranexamic acid (fuel) loaded calcium carbonate microparticles can propel autonomously and travel inside an amputated mouse tail vessel. When incorporating green fluorescent cargo FITC-dextran, their presence in blood vessel can be clearly seen. Loaded with coagulation activating thrombin, the micromotors penetrating deep into wound can shorten the bleeding time efficiently after the tails being amputated, reproduced with permission[110], Copyright 2015, AAAS. (II) With near-infra red irradiation, gold sputtered silica Janus motors can facilitate wound welding. With a mouse model, it was shown that after 9 days the motor based tissue glue was superior (picture in the bottom, D) in assisting wound healing compared with no treatment, laser welding and suturing, reproduced with permission[107], Copyright 2016, Wiley-VCH. (III) Negatively charged quantum dots (red fluorescent) can be attracted towards cracked bone following ion gradients generated in the crack vicinity. The increasing fluorescence along prolonging time near the crack indicates the particle accumulation process, reproduced with permission[108], Copyright 2013, Wiley-VCH.

1.3.2.2. Thrombolysis

We have presented above many application examples of nanomotors demonstrating linear movements. Besides the translational motors, rotary motors in nature are also responsible for many important biological events. For instance, F0F1-ATP synthase is a type of rotary motor complex which comprises of F0 motor protein, F1 motor protein and a rotary shaft. F0 protein is embedded in the membrane while F1 is the extramembrane part of the synthase.[114] With a proton gradient across the mitochondria membrane and proton passing through F0, the complex can undergo a conformational change (rotation of central shaft) and F1 convert adenosine diphosphate (ADP) to ATP. ATP is the energy source for almost every biological process. Efforts have also been made to fabricate synthetic rotating motors and put them to application. Zhao's group used a local fluid flow produced by rotating motors for rapid drug dispensing and blood clotting treatment in a controlled way. Blood clotting in cerebral blood vessels and the resulting stroke are considered to be second leading cause for death and disability in adult human. Yet administration of free diffusing tissue plasminogen activator (t-PA), a therapeutic drug, to the body could result in systematic intracranial haemorrhages. With an external rotating magnetic field, nickel nanorods fabricated by Zhao's team rotated in the suspension. After setting up a blood clot model in a PDMS channel, magnetized nanorods and t-PA were placed in the vicinity of the blood clots. The nanomotors were activated with external rotating magnetic field and the rotation of nanorods was found to enhance the convection and accelerated the thrombolysis speed up to 2 fold. The drug dispensing process can be highly controlled by varying both the nanorod concentration and the magnetic field efficiency. The efficiency of the nanomotor enhanced thrombolysis has also been demonstrated in a rat embolic model.[115]

1.3.2.3. Surgical tools

Since the concept of minimal invasive surgery being brought up, the effort to reduce the operation trauma at each stage is ever growing.[116] Minimal incision/robot assisted precision cutting is the first step to start with. To do this, minimal invasive surgical tools or miniaturized surgical devices are used. The results of current minimal invasive practice are encouraging yet it remains a bottleneck for treating malign tissues deep inside or tissues localized closely to the vasculature systems. To realize the goal of treating more while hurting less, there is a demanding need for novel minimal invasive tools. Various types of micromotors were developed for minimal invasive surgery tools. Being micro or nanometer scale, the motors present minimal invasive cuts and are beneficial for subsequent wound recovery.

Using a multilayer microfabrication, Gracias' group designed microgrippers with sizes varied from 300 μm to 1.5 mm. The microgrippers consisted of two parts: a rigid region composed of ferromagnetic nickel and a flexible stress powered actuators with a

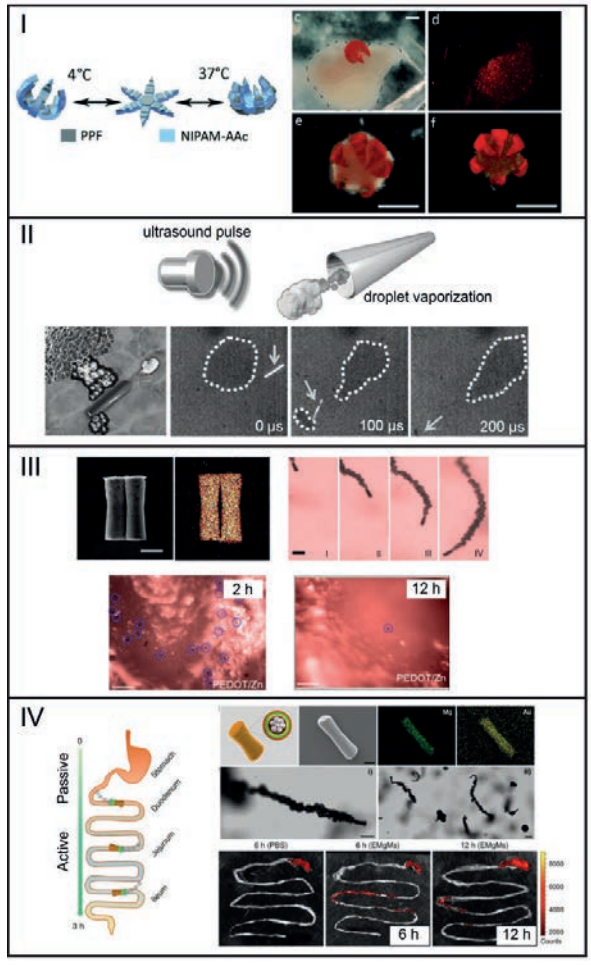

Figure 1.10. (I) Thermal actuation of microgrippers; tissue excision with a thermally triggered microgripper, reproduced with permission[117], Copyright 2014, Wiley-VCH. (II) Under sonication, perfluorocarbon emulsion loaded in tubular motors vaporized rapidly and propelled the motor forward; the thrust was used for penetrating lamb tissue, reproduced with permission[112], Copyright 2012, Wiley-VCH. (III) Water powered PEDOT-Mg motor stabbed into mucus layer of a mouse stomach and retained even after 12 h, reproduced with permission[48], Copyright 2015, American Chemical Society. (IV) PEDOT-Mg motor with enteric coating selectively activated in intestine and penetrated into intestinal wall, the fluorescently labeled motors were retained and visible after 12 h, reproduced with permission[113], Copyright 2016, American Chemical Society.

thermosensitive polymer poly(N-isopropylacrylamide) (pNIPAM) layer. The nickel segment allows for easy guidance and retrieval with a magnetic catheter. The microgrippers stayed open at room temperature and closed within 10 minutes after temperature was elevated to body temperature. It was found feasible to perform tissue excision with the microgrippers from a real organ (bile duct of porcine liver).[111] To increase the multifunctionality of the microgrippers, in another investigation by the same group, model drug doxorubicin, mesalamine and fluorescein were loaded into the porous network poly(N-isopropylacrylamide-co-acrylic acid) (pNIPAM-AAc) (Figure 1.10I). The loaded model drug eluted from the microgrippers up to 7 days.[117] In this case the micromachines functioned as both surgical tools and drug delivery carriers.

Sanchez's group reported the use of a ferromagnetic rolled-up microtube with a sharp tip for tissue surgery.[118] Incorporation of a thin ferromagnetic iron layer facilitated external magnetic field manipulation. With a pig liver section, the ferromagnetic microtube could be guided to target location, start drilling and make incision.

For surgical tools with greater thrust, Wang and coworkers made use of ultrasound powered perfluorocarbon (PFC)-loaded microbullets (MB) for tissue penetration and cleaving. Anionic perfluorocarbon emulsion was confined into the cysteamine decorated interior of a tubular micromotor through electrostatic interaction. Ultrasound pulses triggered the vaporization of perfluorocarbon emulsion from the interior of the tubular micromotor (Figure 1.10II). The generated great thrust produced linear motion with ultrafast speed of 6.3 m s^{-1}. The PFC-loaded MB was shown to penetrate, cleave and expand a dense lamb kidney tissue.[112]

A PEDOT acid driven microtube motor with acid reactive zinc deposited on its surface developed by the same group was found to be able to use locally available gastric acid as fuel and generate hydrogen bubbles as propulsion thrust. The microtubular motors remained stable and functional for 10 min in the stomach environment. The propulsion of the micromotors was demonstrated to improve the penetration into the gel like mucus layer of the stomach wall as well as increasing their retention time (Figure 1.10III). After 12 hours of administration, micromotors were still observed in the stomach tissue despite acid degradation and digestive system movement.[48]

Using similar magnesium microparticles loaded PEDOT/Au microtubes, the same group later demonstrated the possibility of gastrointestinal (GI) tract delivery. The reaction of Mg and water generated robust propulsion for the whole system. By covering the micromotors with a pH sensitive enteric coating which only dissolves in intestinal fluid (pH 6-7), the micromotors were only activated in the intestinal segment when Mg was exposed (Figure 10IV). By loading a fluorescent dye Rhodamine 6G to the micromotor, the biodistribution of microtubular motors after oral administration could be examined by fluorescence imaging. It was found the coating thickness had a strong influence on the microtube biodistribution. Compared with inert silica particles loaded microtubes, the Mg incorporated microtube

motors demonstrated an increased retention in the gastrointestinal (GI) tract as higher fluorescence signal was observed. This was attributed to the propulsion of microtubes and increased chance of collision/penetration into intestinal mucus layer.[113]

Excellent examples have been demonstrated with a wide range of micro/nanomotors piercing into various tissues. Yet there are many steps to go before using these motors in surgery. Firstly, intelligent surgical tools responsive to the diseased environments are needed. For precise and site specific surgery, more control including speed and direction over the micro/nano surgical tools needs to be gained. It is also necessary to develop techniques to retrieve the micro/nano tools after incision, otherwise biodegradable tools are necessary. Micro/nanomotors capable of performing multiple incisions consecutively are required for solving complicated medical tasks. More micro/nanomotors with varied shape and size are to be developed to expand the toolbox for micro/nano surgery and address different needs.

1.3.2.4. Imaging

The advance of medicine is accelerated by enhanced tools of observation and imaging. Nowadays medical vision is at the core of accurate diagnosis and is essential for precise surgery.[119] Only precise imaging can make it possible for surgeons to remove small patches of malignant tissues. Yet for diseased tissue specific imaging, novel imaging tools are demandingly needed. Researchers have endeavoured to apply nanomotors in the field of imaging. Deploying the catalytic decomposition of endogenous hydrogen peroxide generated by inflamed tissues, ultrasonic sensing combined with a motor system made it possible to detect abscess *in vivo*. Mattrey's group manufactured layer by layer catalase-coated nanosphere converters for hydrogen peroxide detection and imaging in an abscess model in rats. The highly efficient nanosphere converters consumed hydrogen peroxide from the local environment and produced microbubbles which were detectable by ultrasound imaging. In the case of abscess induced by bacterial invasion, activated neutrophils released excessive hydrogen peroxide. With catalase-coated nanosphere converters, ultrasound signals were detected at the abscess area.[120] Since inflammation is central to the development of various disorders, from atherosclerosis to cancer, the application scope and potential of this technique are highly relevant.

Despite recent progress made in applications with tissues, many challenges remain. In most cases, motor applications were demonstrated with tissues *ex vivo* or more static tissues. New applications at tissue level are in need to be developed.

1.3.3. APPLICATIONS IN BODY FLUID AND MATRIX

1.3.3.1. Transportation in blood

For intraveneously administrated micro/nanoparticles, blood is the first medium of contact as well as hurdle before reaching target tissues.[121] Once entering the blood stream, synthetic micro/nanomotors face destructive attack from blood which is composed of a complex mixture of water, protein and cells. In a process named opsonization, plasma proteins bind to external particles and result in subsequent particle removal by macrophage cells in liver and spleen. In addition to blood protein, blood cells can interact with foreign particles leading to shortened blood retention or systematic elimination. For both prolonged blood retention time and continuous functioning in blood, motors need to be specially designed or functionalized with specific coatings. Much research was devoted to investigate the performance/potential application of motors in blood and ways to improve their transporting abilities. Wang and his team successfully loaded iron oxide nanoparticles into red blood cells (RBC) using a hypotonic dilution/encapsulation method (Figure 1.11I). While the asymmetric distribution of loaded magnetic nanoparticles/aggregates inside the blood cell facilitates propulsion by ultrasound, the blood cell membrane on its surface provides good blood biocompatibility and reduces immune attack possibility. When guided by external magnetic field, the motor could navigate precisely along a predetermined route in undiluted whole blood. With J774 murine microphage uptake assay, it confirmed the assumption that the RBC motor evaded the uptake by microphages.[62]

With knowledge about the nonfouling property of red blood cell membrane, Wang and Zhang *et al.* wrapped gold nanowires with red blood cells membrane to serve as biomimetic sponge. The presence of the red blood cell membrane coating on the surface of the motors provided superior compatibility and alleviated the possibility of biofouling (unspecific protein adsorption) in biological medium. In the presence of red blood cell membrane perforating toxin melittin, the motors can act as decoy and protect red blood cells from lysis efficiently.[122]

Guan *et al.* fabricated a Mg/Pt-Poly(N-isopropylacrylamide) (pNIPAM) Janus micromotor. Through reaction between Mg and H_2O, the micromotors can autonomously move in simulated body fluid and human blood plasma despite the high viscosity and possible protein attachment to catalytic active sites (Figure 1.11II). With a layer of thermosensitive PNIPAM hydrogel, model drug FITC could be loaded into the PNIPAM hydrogel shell of micromotors at 4 °C and subsequently released at elevated temperature (20 °C, 37 °C). The release mechanism is due to molecules being squeezed out when PNIPAM layer shrank above its volume phase transition temperature as well as the faster diffusion of molecules at higher temperature. Via a hemolysis experiment, no significant hemoglobin release was observed indicating the blood compatibility of the motor system and the induced motion.[123]

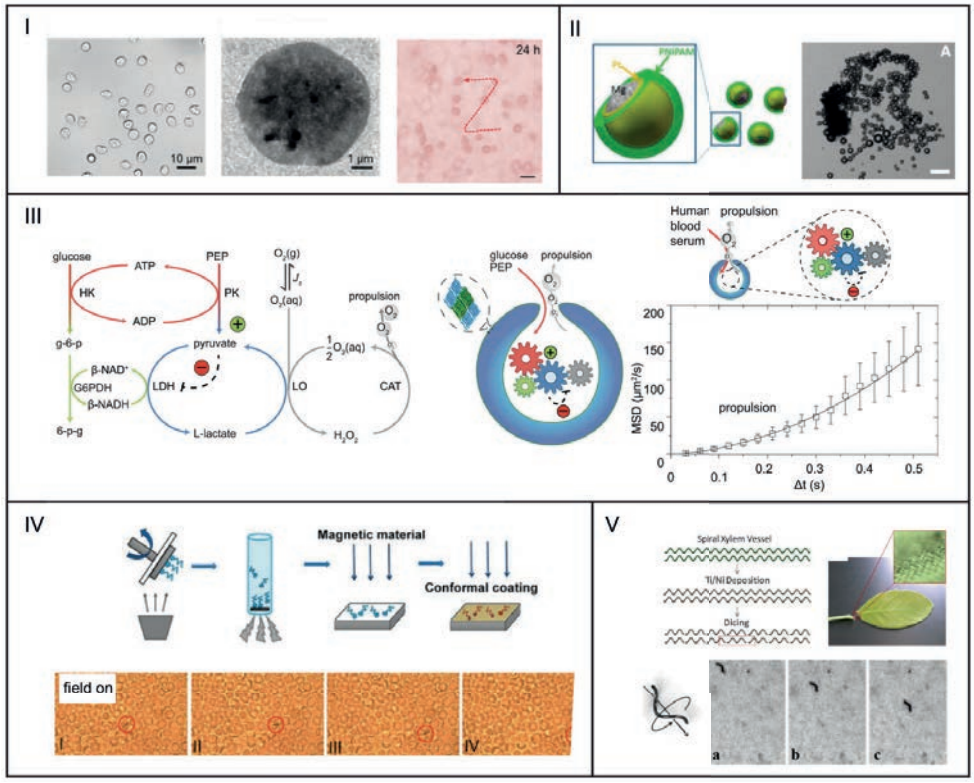

Figure 1.11. (I) Iron oxide loaded red blood cells moved under magnetic navigation in whole blood, reproduced with permission[62], Copyright 2014, American Chemical Society. (II) Fabrication process of Mg/Pt-Poly(N-isopropylacrylamide) (PNIPAM) Janus micromotor and its propulsion in human plasma, reproduced with permission[123], Copyright 2014, American Chemical Society. (III) Encapulation of metabolic network into stomatocytes motors allows conversion of blood glucose into motion, reproduced with permission[124], Copyright 2016, American Chemical Society. (IV) Helical nanopropellers moved in fresh human blood jammed with red blood cells, reproduced with permission[125], Copyright 2014, American Chemical Society. (V) Helical microswimmers derived from water conducting vessels of plants moved in serum, reproduced with permission[126], Copyright 2014, American Chemical Society.

In addition to using metal-water reaction to provide propulsion in blood, enzymes or enzyme cascades can be a good option. Wilson/Van Hest and coworkers designed an enzymatic network driven motor consisting of four cycles (Figure 1.11III). The metabolic pathway enabled the conversion of glucose and phosphoenolpyruvate into oxygen. Encapsulating the metabolic network into the outer compartment of stomatocytes polymersome, the locally produced oxygen could propel the polymersome motor. With multiple feedback loops, the oxygen conversion could be sustained at an “out of equilibrium state” and rationally tuned by the network components. Using human blood serum as the

medium, the glucose (4 mM) and L-lactate (0.08 mM) in the blood were sufficient to power the motion of the whole system.[124]

While rod or sphere motors have shown to be mobile in blood, it has been hypothesised that helical shaped motors would be more efficient in overcoming drag of viscous blood. Ghosh *et al.* used a magnetic helical nanoswimmer and explored the improvement in chemical stability towards biofluids with ferrite coatings on its surface (Figure 1.11IV).

With a rotating magnetic field, the ferrite coated helical motors propelled in fresh human blood via a corkscrew movement, which was considered advantageous for overcoming high viscosity drag. The nanopropellers showed an interesting stick and slip dynamics in this media which was thought to be related to jamming and subsequent unjamming of red blood cells.[125] Helical architectures can also be found in nature. Wang's group used spiral water-conducting vessels from different plants as template and deposited titanium and nickel on its surface to fabricate a new type of biohybrid helical microswimmers (Figure 1.11V). Under rotating magnetic field, the plant derived microswimmers demonstrated a fast motion (85 μm/s) in human serum. Compared to its velocity in pure water (90 μm/s), no significant decline in speed indicates negligible impact of body fluids on the propulsion behavior.[126]

The possible influence of motor shape on speed in blood and interaction between plasma proteins remain however to be explored. Only a few researchers have set out to investigate the relationship between motor surface coating and stability. It has been demonstrated that coating micro/nanomotors with a layer of biocompatible materials is a direct and easy way to increase biocompatibility and stability. Yet more research efforts are needed for comprehensive knowledge of blood motor interaction and optimal motor configuration.

The performance of motors, especially nanomotors in the presence of more realistic dynamic blood flow is to be investigated. While the nanomotors, compared to its micron sized counterparts, can readily access diseased sites through blood vessels even capillaries, they are more susceptible to Brownian motion due to the small size. The swimming velocity, energy conversion efficiency and directional control are important parameters still to be improved.

1.3.3.2. Transportation in urine and saliva

Urine and saliva are two types of biological fluids that are both complicated in composition. Urine, a byproduct of body metabolism, constitutes of water, inorganic salts, hormones, proteins and various metabolites such as urea and uric acid. Saliva, a watery substance secreted by salivary glands, is rich in electrolytes, glycoproteins, antimicrobial agents, enzymes and epithelial cells. In both cases catalytic motors propelled by diffusiophoresis, electrophoresis will suffer efficiency loss and metal motors are susceptible to corrosion. Here external field driven motors are superior. For propulsion in urine, Wang's team fabricated a magnetically powered flexible gold-silver-nickel nanowire motor by partially etching away the middle silver segment of a rigid gold-silver-nickel rod. In resemblance of

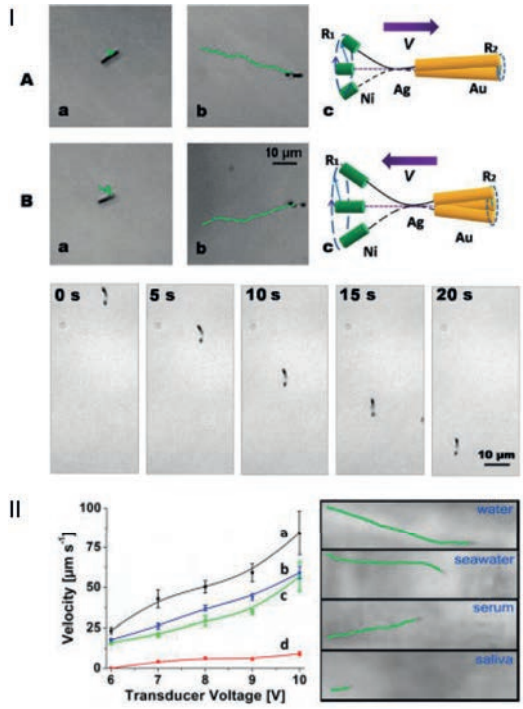

Figure 1.12. (I) With a rotating magnetic field, gold-silver-nickel nanowire propelled in urine sample, reproduced with permission[46], Copyright 2010, American Chemical Society. (II) Under ultrasound field, Au/Ni/Au nanowires demonstrated directional motion in various biological media including saliva, reproduced with permission[127], Copyright 2013, American Chemical Society.

microorganisms moving with rotating flagella, the nanowire could be propelled forward or backward with a clockwise/anticlockwise rotating magnetic field (Figure 1.12I). In undiluted urine sample (high salt medium), the nanowire still displayed an efficient locomotion.[46]

For propelling in saliva, the same team used ultrasound as fuel source. Through a template electrodeposition method, they developed a three segment Au/Ni/Au (0.25 μm in diameter, 0.8 μm/0.2 μm/0.8 μm respectively in length) nanowire. A sacrificial copper layer was deposited at one end for later creation of a concave structure. The asymmetric shape allowed for fast propulsion with ultrasound. The nickel segment facilitated precise magnetic manoeuvring. By modifying the motor surface with lectin and Con A, the micromotor was shown to selectively capture *E. coli* bacteria and *S. Aureus* bacteria.

The motor could retain its moving abilities in untreated serum and saliva (Figure 1.12II). Yet in saliva a substantial decrease in motor speed was observed as saliva is of high viscosity and of complicated molecular composition. With an electropolymerization approach, a negatively charged polypyrrole-polystyrene sulfonate segment was introduced to the Au/

Ni/Au motor. Through electrostatic interaction, brilliant green (BG) model antiseptic drug was absorbed and loaded. By changing to an acidic media after drug loading, up to 95% release in the first 120 min was demonstrated.[127]

1.3.3.3. Transportation in biological matrix

As one out of two important components of tissue (the other is cell), the extracellular matrix is an interconnected gel-like mesh network of fibrous proteins or glycosaminoglycans (GAGs) to provide biochemical and structural support for the cells. Major components include collagen, elastin, fibronectin, hyaluronan (HA) and heparin sulfate. Fischer and coworkers demonstrated a gel model with HA. HA has been reported to form strong interconnected network and is found in high concentration in vitreous humor of the eye and synovial fluid of the joint. The group engineered a silica-nickel based helical nanopropeller with the glancing angle deposition technique (GLAD). After being magnetized in plane, the nanoscrews were responsive to a rotating magnetic field and rotated along their long axis. With their chiral shape, these nanoscrews displayed efficient propulsion in viscous medium including 3 mg/mL HA solution. The concentration used corresponds to that in synovial fluid.[128]

The same group later reported the use of screw-like propellers for penetration into mucin gel. The mucin gel formed from mucin glycoproteins upon acidification is a major composition of viscoelastic layer on the surface of the stomach which prevents the efficient entrance of drug carriers. Inspired by the bacterium *Helicobacter pylori* which uses urease catalyzed urea hydrolysis to increase local pH and liquefy the mucin gel, the group coupled urease to helical micropropellers fabricated through the GLAD technique. A shell of alumina (Al_2O_3) was deposited on the surface to protect the propellers from acid corrosion. While urease free micropropellers rotated in response to a rotating field, forward propulsion was not observed which was due to absorption and immobilization to the mucus gel matrix. In the presence of urea, urease functionalized micropropellers were able to liquefy the gel and actively propel/penetrate into the mucin gel.[106]

Besides pure gel, Wilson and coworkers demonstrated motion in a tumor cell laden collagen gel in mimicking tumor tissue.[129] This part will be demonstrated in Chapter 4.

For propulsion in body fluids, biocompatibility of fuel/motors and stability of motors are important issues.[130] Alkali metal based motor systems use biological friendly water for propulsion. Generated hydrogen bubbles are responsible for propulsion once the systems come into contact with water. However the metallic engines undergo gradual corrosion in the media and release harmful metal ions. The dramatic galvanic corrosion also leads to another side effect, shortened lifespan of micro/nanomotors themselves. Biological media parameters such as pH and ionic strength could even speed up the process.[131] More attention is to be given towards development of resistant motors and discovery of alternative biocompatible fuels.

Besides problems related to the design of the motor systems, the inherent properties of

body fluid also remain a huge hurdle for real application of nanomotors. The presence of biomolecules such as protein, sugar, high ionic strength and pH may lead to inactivation of catalytic spots and motor paralysis (especially motors propelled via diffusiophoresis and electrophoresis mechanism). For motors powered by bubble recoil, biological molecules can suppress bubble detachment. Biomolecules in body fluid may react and attach unspecifically to the motor systems. Physical properties of blood and other body fluids affect the motors performance. In the highly viscous biological fluids, inertia cannot sustain movement while applied momentum can be quickly counteracted by the viscous drag from the medium. The cargo towing forces of current synthetic motors have to be improved to transport heavy cargoes.

1.4. CONCLUSIONS

Still in its infancy, the potential scope for *in vivo* application of the micro- and nanomotors are very broad and still expands.[132] In this paper we have highlighted recent excellent examples of micro/nanomotors in cellular, tissue and body fluid/biological matrix applications. Over the last decade pronounced efforts have been made for the design and fabrication of synthetic motors. Due to the extended availability of motor types and fuels, it becomes feasible to expand the *in vivo* application scope of the artificial machines even further to what is already discussed here. The limitation to the field may only be limited by imagination concerning the practical applications with these new entities.

While significant progresses have been made, challenges remain. For more broad application scope, micro/nanomotors with increased sophistication and versatility shall be developed. Functionalizing motors with different functional groups and targeting moieties is an important step for using motors as an integral platform for multiple aims. Adaptive motors with multiple operation mechanism and functions are required for addressing complicated real life tasks. As the relatively large drag force of body fluid presents a problem, motors with higher fuel conversion efficiency are needed for more efficient delivery *in vivo*. Intelligent motors able to follow environmental physical (temperature) or chemical cues (pH, signaling molecules) are desirable for autoguidance. Such self-navigating capabilities may ensure the motor systems not going astray *in vivo* in complicated vasculature systems before reaching the targeted diseased sites. Biocompatibility and biodegradability of synthetic motors are pressing issues considering motors' fate after mission completion and long term impact on the body.

Yet with multidisciplinary cooperation going on, the field is growing at a very fast pace. We envision the application of micro/nanomotors in vivo to be very useful and maybe not far away from its first trial in clinical practice.

1.5. AIM OF RESEARCH

Improving healthcare is one of society's main concerns, and has been topic of decades of intense research. Although much has been achieved, progress is still regarded limited when cancer, diabetes and other chronic diseases are considered. For instance, the 5 year survival rate for people bearing glioblastoma is only 4-17% (age dependent) while the side effects caused by antitumor therapies are high. The low success rate of treating these diseases is in a large extent caused by the limitation of current drug delivery strategies. For current delivery strategies, on one hand non-specific targeting drugs or off-target drugs can cause harm to healthy cells and diseased cells simultaneously; on another hand many drugs or drug carriers have difficulty to enter the target cells efficiently even after locating to the vicinity of the diseased cells. Therefore low targeting specificity and cell entry efficiency remain challenges to solve for biomedical researchers.

Concerning the specific drug delivery, current and conventional targeted drug delivery in chemotherapy is divided into passive targeting and active targeting. In the passive mode, drugs circulate in the vascular system until passing through leaky tumor vasculature formed by rapid tissue growth found in tumors. Leaky vasculature allows drugs to diffuse out of the vessels and consequently become retained in the surrounding extracellular matrix. In the active mode, although carriers may be similar to that in the passive method, targeting moieties are attached to drug carriers leading to increased interaction between drug carriers and specific receptors on tumor cells and consequently an enhanced entry into the cells. However both of these methods require drug carriers to be deposited passively in the vicinity of the tumor tissue. The efficiency of targeted drug delivery by current methodologies is limited and drugs failing to reach target areas result in systemic non-specific toxic effects. Therefore an exploration of alternative approaches for effective targeting delivery is required. In this thesis we use bowl-shaped polymer vesicles, named stomatocytes, which are loaded with catalytic particles that enable the particles to move in presence of fuel molecules. In **chapter 2** we pursue the use of the concept of chemotaxis (controlled movement in a gradient of fuel) to guide the stomatocyte nanomotor carriers to target cells. Chemotaxis is a strategy nature adopted to guide the motion of organisms and cells. For instance sperm can be steered towards egg during fertilization in this way. We hypothesize if nanomotors demonstrated a fuel concentration dependent motion increase, then the motors are expected to demonstrate more displacement at the fuel richer side than the fuel poorer side when placed in a fuel gradient. A net displacement towards the fuel rich zone is expected. We then set out to test whether our anti-tumor drug (doxorubicin) loaded stomatocytes nanomotors exhibit such behavior.

After achieving targeted delivery to the vicinity of the cells, we need to go one step further "into the cell". With the conventional drug carriers, even when the therapeutic agents are located in the vicinity of target cells, the interaction between carriers and

tumor cells is more or less a random and passive process. The hydrophobic and intact cell membrane protects cells from the entry of foreign molecules, making effective and efficient penetration of therapeutic agents into cells a challenging problem. In **chapter 3** we modified our stomatocyte nanomotor with the tat peptide, a basic domain from HIV tat protein. The tat protein is known to be responsible for assisting the virus entry into host cells. In addition we expected the fast movement of motors in the cell culture medium will increase chances of impact and interaction with cells and would further increase the chances of cellular entry. We then investigated and compared the cell entry efficiency of a passive drug carrier and an active drug carrier functionalized with natural cell penetrating peptides with both flow cytometry and confocal fluorescence microscopy technology.

The tumor tissue microenvironment differs significantly from the cell culture used for evaluation (in chapter 2 and 3). It would be interesting and relevant to explore the behavior as well as targeting delivery possibility of active motor delivery vehicles in a tumor tissue related environment. In **chapter 4** by seeding tumor model HeLa cells into a three dimensional collagen gel network matrix, we established a tumor tissue mimicking model. We planned to use the idea of magnetotaxis to steer the motion in the tissue mimicking model. The magnetic (or other external) field provides guiding possibilities on long distances. We introduced magnetic nickel metal in situ using the catalytic activity of platinum nanoparticles. By controlling the nickel deposition time, the catalytic activity of platinum nanoparticles was retained. We then explored the possibility of (magnetically/catalytically) powering and (magnetically) steering the motor system in solution and the tumor mimicking model.

In previous chapters we used bowl-shaped polymer vesicle based nanomotors. In biological systems, the blood and other body liquids are the first media to encounter for drug delivery agents. Shape and size affect the motor performance and circulation time. Therefore we set out to develop motors of different shapes. In an effort to develop motors of different shape/size in a continuous way, we explored the use of flow focusing fluidic channels in **chapter 5**. We firstly explored the possibility of obtaining vesicles of different shape and size by tuning the flow rate/ratio of the fluidic device as well as the initial polymer concentration. We then investigated whether catalytic platinum nanoparticles can be loaded into these vesicles to turn them into motors.

In **Chapter 6**, we reflect on the development of the motor field concerning the work described here. We also provide a general outlook and suggestions for future research based on the achievements provided in this thesis.

1.6. REFERENCES

[1] M. Schliwa, G. Woehlke, *Nature* **2003**, *422*, 759-765.

[2] a) M. Vicente-Manzanares, X. F. Ma, R. S. Adelstein, A. R. Horwitz, *Nat. Rev. Mol. Cell Bio.* **2009**, *10*, 778-790; b) N. Hirokawa, Y. Noda, Y. Tanaka, S. Niwa, *Nat. Rev. Mol. Cell Bio.* **2009**, *10*, 682-696; c) C. Veigel, C. F. Schmidt, *Nat. Rev. Mol. Cell Bio.* **2011**, *12*, 163-176.

[3] W. R. Browne, B. L. Feringa, *Nat. Nanotechnol.* **2006**, *1*, 25-35.

[4] R. K. Soong, G. D. Bachand, H. P. Neves, A. G. Olkhovets, H. G. Craighead, C. D. Montemagno, *Science* **2000**, *290*, 1555-1558.

[5] R. F. Ismagilov, A. Schwartz, N. Bowden, G. M. Whitesides, *Angew. Chem. Int. Ed.* **2002**, *41*, 652-654.

[6] W. F. Paxton, K. C. Kistler, C. C. Olmeda, A. Sen, S. K. St Angelo, Y. Y. Cao, T. E. Mallouk, P. E. Lammert, V. H. Crespi, *J. Am. Chem. Soc.* **2004**, *126*, 13424-13431.

[7] A. M. Fennimore, T. D. Yuzvinsky, W. Q. Han, M. S. Fuhrer, J. Cumings, A. Zettl, *Nature* **2003**, *424*, 408-410.

[8] W. Gao, A. Pei, X. M. Feng, C. Hennessy, J. Wang, *J. Am. Chem. Soc.* **2013**, *135*, 998-1001.

[9] M. Liu, T. Zentgraf, Y. M. Liu, G. Bartal, X. Zhang, *Nat. Nanotechnol.* **2010**, *5*, 570-573.

[10] a) T. R. Kline, W. F. Paxton, T. E. Mallouk, A. Sen, *Angew. Chem. Int. Ed.* **2005**, *44*, 744-746; b) B. Dong, T. Zhou, H. Zhang, C. Y. Li, *ACS Nano* **2013**, *7*, 5192-5198.

[11] A. A. Solovev, S. Sanchez, M. Pumera, Y. F. Mei, O. G. Schmidt, *Adv. Funct. Mater.* **2010**, *20*, 2430-2435.

[12] L. M. Liu, M. Liu, Y. J. Su, Y. G. Dong, W. Zhou, L. N. Zhang, H. Zhang, B. Dong, L. F. Chi, *Nanoscale* **2015**, *7*, 2276-2280.

[13] J. Guo, K. Kim, K. W. Leia, D. L. Fan, *Nanoscale* **2015**, *7*, 11363-11370.

[14] K. K. Dey, S. Bhandari, D. Bandyopadhyay, S. Basu, A. Chattopadhyay, *Small* **2013**, *9*, 1916-1920.

[15] S. Sattayasamitsathit, H. H. Kou, W. Gao, W. Thavarajah, K. Kaufmann, L. F. Zhang, J. Wang, *Small* **2014**, *10*, 2830-2833.

[16] a) X. Ma, X. Wang, K. Hahn, S. Sanchez, *ACS Nano* **2016**, *10*, 3597-3605; b) J. G. S. Moo, S. Presolski, M. Pumera, *ACS Nano* **2016**, *10*, 3543-3552.

[17] a) T. C. Lee, M. Alarcon-Correa, C. Miksch, K. Hahn, J. G. Gibbs, P. Fischer, *Nano Lett.* **2014**, *14*, 2407-2412; b) Y. F. Mei, A. A. Solovev, S. Sanchez, O. G. Schmidt, *Chem. Soc. Rev.* **2011**, *40*, 2109-2119; c) V. V. Singh, J. Wang, *Nanoscale* **2015**, *7*, 19377-19389.

[18] W. Gao, A. Pei, R. F. Dong, J. Wang, *J. Am. Chem. Soc.* **2014**, *136*, 2276-2279.

[19] S. Sanchez, L. Soler, J. Katuri, *Angew. Chem. Int. Ed.* **2015**, *54*, 1414-1444.

[20] L. K. E. A. Abdelmohsen, F. Peng, Y. F. Tu, D. A. Wilson, *J. Mater. Chem. B* **2014**, *2*, 2395-2408.

[21] D. A. Wilson, R. J. M. Nolte, J. C. M. van Hest, *Nat. Chem.* **2012**, *4*, 268-274.

[22] Y. J. Wu, Z. G. Wu, X. K. Lin, Q. He, J. B. Li, *ACS Nano* **2012**, *6*, 10910-10916.

[23] X. K. Lin, Z. G. Wu, Y. J. Wu, M. J. Xuan, Q. He, *Adv. Mater.* **2016**, *28*, 1060-1072.

[24] X. Ma, K. Hahn, S. Sanchez, *J. Am. Chem. Soc.* **2015**, *137*, 4976-4979.

[25] X. Ma, A. Jannasch, U. R. Albrecht, K. Hahn, A. Miguel-Lopez, E. Schaffer, S. Sanchez, *Nano Lett.* **2015**, *15*, 7779-7779.

[26] a) H. S. Muddana, S. Sengupta, T. E. Mallouk, A. Sen, P. J. Butler, *J. Am. Chem. Soc.* **2010**, *132*, 2110-2111; b) S. Sengupta, K. K. Dey, H. S. Muddana, T. Tabouillot, M. E. Ibele, P. J. Butler, A. Sen, *J. Am. Chem. Soc.* **2013**, *135*, 1406-1414.

[27] W. Gao, A. Pei, J. Wang, *ACS Nano* **2012**, *6*, 8432-8438.

[28] K. Kim, J. Guo, X. Xu, D. L. Fan, *Small* **2015**, *11*, 4037-4057.

[29] a) A. A. Solovev, E. J. Smith, C. C. Bof' Bufon, S. Sanchez, O. G. Schmidt, *Angew. Chem. Int. Ed.* **2011**, *50*, 10875-10878; b) Z. G. Wu, T. Y. Si, W. Gao, X. K. Lin, J. Wang, Q. He, *Small* **2016**, *12*, 577-582; c) F. Z. Mou, Y. Li, C. R. Chen, W. Li, Y. X. Yin, H. R. Ma, J. G. Guan, *Small* **2015**, *11*, 2564-2570.

[30] X. Ma, S. Sanchez, *Chem. Commun.* **2015**, *51*, 5467-5470.

[31] J. Simmchen, J. Katuri, W. E. Uspal, M. N. Popescu, M. Tasinkevych, S. Sanchez, *Nat. Commun.* **2016**, *7*, 10598.

[32] a) S. Sanchez, A. N. Ananth, V. M. Fomin, M. Viehrig, O. G. Schmidt, *J. Am. Chem. Soc.* **2011**, *133*, 14860-14863; b) Y. F. Tu, F. Peng, X. F. Sui, Y. J. Men, P. B. White, J. C. M. van Hest, D. A. Wilson, *Nat. Chem.* **2016**; c) V. Magdanz, G. Stoychev, L. Ionov, S. Sanchez, O. G. Schmidt, *Angew. Chem. Int. Ed.* **2014**, *53*, 2673-2677.

[33] a) W. Gao, X. M. Feng, A. Pei, Y. E. Gu, J. X. Li, J. Wang, *Nanoscale* **2013**, *5*, 4696-4700; b) L. Soler, S. Sanchez, *Nanoscale* **2014**, *6*, 7175-7182; c) L. Soler, V. Magdanz, V. M. Fomin, S. Sanchez, O. G. Schmidt, *ACS Nano* **2013**, *7*, 9611-9620.

[34] V. V. Singh, F. Soto, K. Kaufmann, J. Wang, *Angew. Chem. Int. Ed.* **2015**, *54*, 6896-6899.

[35] S. Sundararajan, P. E. Lammert, A. W. Zudans, V. H. Crespi, A. Sen, *Nano Lett.* **2008**, *8*, 1271-1276.

[36] D. S. Mojon, *Eye* **2015**, *29*, 225-233.

[37] D. M. Copolovici, K. Langel, E. Eriste, U. Langel, *ACS Nano* **2014**, *8*, 1972-1994.

[38] a) H. Wang, M. Pumera, *Chem Rev* **2015**, *115*, 8704-8735; b) M. Guix, C. C. Mayorga-Martinez, A. Merkoci, *Chem. Rev.* **2014**, *114*, 6285-6322.

[39] a) D. Almawlawi, C. Z. Liu, M. Moskovits, *J. Mater. Res.* **1994**, *9*, 1014-1018; b) B. R. Martin, D. J. Dermody, B. D. Reiss, M. M. Fang, L. A. Lyon, M. J. Natan, T. E. Mallouk, *Adv. Mater.* **1999**, *11*, 1021-1025.

[40] S. Fournier-Bidoz, A. C. Arsenault, I. Manners, G. A. Ozin, *Chem. Commun.* **2005**, 441-443.

[41] a) T. Mirkovic, N. S. Zacharia, G. D. Scholes, G. A. Ozin, *Small* **2010**, *6*, 159-167; b) Y. Wang, R. M. Hernandez, D. J. Bartlett, J. M. Bingham, T. R. Kline, A. Sen, T. E. Mallouk, *Langmuir* **2006**, *22*, 10451-10456.

[42] W. Gao, S. Sattayasamitsathit, J. Orozco, J. Wang, *J. Am. Chem. Soc.* **2011**, *133*, 11862-11864.

[43] G. Loget, J. Roche, A. Kuhn, *Adv. Mater.* **2012**, *24*, 5111-5116.

[44] J. G. Gibbs, N. A. Fragnito, Y. P. Zhao, *Appl. Phys. Lett.* **2010**, *97*.

[45] Y. F. Mei, G. S. Huang, A. A. Solovev, E. B. Urena, I. Moench, F. Ding, T. Reindl, R. K. Y. Fu, P. K. Chu, O. G. Schmidt, *Adv. Mater.* **2008**, *20*, 4085-4090.

[46] W. Gao, S. Sattayasamitsathit, K. M. Manesh, D. Weihs, J. Wang, *J. Am. Chem. Soc.* **2010**, *132*, 14403-14405.

[47] W. Wang, L. A. Castro, M. Hoyos, T. E. Mallouk, *ACS Nano* **2012**, *6*, 6122-6132.

[48] W. Gao, R. F. Dong, S. Thamphiwatana, J. X. Li, W. W. Gao, L. F. Zhang, J. Wang, *ACS Nano* **2015**, *9*, 117-123.

[49] W. Gao, S. Sattayasamitsathit, J. Wang, *Chem. Rec.* **2012**, *12*, 224-231.

[50] R. Golestanian, T. B. Liverpool, A. Ajdari, *Phys. Rev. Lett.* **2005**, *94*.

[51] Z. Wu, Y. Wu, W. He, X. Lin, J. Sun, Q. He, *Angew. Chem. Int. Ed.* **2013**, *52*, 7000-7003.

[52] Y. Ikezoe, G. Washino, T. Uemura, S. Kitagawa, H. Matsui, *Nat. Mater.* **2012**, *11*, 1081-1085.

[53] a) J. R. Howse, R. A. Jones, A. J. Ryan, T. Gough, R. Vafabakhsh, R. Golestanian, *Phys. Rev. Lett.* **2007**, *99*, 048102; b) P. M. Wheat, N. A. Marine, J. L. Moran, J. D. Posner, *Langmuir* **2010**, *26*, 13052-13055.

[54] L. Baraban, D. Makarov, R. Streubel, I. Monch, D. Grimm, S. Sanchez, O. G. Schmidt, *ACS Nano* **2012**, *6*, 3383-3389.

[55] J. G. Gibbs, Y. P. Zhao, *Small* **2010**, *6*, 1656-1662.

[56] J. G. Gibbs, Y. P. Zhao, *Small* **2009**, *5*, 2304-2308.

[57] A. Ghosh, P. Fischer, *Nano Lett.* **2009**, *9*, 2243-2245.

[58] O. G. Schmidt, K. Eberl, *Nature* **2001**, *410*, 168-168.

[59] G. Decher, *Science* **1997**, *277*, 1232-1237.

[60] a) X. Ma, A. C. Hortelao, A. Miguel-Lopez, S. Sanchez, *J. Am. Chem. Soc.* **2016**, *138*, 13782-13785; b) X. Ma, S. Jang, M. N. Popescu, W. E. Uspal, A. Miguel-Lopez, K. Hahn, D. P. Kim, S. Sanchez, *ACS Nano* **2016**, *10*, 8751-8759.

[61] a) T. Zhou, H. Qi, L. Han, D. Barbash, C. Y. Li, *Nat. Commun.* **2016**, *7,* 11119; b) W. L. Gao, M. Liu, L. M. Liu, H. Zhang, B. Dong, C. Y. Li, *Nanoscale* **2015**, *7*, 13918-13923.

[62] Z. G. Wu, T. L. Li, J. X. Li, W. Gao, T. L. Xu, C. Christianson, W. W. Gao, M. Galarnyk, Q. He, L. F. Zhang, J. Wang, *ACS Nano* **2014**, *8*, 12041-12048.

[63] R. Dreyfus, J. Baudry, M. L. Roper, M. Fermigier, H. A. Stone, J. Bibette, *Nature* **2005**, *437*, 862-865.

[64] S. Mitragotri, P. A. Burke, R. Langer, *Nat. Rev. Drug Discov.* **2014**, *13*, 655-672.

[65] W. J. M. Hrushesky, M. Martynowicz, M. Markiewicz, R. Vonroemeling, P. A. Wood, S. S. Delapena, *Adv. Drug Deliver. Rev.* **1992**, *9*, 1-83.

[66] M. Xuan, J. Shao, X. Lin, L. Dai, Q. He, *Chemphyschem* **2014**, *15*, 2255-2260.

[67] Z. G. Wu, X. K. Lin, X. Zou, J. M. Sun, Q. He, *ACS Appl. Mater. Inter.* **2015**, *7*, 250-255.

[68] E. L. Chng, G. Zhao, M. Pumera, *Nanoscale* **2014**, *6*, 2119-2124.

[69] M. Lopez-Lazaro, *Cancer Lett.* **2007**, *252*, 1-8.

[70] P. Schattling, B. Thingholm, B. Stadler, *Chem. Mater.* **2015**, *27*, 7412-7418.

[71] F. Hirschhaeuser, U. G. A. Sattler, W. Mueller-Klieser, *Cancer Res.* **2011**, *71*, 6921-6925.

[72] M. Guix, A. K. Meyer, B. Koch, O. G. Schmidt, *Sci .Rep.* **2016**, *6*, 21701.

[73] S. Sanchez, L. Soler, J. Katuri, *Angew. Chem. Int. Ed.* **2015**, *54*, 1414-1444.

[74] J. Wang, W. Gao, *ACS Nano* **2012**, *6*, 5745-5751.

[75] D. L. Fan, Z. Z. Yin, R. Cheong, F. Q. Zhu, R. C. Cammarata, C. L. Chien, A. Levchenko, *Nat. Nanotechnol.* **2010**, *5*, 545-551.

[76] L. Zhang, J. J. Abbott, L. X. Dong, B. E. Kratochvil, D. Bell, B. J. Nelson, *Appl. Phys. Lett.* **2009**, *94*.

[77] D. Kagan, R. Laocharoensuk, M. Zimmerman, C. Clawson, S. Balasubramanian, D. Kong, D. Bishop, S. Sattayasamitsathit, L. F. Zhang, J. Wang, *Small* **2010**, *6*, 2741-2747.

[78] S. Ahmed, W. Wang, L. O. Mair, R. D. Fraleigh, S. X. Li, L. A. Castro, M. Hoyos, T. J. Huang, T. E. Mallouk, *Langmuir* **2013**, *29*, 16113-16118.

[79] M. Liu, L. Q. Pan, H. G. Piao, H. Y. Sun, X. F. Huang, C. D. Peng, Y. M. Liu, *ACS Appl. Mater. Inter.* **2015**, *7*, 26017-26021.

[80] E. Mace, G. Montaldo, I. Cohen, M. Baulac, M. Fink, M. Tanter, *Nat. Methods* **2011**, *8*, 662-685.

[81] V. Garcia-Gradilla, S. Sattayasamitsathit, F. Soto, F. Kuralay, C. Yardimci, D. Wiitala, M. Galarnyk, J. Wang, *Small* **2014**, *10*, 4154-4159.

[82] B. E. F. de Avila, C. Angell, F. Soto, M. A. Lopez-Ramirez, D. F. Baez, S. B. Xie, J. Wang, Y. Chen, *ACS Nano* **2016**, *10*, 4997-5005.

[83] R. Garzon, G. Marcucci, C. M. Croce, *Nat. Rev. Drug Discov.* **2010**, *9*, 775-789.

[84] W. Gao, D. Kagan, O. S. Pak, C. Clawson, S. Campuzano, E. Chuluun-Erdene, E. Shipton, E. E. Fullerton, L. F. Zhang, E. Lauga, J. Wang, *Small* **2012**, *8*, 460-467.

[85] R. Mhanna, F. M. Qiu, L. Zhang, Y. Ding, K. Sugihara, M. Zenobi-Wong, B. J. Nelson, *Small* **2014**, *10*, 1953-1957.

[86] F. M. Qiu, R. Mhanna, L. Zhang, Y. Ding, S. Fujita, B. J. Nelson, *Sensor Actuat. B Chem.* **2014**, *196*, 676-681.

[87] F. Peng, Y. F. Tu, J. C. van Hest, D. A. Wilson, *Angew. Chem. Int. Ed.* **2015**, *54*, 11662-11665.

[88] L. Restrepo-Perez, L. Soler, C. Martinez-Cisneros, S. Sanchez, O. G. Schmidt, *Lab Chip* **2014**, *14*, 2914-2917.

[89] D. Cai, J. M. Mataraza, Z. H. Qin, Z. P. Huang, J. Y. Huang, T. C. Chiles, D. Carnahan, K. Kempa, Z. F. Ren, *Nat. Methods* **2005**, *2*, 449-454.

[90] A. A. Solovev, W. Xi, D. H. Gracias, S. M. Harazim, C. Deneke, S. Sanchez, O. G. Schmidt, *ACS Nano* **2012**, *6*, 1751-1756.

[91] W. Wang, S. X. Li, L. Mair, S. Ahmed, T. J. Huang, T. E. Mallouk, *Angew. Chem. Int. Ed.* **2014**, *53*, 3201-3204.

[92] S. K. Srivastava, M. Medina-Sanchez, B. Koch, O. G. Schmidt, *Adv. Mater.* **2016**, *28*, 832-837.

[93] F. Peng, Y. F. Tu, A. Adhikari, J. C. J. Hintzen, D. W. P. M. Löwik, D. A. Wilson, *Chem. Commun.* **2017**, *53*, 3.

[94] Z. G. Wu, X. K. Lin, Y. J. Wu, T. Y. Si, J. M. Sun, Q. He, *ACS Nano* **2014**, *8*, 6097-6105.

[95] J. Wu, S. Balasubramanian, D. Kagan, K. M. Manesh, S. Campuzano, J. Wang, *Nat. Commun.* **2010**, *1*, 36.

[96] B. E. F. de Avila, A. Martin, F. Soto, M. A. Lopez-Ramirez, S. Campuzano, G. M. Vasquez-Machado, W. W. Gao, L. F. Zhang, J. Wang, *ACS Nano* **2015**, *9*, 6756-6764.

[97] X. B. Xu, H. F. Li, D. Hasan, R. S. Ruoff, A. X. Wang, D. L. Fan, *Adv. Funct. Mater.* **2013**, *23*, 4332-4338.

[98] S. Sanchez, A. A. Solovev, S. Schulze, O. G. Schmidt, *Chem. Commun.* **2011**, *47*, 698-700.

[99] L. Zhang, T. Petit, K. E. Peyer, B. J. Nelson, *Nanomed. Nanotechnol.* **2012**, *8*, 1074-1080.

[100] V. Magdanz, S. Sanchez, O. G. Schmidt, *Adv. Mater.* **2013**, *25*, 6581-6588.

[101] M. Medina-Sanchez, L. Schwarz, A. K. Meyer, F. Hebenstreit, O. G. Schmidt, *Nano Lett.* **2016**, *16*, 555-561.

[102] M. M. Stanton, J. Simmchen, X. Ma, A. Miguel-Lopez, S. Sanchez, *Adv. Mater. Interfaces* **2016**, *3*, 1500505.

[103] Y. Yoshizumi, K. Okubo, M. Yokokawa, H. Suzuki, *Langmuir* **2016**, *32*, 9381-9388.

[104] S. Balasubramanian, D. Kagan, C. M. J. Hu, S. Campuzano, M. J. Lobo-Castanon, N. Lim, D. Y. Kang, M. Zimmerman, L. F. Zhang, J. Wang, *Angew. Chem. Int. Ed.* **2011**, *50*, 4161-4164.

[105] F. Kuralay, S. Sattayasamitsathit, W. Gao, A. Uygun, A. Katzenberg, J. Wang, *J. Am. Chem. Soc.* **2012**, *134*, 15217-15220.

[106] D. Walker, B. T. Kasdorf, H. H. Jeong, O. Lieleg, P. Fischer, *Sci. Adv.* **2015**, *1*, e1500501.

[107] W. He, J. Frueh, N. Hu, L. Liu, M. Gai, Q. He, *Adv. Sci.* **2016**, 9, 1600206.

[108] V. Yadav, J. D. Freedman, M. Grinstaff, A. Sen, *Angew. Chem. Int. Ed.* **2013**, *52*, 10997-11001.

[109] G. C. Gurtner, S. Werner, Y. Barrandon, M. T. Longaker, *Nature* **2008**, *453*, 314-321.

[110] J. R. Y. Baylis, J. H. Thomson, M. H. Kazerooni, A. Wang, X. St. John, A. E. Lim, E. B. Chien, D. Lee, A. Zhang, J. Q. Piret, J. M. Machan, L. S. Burke, T. F. White, N. J. Kastrup, C. J., *Sci. Adv.* **2015**, *1*, 8.

[111] E. Gultepe, J. S. Randhawa, S. Kadam, S. Yamanaka, F. M. Selaru, E. J. Shin, A. N. Kalloo, D. H. Gracias, *Adv. Mater.* **2013**, *25*, 514-519.

[112] D. Kagan, M. J. Benchimol, J. C. Claussen, E. Chuluun-Erdene, S. Esener, J. Wang, *Angew. Chem. Int. Ed.* **2012**, *51*, 7519-7522.

[113] J. X. Li, S. Thamphiwatana, W. J. Liu, B. E. F. de Avila, P. Angsantikul, E. Sandraz, J. X. Wang, T. L. Xu, F. Soto, V. Ramez, X. L. Wang, W. W. Gao, L. F. Zhang, J. Wang, *ACS Nano* **2016**, *10*, 9536-9542.

[114] G. Deckers-Hebestreit, K. Altendorf, *Annu. Rev. Microbiol.* **1996**, *50*, 791-824.

[115] R. Cheng, W. J. Huang, L. J. Huang, B. Yang, L. D. Mao, K. L. Jin, Q. C. ZhuGe, Y. P. Zhao, *ACS Nano* **2014**, *8*, 7746-7754.

[116] E. Bacha, D. Kalfa, *Nat. Rev. Cardiol.* **2014**, *11*, 24-34.

[117] K. Malachowski, J. Breger, H. R. Kwag, M. O. Wang, J. P. Fisher, F. M. Selaru, D. H. Gracias, *Angew. Chem. Int. Ed.* **2014**, *53*, 8045-8049.

[118] W. Xi, A. A. Solovev, A. N. Ananth, D. H. Gracias, S. Sanchez, O. G. Schmidt, *Nanoscale* **2013**, *5*, 1294-1297.

[119] H. Brody, *Nature* **2013**, *502*, S81-S81.

[120] E. S. Olson, J. Orozco, Z. Wu, C. D. Malone, B. Yi, W. Gao, M. Eghtedari, J. Wang, R. F. Mattrey, *Biomaterials* **2013**, *34*, 8918-8924.

[121] J. Lazarovits, Y. Y. Chen, E. A. Sykes, W. C. W. Chan, *Chem. Commun.* **2015**, *51*, 2756-2767.

[122] Z. G. Wu, T. L. Li, W. Gao, T. L. Xu, B. Jurado-Sanchez, J. X. Li, W. W. Gao, Q. He, L. F. Zhang, J. Wang, *Adv. Funct. Mater.* **2015**, *25*, 3881-3887.

[123] F. Z. Mou, C. R. Chen, Q. Zhong, Y. X. Yin, H. R. Ma, J. G. Guan, *ACS Appl. Mater. Inter.* **2014**, *6*, 9897-9903.

[124] M. Nijemeisland, L. K. Abdelmohsen, W. T. Huck, D. A. Wilson, J. C. van Hest, *ACS Cent. Sci.* **2016**, *2*, 843-849.

[125] P. L. Venugopalan, R. Sai, Y. Chandorkar, B. Basu, S. Shivashankar, A. Ghosh, *Nano Lett.* **2014**, *14*, 1968-1975.

[126] W. Gao, X. M. Peng, A. Pei, C. R. Kane, R. Tam, C. Hennessy, J. Wang, *Nano Lett.* **2014**, *14*, 305-310.

[127] V. Garcia-Gradilla, J. Orozco, S. Sattayasamitsathit, F. Soto, F. Kuralay, A. Pourazary, A. Katzenberg, W. Gao, Y. F. Shen, J. Wang, *ACS Nano* **2013**, *7*, 9232-9240.

[128] D. Schamel, A. G. Mark, J. G. Gibbs, C. Miksch, K. I. Morozov, A. M. Leshansky, P. Fischer, *ACS Nano* **2014**, *8*, 8794-8801.

[129] F. Peng, Y. F. Tu, Y. J. Men, J. C. M. van Hest, D. A. Wilson, *Adv. Mater*. **2016**, 2017, **29**, 1604996.

[130] D. Pantarotto, W. R. Browne, B. L. Feringa, *Chem. Commun.* **2008**, 1533-1535.

[131] A. Chalupniak, E. Morales-Narvaez, A. Merkoci, *Adv. Drug Deliver. Rev.* **2015**, *95*, 104-116.

[132] Z. G. Wu, X. K. Lin, T. Y. Si, Q. He, *Small* **2016**, *12*, 3080-3093.

2

Self-guided supramolecular cargo-loaded nanomotors with chemotactic behavior towards cells

This chapter has been published:
F. Peng, Y. F. Tu, J. C. M. van Hest, D. A. Wilson, *Angew. Chem. Int. Ed.*, 2015, **54**, 11662-11665.

2.1. INTRODUCTION

Chemotaxis in nature allows bacteria and immune cells to navigate along a concentration gradient towards chemical attractants or away from repellants.[1] This natural phenomenon has inspired scientists to construct synthetic motors able to demonstrate a similar behavior in vitro. Sen's group discovered that bimetallic rods and even single enzymes could show chemotactic behavior and move autonomously towards their substrates.[2] Schmidt and Sanchez's team reported that tubular microjets and Janus motors showed a deviation towards areas with a higher concentration of hydrogen peroxide.[3] Chattopadhyay and coworkers described hydrogen peroxide-driven catalytic microspheres that were guided towards alkali-rich regions.[4] These motors with chemotactic behavior offer the possibility,[5] besides application of external magnetic[6] or electric fields[7], to achieve precise directional control,[8] which is still lacking in most artificial motors. However most current chemotaxis motors suffer from limited cargo loading potential, and their size dimensions limit possible applications, for example with regard to drug delivery.

Several approaches have been followed towards biomedical application of nanomotors.[9] Nanosized self-assembled motors which can be loaded with cargo and which show chemotactic behavior have however not been demonstrated before. An interesting biologically relevant chemical signaling compound for induction of chemotaxis is hydrogen peroxide.[10] Compared to normal tissue, hydrogen peroxide is overproduced by tumor cells, which facilitates cancer cell invasion and metastasis.[11] A drug delivery system that could autonomously move in interstitial tissue, seek out the hydrogen peroxide source and deliver the antitumor agent would be a great improvement to current passively targeted drug delivery systems.

In this chapter we present a nanomotor, which meets the requirements regarding size, loading capability and directional movement. The nanomotor is based on a polymersome stomatocyte which is functionalized with platinum nanoparticles (PtNP) and loaded with a model anticancer drug, doxorubicin (Dox) as cargo. Furthermore, we demonstrate that these nanomotors show motion towards higher concentrations of hydrogen peroxide, not only artificially created chemical gradients in a microfluidic device, but also in presence of hydrogen peroxide-excreting neutrophils.

2.2. RESULTS AND DISCUSSION

Through self-assembly[12], Dox and PtNP loaded stomatocytes with an average size of 308 nm (Table 2.1) were obtained. Results from transmission electron microscopy (TEM) (Figure 2.1a-b), cryogenic transmission electron microscopy (cryo TEM)(Figure 2.2b) and 3D reconstruction (Figure 2.2c-e) indicated that the vesicles have a bowl-shaped morphology

with the PtNP entrapped in the outer cavity, while confocal laser scanning microscopy (CLSM) (Figure 2.2i) and energy-dispersive X-ray spectroscopy (EDX) (Figure 2.2h) corroborated the successful incorporation of doxorubicin. (For Dox and PtNP encapsulation efficiency, PtNP - 59.8% the percentage of stomatocytes carrying PtNP, Dox - 78.1% the percentage of loaded Dox based on the added amount, see Figure 2.3)

Table 2.1. Dynamic light scattering data of PtNP, empty stomatocytes, Dox-PtNP loaded stomatocytes, Dox loaded stomatocytes and PtNP loaded stomatocytes.

	Size(nm)	PDI
PtNP	73.9	0.109±0.03
PS-*b*-PEG stomatocyte	351.3	0.097±0.03
PS-*b*-PEG DOX PtNP stomatocyte	307.7	0.208±0.03
PS-*b*-PEG DOX stomatocyte	356.6	0.108±0.02
PS-*b*-PEG PtNP stomatocyte	325.4	0.168±0.03

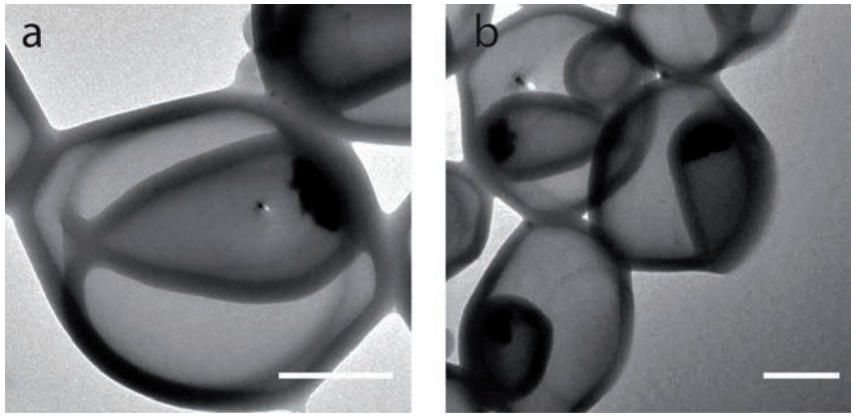

Figure 2.1. (a, b). TEM images of platinum nanoparticles and doxorubicin loaded stomatocytes, scale bar represents 100 nm.

Once the structure of the nanomotor was confirmed to have incorporated both the engine (PtNP) and the cargo (Dox) we subsequently analysed the speed of the nanomotors by using nanoparticle tracking analysis. Upon applying hydrogen peroxide, the PtNP containing stomatocytes showed a fuel concentration-dependent diffusion enhancement (Figure 2.4). The diffusion coefficient of PtNP stomatocytes experienced a remarkable increase from 1.74×10^{-8} cm^2/s in water to 2.68×10^{-8} cm^2/s upon addition of 5% (v/v) of hydrogen peroxide (final concentration was 0.15 % v/v).

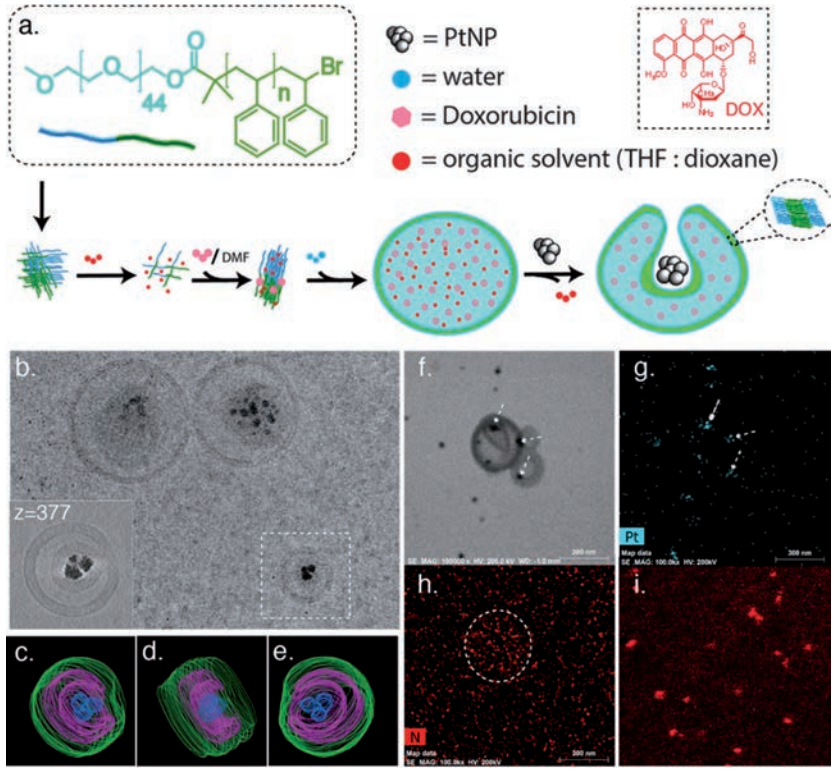

Figure 2.2. a) Procedure for preparing Doxorubicin (Dox) and platinum nanoparticle (PtNP) loaded stomatocytes; b) cryo-TEM images of Dox and PtNP loaded stomatocytes. (c-e) 3D reconstructed images of the loaded vesicle (dotted white line square in b) from cryo-TEM tomography at different angles; f) TEM images and EDX of g) Pt and h) N mapping of Dox and PtNP loaded stomatocytes. All scale bars are 300 nm; i) confocal images of PtNP and fluorescent Dox-loaded stomatocytes.

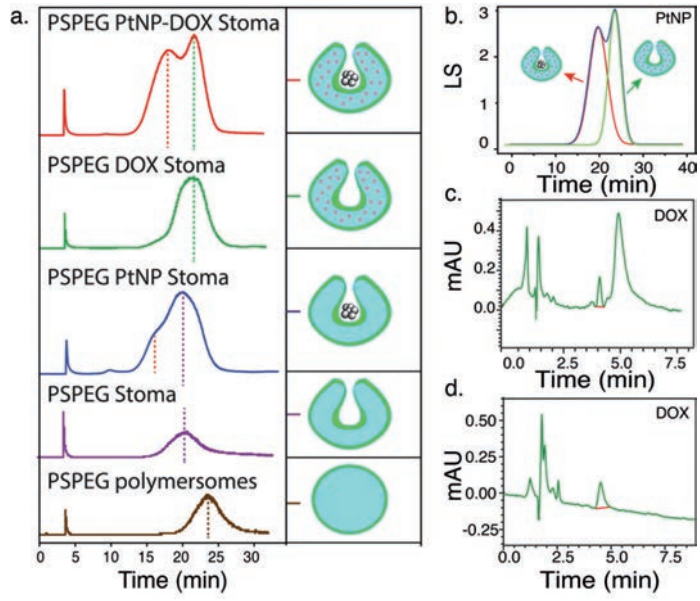

Figure 2.3. a) Field flow fractionation spectra from top to bottom of Dox and PtNP-loaded stomatocytes (red), Dox-loaded stomatocytes (green), PtNP-loaded stomatocytes (blue), empty stomatocytes (purple) and polymersomes (brown); b) Fitting of the peak area of Dox and PtNP-loaded stomatocytes. HPLC spectra of c) liberated Dox from Dox and PtNP-loaded stomatocytes and d) free Dox.

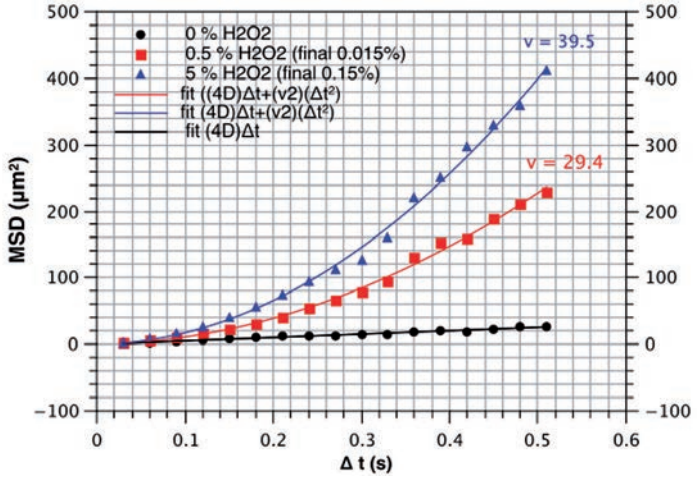

Figure 2.4. Average mean square displacement of platinum nanoparticles and doxorubicin loaded stomatocytes with addition of 0% (black circles), 0.5% (red squares) and 5% (v/v) of hydrogen peroxide (blue triangles), the final concentration of hydrogen peroxide is 0%, 0.015%, 0.15% (v/v), respectively.

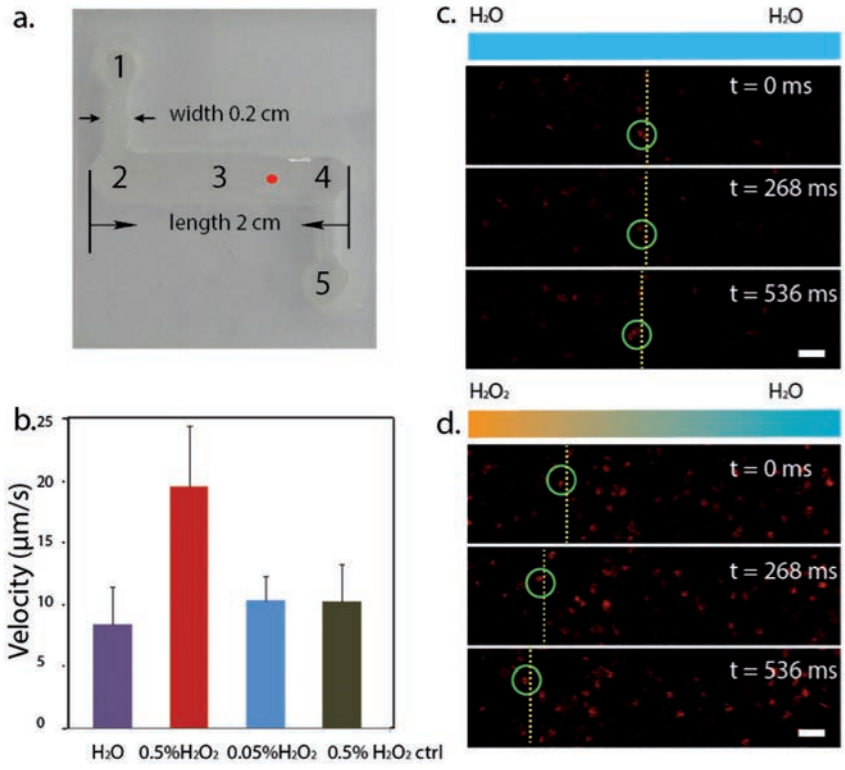

Figure 2.5. Chemotaxis evaluation in a glass channel a) the glass channel design b) average velocity of Dox and PtNP loaded stomatocytes upon addition of H_2O, 0.5% v/v H_2O_2 and 0.05% v/v H_2O_2 at position 1, or Dox loaded stomatocytes upon addition of 0.5% H_2O_2 (ctrl) after tracking 30 nanoparticles for each group; c) Motion of Dox and PtNP loaded stomatocytes upon addition of H_2O or (d) 0.5% H_2O_2. In the green circles the movement of a single particle is tracked. Scale bars represent 4 µm.

To evaluate and demonstrate the chemotactic behavior of our Dox and PtNP loaded stomatocytes, a glass flow device, similar to a PP chamber[13] for cell chemotaxis evaluation, was designed (Figure 2.5a) and confocal fluorescence microscopy was employed. The design of the channel including its size and shape was chosen so that to minimize possible drift and convection effects caused by the addition of the hydrogen peroxide/stomatocytes solution. The hydrogen peroxide concentration gradient was first demonstrated by using a hydrogen peroxide sensitive dye 2,7-dichlorodihydrofluorescein from which an optimal observation region (red spot between position 3 and 4, Figure 2.5a) was determined. In the experiment group, 5 µl of freshly prepared Dox and PtNP loaded stomatocytes was added to position 5 after the glass channel was filled with deionized water, and 5 µl of a hydrogen

peroxide solution was added to position 1 to generate a concentration gradient. In case of the 0.5% H_2O_2 experiment it was observed at the red spot position (Figure 2.5a) that tracked particles (overlaid with green circles) showed a net movement to the left where the hydrogen peroxide levels were higher (Figure 2.5d).

Similar directional movement was also observed for Dox and PtNP loaded stomatocytes in the presence of 0.05% of hydrogen peroxide, at a lower velocity (Figure 2.5b). An increase in rate along the hydrogen peroxide concentration gradient was observed.

Motors at position 4 with an average velocity of 15.47 μm/s accelerated to 19.64 μm/s at the red spot position with addition of 0.5% hydrogen peroxide, while motors with 0.05% hydrogen peroxide addition experienced a slight increase from 10.06 μm/s to 10.33 μm/s from position 4 to the red spot, confirming thus the results from the nanoparticle tracking analysis experiment. When moving up the gradient, motors travelled longer distances than by moving in the opposite direction, resulting in net motion towards the hydrogen peroxide rich area, which accounts for their chemotactic behaviour.

Control experiments were further performed and possible influences of the Marangoni effect,[14] drift effects, channel wall interaction,[15]and convection gradients[16] were ruled out. The net displacement of the nanomotors was also confirmed by observations with both microscopy and the naked eye. As the cluster of Pt-loaded nanomotors appeared dark, their displacement could be directly observed. The lack of movement in the negative control samples explains the reason we observe fewer particles in Figure 2.5c than in Figure 2.5d.

To further demonstrate the chemotactic behaviour of Dox and PtNP loaded stomatocytes, a microfluidic 2-inlet 1-outlet flow device was used (Figure 2.6). The design of the device offers

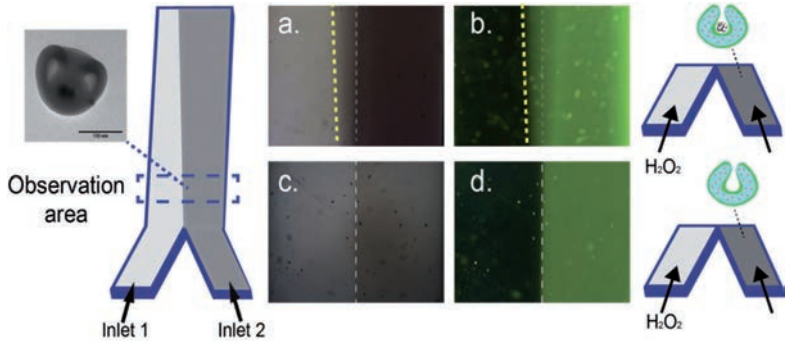

Figure 2.6. Chemotaxis evaluation in a microfluidic channel. (left) Schematic representation of the microfluidic channel. Lateral shifts of Dox and PtNP loaded stomatocytes in the presence of 0.05% H_2O_2 a) bright field b) fluorescent imaging, no deviation towards the fuel of the only Dox loaded stomatocytes in presence of 0.05% H_2O_2 c) bright field d) fluorescent imaging.

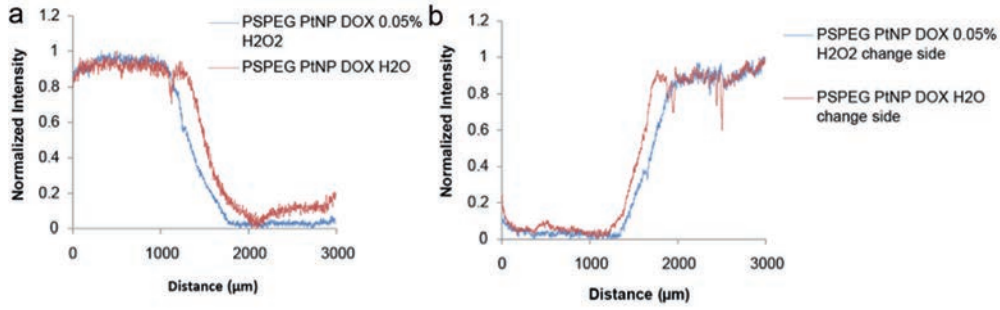

Figure 2.7. Average intensity of stacks plotted against the width of the microfluidic channel. a) Dox and PtNP loaded stomatocytes in the presence of 0.05 % hydrogen peroxide versus in the presence of water; b) Experiment in which the inlets have been inverted; Dox and PtNP loaded stomatocytes in the presence of 0.05 % hydrogen peroxide versus in the presence of water.

high controllability and flexibility over the fluid flow and concentration gradient generation. In order to establish a hydrogen peroxide concentration gradient with the least possible diffusion, the optimal flow rate through each inlet was investigated and determined to be 600 µL/h, which was maintained constant throughout the whole flow device experiment. Dox and PtNP loaded stomatocytes were pumped into the device through inlet 2 while hydrogen peroxide of 0.05% v/v was injected through inlet 1. Hydrogen peroxide with a relatively low concentration of 0.05% was chosen so as to make sure no visible oxygen bubbles would be produced immediately thereby possibly perturbing the flow profile. The particle concentration was maintained the same during the flow experiments.

Measurements started after a steady-state profile was obtained. The motors exhibited a lateral shift towards channel 1 (Figure 2.6a-b) while in the case of water instead of hydrogen peroxide only straight motion was observed and the deviation angle was close to zero (Figure 2.7).

It is possible that convection may cause bulk fluid distortion; to exclude the flow effects, control experiments with Dox only-loaded stomatocytes were performed. No deviation towards the hydrogen peroxide containing channel was observed in this case (Figure 2.6c-d). To further rule out a possible influence of the channel asymmetry or channel flow differences on the flow profile, Dox and PtNP containing stomatocytes were injected into inlet 1 and hydrogen peroxide through inlet 2. A lateral shift towards inlet 2 was observed for Dox and PtNP loaded stomatocytes (Figure 2.8, 2.7b) confirming that they move towards higher concentrations of hydrogen peroxide irrespective of the channel used.

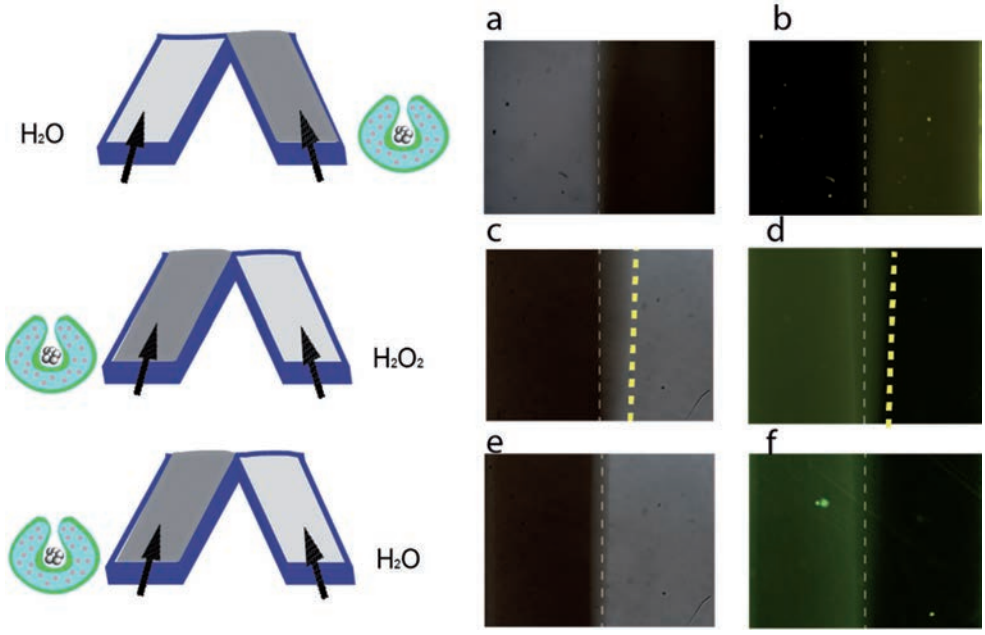

Figure 2.8. Bright field images of a) Dox and PtNP loaded stomatocytes in the presence of water, c) Dox and PtNP loaded stomatocytes in the presence of 0.05 % hydrogen peroxide with inverted inlets, e) Dox and PtNP loaded stomatocytes in the presence of water with inverted inlets. Fluorescence images of b) Dox and PtNP loaded stomatocytes in the presence of water, d) Dox and PtNP loaded stomatocytes in the presence of 0.05 % hydrogen peroxide with inverted inlets, f) Dox and PtNP loaded stomatocytes in the presence of water with inverted inlets.

After establishing the chemotactic behavior of these nanomotors, we set out to investigate if they could also respond to hydrogen peroxide gradients provided by model cells. This would provide the proof of concept of active delivery vehicles able to guide their movement towards diseased cells. We explored this possibility by using activated neutrophils as a hydrogen peroxide source.[17] Neutrophils were isolated from fresh heparinized rabbit blood.[18] The survival rate and neutrophils density of the obtained preparation was determined to be 90.9% and 1.8×10^8 cells/mL using trypan blue staining and hemocytometer counting. Then phorbol 12-myristate 13-acetate activated neutrophils were seeded into a HBSS soaked cell culture substrate before being placed into the center of a petri dish filled with Dox and PtNP loaded stomatocytes. At an observation time of 1.5 h, the nanomotors were found to be translating towards the activated neutrophils.

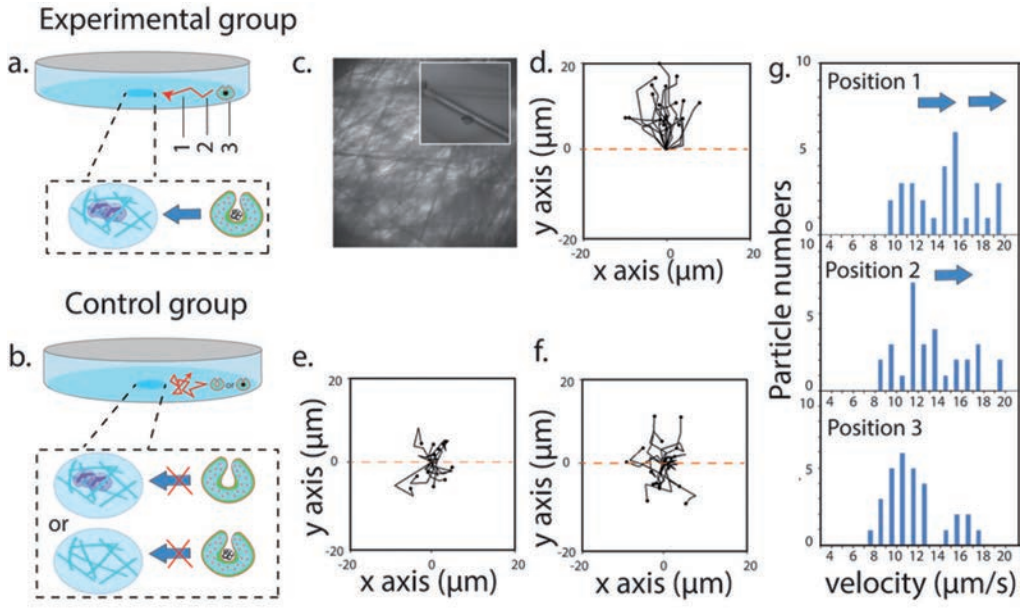

Figure 2.9. a) Experiment group set up for chemotaxis evaluation with neutrophils as hydrogen peroxide source and Dox-PtNP loaded stomatocytes in the solution; b) Control group set up using either Dox-PtNP loaded stomatocytes without cells, or neutrophils with Dox-only loaded stomatocytes; c) Bright field microscopy image of the center of the petri dish with the cells immobilized onto the cell culture substrate. The activated neutrophils can be observed at higher magnification in the inset; d) Tracking paths over 5 consecutive frames of the Dox-PtNP loaded nanomotors moving directionally towards the activated neutrophils, e) PtNP loaded nanomotors without activated neutrophils, f) Dox-only loaded stomatocytes with activated neutrophils, at position 1; g) Velocity distribution at position 1, 2, 3 for the experiment group a.

As a control, we placed only HBSS soaked substrate into the nanomotor-filled petri dish. No such phenomenon was observed in this case. As the substrate was immersed in the HBSS solution for 30 minutes and was kept inside the solution during the experiment, no capillary forces[19] between the substrate and air were expected to cause any directional motion of the nanomotors. Furthermore a lack of directional motion was also observed when activated neutrophils were placed into a solution of Dox-only loaded stomatocytes. After normalizing the starting point of a number of stomatocytes to zero, trajectories of particles over first 5 consecutive frames (total time interval = 1.34 s) from 3 groups could be compared. As shown from Figure 2.9 d, e, f, only the group with active neutrophils and nanomotors showed a directional movement. Shown in Figure 2.9 d, e, f is the tracking paths of nanoparticles at position 1. For the nanomotors with activated cells group, the motion at position 2 and 3 is less directional than at position 1. The distance between the center of mass or the spatial average end point and the point of origin (displacement of

center of mass) were also compared. As the nanomotors showed a preferred migration and directional movement in the presence of activated neutrophils, the displacement value of the center of mass was higher than the displacement values of the control group, which was close to zero (Table 2.2).

Table 2.2. Displacement of the center of mass of Dox-PtNP stomatocytes in presence of activated neutrophils cells (cells + motor); Dox-PtNP stomatocytes without activated neutrophils cells (HBSS + motor); Dox stomatocytes in presence of activated neutrophils cells (cells + stomatocyte) at different positions.

Displacement of center of mass (μm)	Cells+ motor	HBSS+ motor	Cells+stomatocyte
Position 1	11.2	0.4	0.7
Position 2	8.6	2	4.4
Position 3	7.3	1.2	2.4

It was also shown that the velocity of the nanomotors gradually increased as they were moving closer to substrate, varying from an average velocity of 12.4 μm/s at position 3 to an average velocity of 15.6 μm/s at position 1 (Figure 2.9g). We assume the directional motion is attributed to an enhanced motion of motors at a higher concentration of hydrogen peroxide. The multimodality of the velocity distribution could be due to the loading difference of catalytic PtNP between vesicles as observed with TEM/cryo-TEM.

2.3. CONCLUSION

We have demonstrated that nanosized soft polymer stomatocytes, loaded with platinum nanoparticles and the model drug doxorubicin, display chemotactic behavior in the presence of hydrogen peroxide gradients. Furthermore these structures can also sense hydrogen-peroxide producing cells by guiding their motion towards activated neutrophils. Chemotactic behavior can be explained by the fact that the nanomotors travel longer distances in the presence of higher concentration of fuels as their speed increases with fuel concentration, than in the opposite direction, leading to motors moving up the fuel gradient. While recent theoretical calculations pointed out the extent of enhanced tumbling/rotating motion at higher fuel zone would determine the chemotaxis direction (positive/negative) of motors,[20] the exact chemotaxis mechanism remains to be an open question.

The motors' nanosized dimensions and their ability to transport cargo make them an

interesting starting point for the development of drug carrier systems with chemotactic potential. Nanomotors with chemotactic behavior which could move against flow may find application in delivering drugs to late-stage tumours where high interstitial pressure[21] inhibits entrance of current delivery agents.[22]

2.4. ACKNOWLEDGEMENTS

We would like to thank Elisabeth Pierson, Geert-Jan Janssen from General Instruments from Radboud University Nijmegen and Pekka Kujala for assistance with the Cryo-TEM analysis and TEM-EDX experiments. Roeland Nolte is thanked for his many valuable suggestions.

2.5. EXPERIMENTAL SECTION

Materials

Unless otherwise indicated all reagents are used as received. Poly(vinyl pyrrolidone) (Mn10000), potassium tetrachloroplatinate (II), L (+) ascorbic acid, DMF, and dichloro-dihydro-fluorescein diacetate (DCFH-DA) were purchased from Sigma-Aldrich. Doxorubicin (Dox) was purchased from Bioconnect. BV. Methanol of HPLC grade was purchased from Avantor Performance Materials and used without further purification. Spectra/Por dialysis membrane with a MW cut-off of 12000-14000 was used for dialysis. All solutions were prepared with MilliQ water, which was obtained with a MilliQ QPOD purification system, with an electrical resistance > 18.2 MΩ.

Instruments

Dynamic light scattering (DLS) analysis was performed on Malvern Zetasizer Nano S with following settings: temperature 20 °C, He-Ne laser wavelength 633 nm and detector angle 173°. High performance liquid chromatography spectra were obtained on a HPLC analytical Agilent 1120. Fluorescence spectra of samples were recorded on a Perkin Elmer LS 55 Fluorescence spectrometer. For transmission electron microscopy, a JEOL 1010 Transmission Electron Microscope with MegaView Soft Imaging camera at an acceleration voltage of 60 kV was used. Cryogenic transmission microscopy and 3D electron tomography were performed on a JEOL TEM 2100 with high-quality Gatan 895 ultrascan 4000 bottom mount camera (4080x4080 pixels) incorporated.

Synthesis of poly(ethylene glycol)$_{44}$-*b*-polystyrene$_{190}$ (PEG$_{44}$-*b*-PS$_{190}$)

Poly(ethylene glycol)$_{44}$-*b*-polystyrene$_{190}$ was synthesized according to a modified literature method. ^{1}H NMR and GPC were used for monitoring the polymerization process by

determining the molecular weight of the block copolymer. The reaction was terminated once the desired MW of 24000 was attained. A block copolymer was obtained with a PDI of 1.07, according to the GPC.

Preparation of PtNP with PVP coating

20 mg poly(vinyl pyrrolidone) (PVP, MW≈ 10,000) was added to 2 mL K_2PtCl_4 (20 mM). The mixture was stirred at room temperature for 48 hours to allow full dissolution of the PVP. 35 mg ascorbic acid was dissolved in 1 mL of water before addition to the above solution. After stirring for 1 min, the resulting solution was incubated in a sonication bath (VWR Ultrasonic Cleaner Model 75D) at room temperature for 1 h. The appearance of a black color indicated the formation of PtNP. Average size of particles was determined to be 74 nm with DLS (Table 2.1).

Preparation of the Dox and platinum nanoparticles (PtNP)- loaded stomatocytes

The block copolymer poly(ethylene glycol)$_{44}$-*b*-polystyrene$_{190}$ (10 mg) was fully dissolved in 1 mL organic solvent mixture (tetrahydrofuran:dioxane = 4 : 1) before addition of 0.05 mg doxorubicin solution in DMF. Deionized water (0.35 mL) was subsequently slowly added to the solution, followed by addition of 0.65 mL preformed PtNP aqueous solution. After vigorous dialysis for at least 48 hours to remove non-entrapped Dox, Dox-loaded and PtNP entrapped stomatocytes were obtained. The average size of the obtained structures was determined from dynamic light scattering (DLS) analysis to be 308 nm (Table 2.1).

Transmission electron microscopy (TEM)

Samples were prepared with the following protocol: Freshly prepared Dox and PtNP loaded stomatocytes were diluted to the appropriate concentration. Then 6 µL of diluted sample aliquots were dropped onto carbon-coated copper grids. Excessive liquid was removed with filter paper and the grid was dried overnight at room temperature. Image acquisition was performed with iTEM software (Olympus). TEM images of Dox and PtNP loaded stomatocytes are presented in Figure 2.1.

Cryo electron microscopy and 3D tomography

A small droplet of Dox and PtNP loaded stomatocytes was placed on an EM Science TEM grid, blotted and vitrified through freeze plunging with an automatic vitrification robot, FEI Vitrobot™ Mark IV. Electron tomography was performed on a JEOL TEM 2100 with a Gatan 914 High tilt tomography cryo holder at an acceleration voltage of 200 kV. The region of interest was chosen and tilt series were acquired over 74 images from – 54 to 55 degrees. A side view of the reconstructed structure clearly showed that PtNP was in the outer cavity of the stomatocytes. (Figure 2.2) The average membrane thickness (20 nm) was obtained from measurements of 5 different regions (3 images) and analyzed with plot profile tools

of ImageJ software, a program developed by NIH and available at imagej.nih.gov/ij/. The measurements were made on vesicles with clearly visible boundaries.

Energy-dispersive X-ray spectroscopy (EDS)

Element (platinum and nitrogen) analysis was performed on a Bruker Quantax EDS system with an STEM detector incorporated.

Dynamic light scattering (DLS)

Dynamic light scattering analysis of Dox and PtNP loaded stomatocytes, Dox loaded stomatocytes, PtNP loaded stomatocytes, empty stomatocytes and PtNP in aqueous solution was performed using a Malvern Zetasizer Nano S instrument. Samples were typically loaded in Malvern disposable capillary cells. Values are averages of three measurements ± standard deviation (Table 2.1).

General procedure for Field Flow Fractionation

Samples were separated and detected by a field flow fractionation system (Eclipse, wyatt company) connected with a Shimazu HPLC pump and a DAWN multi-angle light scattering detector. MALS detectors were normalized with bovine serum albumin (BSA) before the experiment. 50 mM sodium nitrate solution was used as eluent. Membranes used at the channel bottom were cellulose (10 kD) RC 10 from Nadir. The channel flow rate was set at 3.0 mL/min. With an injection rate of 0.2 mL/min, samples were injected into the channel through a loop injector with injection amount of 10 µL and concentrated with a focusing flow rate of 1.0 mL/min. After focusing, samples were fractionated with a cross flow of 3.0 mL/min which decreased exponentially to 0 mL/min during the course of 28 min. Data was recorded and analyzed with Astra software (Figure 2.3). Spectra of Dox and PtNP loaded stomatocytes were deconvoluted with Gaussian distribution fitting, the percentage of PtNP loaded stomatocytes was determined to be 59.8 %.

Quantification of doxorubicin encapsulation efficiency with HPLC

To 250 µL of Dox and PtNP loaded stomatocytes solution 3 mL of THF was added before 30 seconds of vortexing. Then the mixture was centrifuged at 3000 g for 15 min. The obtained supernatant was evaporated before being reconstituted with 100 µL of HPLC mobile phase (methanol:water = 60:40). Standard solutions of Dox with concentrations of 50, 25, 12.5, 6.25, 3.125 µg/mL were prepared with eluent as calibration standards.

Reversed phase HPLC separation was performed with a column (Inertsil ODS-3, 5 µm, 4.6 × 150 mm) at room temperature. Isocratic elution was performed with a flow rate at 1.0 mL/min and a mobile phase consisting of methanol/water (methanol:water=60:40). The UV detection wavelength was set at 289 nm. Data was acquired and analyzed using EZ chrome software (Figure 2.3). The encapsulation efficiency of Dox was determined to be 78.1%.

Quantification of doxorubicin encapsulation efficiency with fluorescence spectroscopy

Standard solutions of Dox with concentrations of 50, 25, 12.5, 6.25, 3.125 μg/mL were prepared in deionized water. The freshly prepared standard solutions and all samples were kept in dark at room temperature. Excitation and emission band widths were both 15 nm with an excitation wavelength of 530 nm and an emission wavelength of 560 nm. The scanning speed was set at 100 nm/min. The fluorescence of Dox loaded stomatocytes solution was measured and compared to a calibration curve prepared by the series of Dox standard solutions. The encapsulation efficiency of Dox was determined to be 63.7%, lower than the HPLC-UV approach (78.1%). We speculate that the lower fluorescence values are the result of the formation of either aggregates or bundles of fibres through π–π stacking of Dox molecules inside the vesicles.

Procedure to measure nanomotors by nanosight

To investigate the motion of Dox and PtNP loaded stomatocytes and rule out a negative effect of Dox encapsulation on the efficiency of the nanomotors, nanoparticle tracking analysis was carried out with a nanosight LM10 at a magnification of 20X. Nanoparticle tracking analysis combines the laser light scattering technique with a CCD camera and is capable of tracking particles of 10 to 1000 nm size moving under Brownian or non-Brownian motion in real-time. The Stokes-Einstein equation can be used to correlate the tracking coordinates obtained from the movement of the particles with their size. The technique is complementary to dynamic light scattering (DLS), however, it provides individual particle-by-particle analysis rather than an ensemble size distribution information. Since the method provides additional visualization of the particles we used this technique to study in detail the effect of the fuel concentration on the movement of the platinum-loaded nanomotors for concentrations ranging from 2.5, 15, 50, 75 and 100 mM. In this experiment we analysed the movement of Dox and PtNP loaded stomatocytes at two concentrations of hydrogen peroxide (5 v/v % and 0.5 v/v %).

30 μL of freshly prepared hydrogen peroxide (5 v/v %, 0.5 v/v %) or Milli Q water was added to 1 mL doxorubicin and PtNP loaded stomatocytes solution with the appropriate concentration (8×10^8 particles/mL) before injection into the sample cell. A typical video of 90 seconds was recorded. By analyzing the video, x, y coordinates / positions of each particle were determined as a function of time intervals. Mean square displacements obtained by averaging over 25 particles from the major size distribution observed with Nanosight were plotted versus the time intervals (Figure 2.4). Upon 5 v/v % (final 0.15%) and 0.5 % (final 0.015%) hydrogen peroxide addition directional movement was observed. The average velocity (v) of the stomatocyte motors at these concentrations were extracted from the parabolic fit of the MSD ($\langle r^2 \rangle$) dependency in time (t) according to the equation $\langle r^2 \rangle = 4D\Delta t + (v\Delta t)^2$. The velocity of the nanomotors at these two concentrations was determined to be 29.4 μm/s and 39.5 μm/s respectively, demonstrating a good efficiency

of the nanomotors. The self-diffusiophoretic model proposed by Golestanian and co-workers postulated that the directional motion of a propelled particle is the result of both rotational and translational diffusion with two limiting forms, a parabolic component for short periods and a linear component for long periods in respect to the contribution of the rotational diffusion. The experimental MSD data obtained for our stomatocyte nanomotor indicates only a parabolic component for the Δt currently obtainable with this nanosize system, in contrast to micrometre-size particles for which tracking over many seconds is readily achievable.

The movement is therefore proportional to the added amount of hydrogen peroxide indicating Dox and PtNP loaded stomatocytes accelerate with increasing the concentration of hydrogen peroxide.

Demonstration of hydrogen peroxide concentration gradient in glass channel

A confocal fluorescence laser scanning microscope (Leica TCS SP2 AOBS) with 488 nm argon laser lines was used to obtain the data. The laser beam was focused on the sample through a 63X oil immersion objective. A pinhole of 400 µm was selected.

2,7-dichlorodihydrofluorescein (DCFH), a rapid and sensitive probe for oxygen-reactive species, can be turned into highly fluorescent 2,7-dichlorofluorescein (DCF) upon addition of hydrogen peroxide. As DCFH was supplied as 2,7-dichlorodihydrofluoresceindiacetate (DCFH-DA), 1.0 mL of 0.01 N NaOH was added to 250 µL of DCFH-DA to remove the ester groups. After incubation for 30 min, the mixture was neutralized with 5 mL of 25 mM PBS at pH 7.4. The resulting DCFH solution was stored in ice bath before use.

To demonstrate the formation of a hydrogen peroxide concentration gradient, 400 µL of freshly prepared DCFH solution was added into a clean and dried glass channel (channel height 0.5 cm, middle section length of channel 2 cm) before addition of 5 µL of hydrogen peroxide to position 1. DCF was excited with an Ar laser at 488 nm and the emission was collected at 510 – 560 nm. Three consecutive images at position 1-5 were acquired at predetermined time points and the fluorescence intensity of each image was directly quantified with ImageJ software. Using images taken before the addition of hydrogen peroxide, the background fluorescence was determined and subtracted from each image. There was a clear hydrogen peroxide gradient between position 2 and position 4. Therefore, the middle region (red spot in Figure 2.5a) between position 3 and position 4 was chosen as observation area.

Glass channel for chemotaxis evaluation

The glass channel was filled with 400 µL of deionized water. Then 5 µL of hydrogen peroxide (5 v/v % or 0.5 v/v %) was gently added to position 1 before gentle addition of doxorubicin and PtNP loaded stomatocytes to position 5. Particles were irradiated at an excitation wavelength of 488 nm and emission was detected using a band pass 530-620

nm to collect doxorubicin fluorescence. To visualize particle motion, particles were imaged as time series (100 frames, time interval between each frames ΔT = 268 ms) on a Leica TCS SP2 AOBS confocal using 63× oil immersion objective. The imaging plane and imaging time were carefully chosen and maintained throughout the whole experiment. A pinhole of 400 μm was used to achieve maximal tracking of particles before particles move out of imaging plane. Bidirectional scanning mode was used and the scanning speed was set at 1000 Hz to ensure minimal time interval 268 ms. Tracking image sequences were analyzed with ImageJ plugin manual tracking. With the x/y coordinates information, the distance a particle travelled within 268 ms time interval was determined. By averaging velocity of particle over different time intervals, average velocity of particle was obtained. For each group 30 nanoparticles were tracked and the velocity determined, giving a final average velocity.

To rule out effects of surface tension change induced by hydrogen peroxide addition, 5 μL of hydrogen peroxide at 0.5% was added to position 1 while doxorubicin loaded but PtNP free stomatocytes were added to position 5. No directional motion was observed in this case, excluding thus possible influences of the Marangoni effect, while the (random) movement of the PtNP-free stomatocytes was calculated to be 10.30 μm/s (Figure 2.5b). Although the calculated motion of the empty stomatocytes is similar to that of motors with hydrogen peroxide at 0.05% in magnitude it did not show any preferred directionality as is the case with chemotactic behaviour. In order to further exclude the possible influence of drift effects, deionized water of the same volume was added to position 1 while Dox and PtNP loaded stomatocytes were added to position 5. A moving rate of 8.44 μm/s was determined for the PtNP loaded stomatocytes. In this case, only typical Brownian-based diffusion, random in direction, was detected.

As observed in the experiment, there was no sign that stomatocytes sedimented or adhered/interacted with the glass channel wall. It is therefore unlikely the channel wall would influence the flow pattern. As oxygen bubble formation may give rise to convection gradients, low concentrations of hydrogen peroxide (0.5% and 0.05%) were used. With the addition of both 5 μL 0.5% and 0.05% of hydrogen peroxide, no visible oxygen production could be observed during the experiments, we therefore ensured that the directional migration towards higher concentrations of hydrogen peroxide was not due to microsized bubble formation and perturbation of the fluid.

Microfluidic device for chemotaxis evaluation

The chemotaxis of doxorubicin and PtNP loaded stomatocytes was studied with a Leica DM2500 fluorescence microscope equipped with a CCD camera. For fluorescence an HXP R 120W/45C lamp (Osram) was used. Excitation light (515-560 nm) guided through a dichroic mirror (580 nm) was focused onto the microfluidic channel. Excited fluorescence was collected after passing through a 590 nm long pass filter. Water and sample solution

were injected into a Y shaped microfluidic device (main channel width 3 mm, main channel length 2.4 cm) using a syringe pump (Fusion 100 Touch, KR analytical Ltd.). Flow rate for each inlet was maintained at 0.6 mL/h. Bright field images and fluorescent images in the region of interest (3500 µm down the channel) were acquired for 6–8 minutes after stabilization of flow. After being converted into stacks, bright field images were analyzed with ImageJ - z project tool. The average intensity of stacks was plotted against the width of the microfluidic channel. There was a shift for Dox and PtNP loaded stomatocytes in the presence of 0.05 % hydrogen peroxide while no such shift was observed for only Dox loaded stomatocytes.

Chemotactic evaluation with activated neutrophils as hydrogen peroxide source

To fresh heparinised rabbit blood, ice cold red blood cell lysing agent (0.16 M ammonium chloride, 0.01 M sodium hydrogen carbonate) was added (volume ratio 1:4) and incubated for 15 min. Then after centrifugation at 3000 rpm for 15 min, the cell pellet was resuspended in 10 mL 1 × HBSS buffer solution. After centrifugation at 3000 rpm for 5 min and 5 mL HBSS rinsing for 2 rounds, the cell pellet was resuspended with HBSS buffer solution. For neutrophil activation, concentrated neutrophils in HBSS (with calcium, magnesium) buffer were incubated with phorbol 12-myristate 13-acetate (final concentration 0.16 µM) at 37 °C for 2 h. The level of hydrogen peroxide was determined with an amplex red assay to be 2 mM. The activated neutrophils was seeded into HBSS soaked cell culture substrate (catalogue No SC-C048-0024, SeedEZ, USA) before placing into the center of a petri dish (50 mm in diameter, µ-Dish, ibidi, Germany) filled with Dox and PtNP loaded stomatocytes in HBSS solution (1.2×10^{10} vesicles/mL). Time lapse confocal images were taken at different positions. For confocal images, bidirectional scanning mode was used and the scanning speed was 1000 Hz. The analysis of image sequences was performed with ImageJ manual tracking plugin. The average distance nanoparticle travelled in minimal time interval was obtained as velocity of the nanoparticle. Velocity distribution diagrams of groups at different positions were shown. The median velocity of either Dox loaded stomatocytes in presence of stimulated cells or Dox and PtNP loaded stomatocytes in presence of cell-free culture substrate was lower than that of Dox and PtNP loaded stomatocytes in presence of activated cells. There was also no acceleration tendency from position 3 to position 1 for the control groups.

Discussion of the motion mechanism

Locomotion in both water and HBSS buffer is observed for our motor system. While our stomatocyte motors could be considered as a resemblance of Janus-type nanomotors, up till now, the motion mechanism of Janus motors remains under debate.

We examined the mechanism of directed movement by measuring the diffusion coefficient of our motors in deionized water and HBSS buffer upon addition of hydrogen peroxide. The

diffusion coefficient of Dox and PtNP loaded stomatocytes in the deionized water solution/ HBSS buffer solution upon addition of 0.05% (final concentration 0.0015%) hydrogen peroxide was determined to be 1.85×10^{-8} cm^2/s and 1.79×10^{-8} cm^2/s, respectively. The presence of electrolyte in HBSS buffer reduced the diffusion coefficient of motors to some extent. It is known that electrolyte diffusiophoresis based on ionic gradients generated by hydrogen peroxide decomposition and nonelectrolyte diffusiophoresis can be suppressed in strong electrolytes (NaCl, KCl) and neutral molecules (glucose) containing HBSS buffer. Poon and Ebbens discovered a strong propulsion reduction of platinum-PS Janus swimmers (diameter 2 μm) by addition of ionic species (maximum concentration 1 mM), suggesting a diffusiophoresis mechanism or self-electrophoresis resulting from a localized ionic current on the surface of catalyst. In our case the diffusion coefficient of motors in HBSS buffer (containing 138 mM NaCl, 5.6 mM glucose) with 0.05% hydrogen peroxide addition was reduced, yet still higher than that in HBSS without hydrogen peroxide (1.72×10^{-8} cm^2/s). We expect diffusiophoresis to play a role in our system, however it seems it is not the only operating mechanism. As it was reported previously platinum-based Janus nanomotors move directionally under either diffusiophoresis or bubble propelled mechanisms at the same concentration of hydrogen peroxide, depending on the roughness of catalyst. We assume that nanoscale bubbles could account for the locomotion we observed in HBSS buffer. It is somewhat surprising that diffusiophoresis is partly accountable for locomotion of 300 nm sized motors as one would expect rotational motion may interrupt the asymmetric distribution of catalyzed products. Recent studies from other groups also experimentally showed that motors propelled through phoretic mechanisms could still be operative at a size scale as low as 30 nm and are not be disrupted by self-rotation.

2.6. REFERENCES

[1] R. R. Kay, P. Langridge, D. Traynor, O. Hoeller, *Nat. Rev. Mol. Cell Biol.* **2008**, *9*, 455-463.

[2] a) Y. Hong, D. Velegol, N. Chaturvedi, A. Sen, *Phys. Chem. Chem. Phys.* **2010**, *12*, 1423-1435;b) S. Sengupta, K. K. Dey, H. S. Muddana, T. Tabouillot, M. E. Ibele, P. J. Butler, A. Sen, *J. Am. Chem. Soc.***2013**, *135*, 1406-1414.

[3] L. Baraban, S. M. Harazim, S. Sanchez, O. G. Schmidt, *Angew. Chem. Int. Ed.* **2013**, *52*, 5552-5556.

[4] K. K. Dey, S. Bhandari, D. Bandyopadhyay, S. Basu, A. Chattopadhyay, *Small* **2013**, *9*, 1916-1920.

[5] A. K. Singh, K. K. Dey, A. Chattopadhyay, T. K. Mandal, D. Bandyopadhyay, *Nanoscale* **2014**, *6*, 1398-1405.

[6] T. R. Kline, W. F. Paxton, T. E. Mallouk, A. Sen, *Angew. Chem. Int. Ed.* **2005**, *44*, 744-746.

[1] R. R. Kay, P. Langridge, D. Traynor, O. Hoeller, *Nat. Rev. Mol. Cell Biol.* **2008**, *9*, 455-463.

[2] a) Y. Hong, D. Velegol, N. Chaturvedi, A. Sen, *Phys. Chem. Chem. Phys.* **2010**, *12*, 1423-1435;b) S. Sengupta, K. K. Dey, H. S. Muddana, T. Tabouillot, M. E. Ibele, P. J. Butler, A. Sen, *J. Am. Chem. Soc.* **2013**, *135*, 1406-1414.

[3] L. Baraban, S. M. Harazim, S. Sanchez, O. G. Schmidt, *Angew. Chem. Int. Ed.* **2013**, *52*, 5552-5556.

[4] K. K. Dey, S. Bhandari, D. Bandyopadhyay, S. Basu, A. Chattopadhyay, *Small* **2013**, *9*, 1916-1920.

[5] A. K. Singh, K. K. Dey, A. Chattopadhyay, T. K. Mandal, D. Bandyopadhyay, *Nanoscale* **2014**, *6*, 1398-1405.

[6] T. R. Kline, W. F. Paxton, T. E. Mallouk, A. Sen, *Angew. Chem. Int. Ed.* **2005**, *44*, 744-746.

[7] P. Calvo-Marzal, K. M. Manesh, D. Kagan, S. Balasubramanian, M. Cardona, G. U. Flechsig, J. Posner, J. Wang, *Chem. Commun.* **2009**, 4509-4511.

[8] J. Wang, K. M. Manesh, *Small* **2010**, *6*, 338-345.

[9] a) Z. Wu, X. Lin, Y. Wu, T. Si, J. Sun, Q. He, *ACS Nano* **2014**, *8*, 6097-6105;b) Z. Wu, T. Li, J. Li, W. Gao, T. Xu, C. Christianson, W. Gao, M. Galarnyk, Q. He, L. Zhang, J. Wang, *ACS Nano* **2014**, *8*, 12041-12048;c) S. Sanchez, L. Soler, J. Katuri, *Angew. Chem. Int. Ed.* **2015**, *54*, 1414-1444;d) J. Wang, W. Gao, *ACS Nano* **2012**, *6*, 5745-5751;e) M. Guix, C. C. Mayorga-Martinez, A. Merkoci, *Chem. Rev.* **2014**, *114*, 6285-6322.

[10] P. Niethammer, C. Grabher, A. T. Look, T. J. Mitchison, *Nature* **2009**, *459*, 996-999.

[11] a) W. A. Wlassoff, C. D. Albright, M. S. Sivashinski, A. Ivanova, J. G. Appelbaum, R. I. Salganik, *J. Pharm. Pharmacol.* **2007**, *59*, 1549-1553;b) T. P. Szatrowski, C. F. Nathan, *Cancer Res.* **1991**, *51*, 794-798;c) U. E. Martinez-Outschoorn, Z. Lin, C. Trimmer, N. Flomenberg, C. Wang, S. Pavlides, R. G. Pestell, A. Howell, F. Sotgia, M. P. Lisanti, *Cell Cycle* **2011**, *10*, 2504-2520.

[12] D. A. Wilson, R. J. Nolte, J. C. van Hest, *Nat. Chem.* **2012**, *4*, 268-274.

[13] L. Kohidai, *Curr. Microbiol.* **1995**, *30*, 251-253.

[14] H. Jin, A. Marmur, O. Ikkala, R. H. A. Ras, *Chem. Sci.* **2012**, 2526-2529.

[15] G. Dunderdale, S. Ebbens, P. Fairclough, J. Howse, *Langmuir* **2012**, *28*, 10997-11006.

[16] A. R. Morgan, A. B. Dawson, H. S. Mckenzie, T. S. Skelhon, R. Beanland, H. P. W. Franks, S. A. F. Bon, *Mater. Horiz.* **2014**, 65-68.

[17] a) M. Freitas, G. Porto, J. L. Lima, E. Fernandes, *Clin. Biochem.* **2008**, *41*, 570-575;b) E. S. Olson, J. Orozco, Z. Wu, C. D. Malone, B. Yi, W. Gao, M. Eghtedari, J. Wang, R. F. Mattrey, *Biomaterials* **2013**, *34*, 8918-8924;c) F. Dallegri, G. Frumento, F. Patrone, *Immunology* **1983**, *48*, 273-279.

[18] P. Eggleton, R. Gargan, D. Fisher, *J. Immunol. Methods* **1989**, *121*, 105-113.

[19] A. A. Solovev, Y. Mei, O. G. Schmidt, *Adv. Mater.* **2010**, *22*, 4340-4344.

[20] S. Saha, R. Golestanian, S. Ramaswamy, *Phys. Rev. E* **2014**, 89, 062316.

[21] a) Y. Fan, W. Du, B. He, F. Fu, L. Yuan, H. Wu, W. Dai, H. Zhang, X. Wang, J. Wang, X. Zhang, Q. Zhang, *Biomaterials* **2013**, *34*, 2277-2288;b) X. Wang, C. Yang, Y. Zhang, X. Zhen, W. Wu, X. Jiang, *Biomaterials* **2014**, *35*, 6439-6453.

[22] I. K. Kwon, S. C. Lee, B. Han, K. Park, *J. Control Release* **2012**, *164*, 108-114.

3

Peptide functionalized nanomotor as efficient cell penetrating tool

This chapter has been published:
F. Peng, Y. F. Tu, A. Adhikari, J. C. J. Hintzen, D. W. P. M. Löwik, D. A. Wilson, *Chem. Commun.*, 2017, **53**, 3.

3.1. INTRODUCTION

The nature of the hydrophobic cell membrane and its intactness protect cells from the influx of exogeneous molecules, making efficient and effective access of therapeutic agents into diseased cells a challenging yet attractive problem.[1] Progress made in drug delivery over the last decades was considered limited, when compared to the high expectations concerning cancer and other vasculature diseases, mainly because it relied on passive delivery and accumulation in the diseased tissue. For this purpose next generation active delivery devices with strong cell penetrating abilities are in high demand. Self propelled micro or nanomotors[2] which demonstrate great potential in the realm of transportation,[3] sensing[4] and environmental remediation,[5] have been given growing attention. These motors with increased cargo towing force and direction control[6] are capable of efficient transportation at the micro and nanometer scale, showing promise in precise active delivery.[7] However, applications of nanomotors in a biological context remain still limited due to their complicated preparation, size restriction and limited possibilities for further modification. Functionalized motors with engineered properties and functions are therefore desirable. Self-assembled motors are in particular interesting soft locomotive carriers, as they provide more diversity in the choice of the building components, good interface with biological systems and could be easily modified.[8] Here we present a new type of self-assembled nanomotor, which was easily functionalized with a cell penetrating peptide. The motion of the nanoscale motors was utilized to actively interact with and facilitate uptake by tumor cells. The dynamic movement of the drug loaded nanomotors increases the likelihood of interaction between delivery agents and target cells. Cell penetrating peptides (CPPs), or protein transduction domains are capable of crossing cell membranes effectively.[9] Through electrostatic interaction with the plasma membrane, cellular binding and direct insertion, cell penetrating peptides can promote rapid membrane crossing of themselves/tagged biomolecules.[9c] Among these CPPs, one of the most successful is trans-activator of transcription (tat) peptide derived from the tat protein of human immunodeficiency virus. This basic protein domain is responsible for promoting the efficient cell entry of the virus and can facilitate a wide range of cargos to translocate rapidly across cell membranes.[10] Coupling CPPs onto synthetic nanomotors to enhance further their cell penetrating ability has not been reported yet. Such biohybrid nanomotors represent a new class of nanomotors bridging the synthetic motors with natural properties. Capability of moving efficiently and penetrating effectively, along with easy fabrication makes this nanomotor particularly attractive for cargo delivery.

3.2. RESULTS AND DISCUSSION

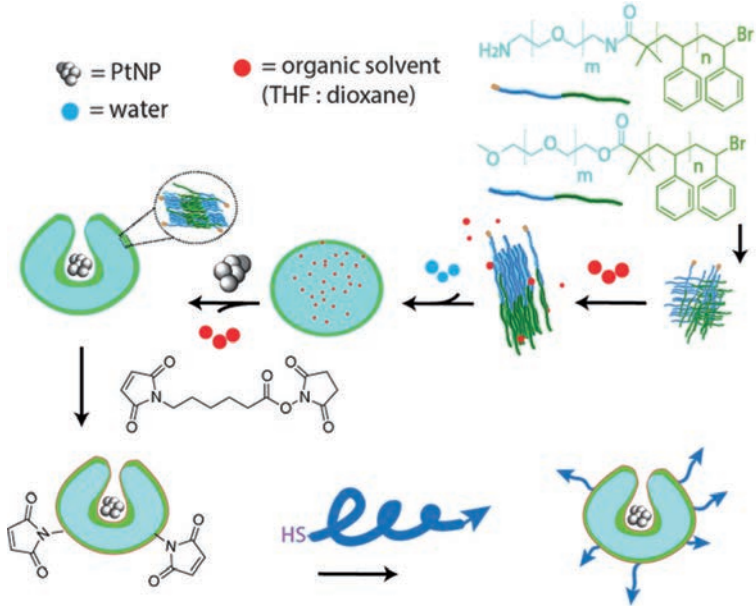

Figure 3.1. Schematic illustration of the synthetic process of tat peptide functionalized stomatocyte nanomotors.

Figure 3.1 illustrates the preparation process of tat peptide modified poly(ethylene glycol)-*b*-polystyrene stomatocyte nanomotors. Firstly carboxylic acid functional polystyrene$_{190}$ and poly(ethylene glycol)$_{44}$-*b*-polystyrene$_{190}$ were synthesized via ATRP polymerization, while amine functionalized poly(ethylene glycol)$_{66}$-*b*-polystyrene$_{190}$ was obtained by reacting the PS carboxyl end group with α,ω-amine functionalized poly (ethylene glycol) (^{1}H NMR spectrum of poly(ethylene glycol)$_{44}$-*b*-polystyrene$_{190}$ and poly(ethylene glycol)$_{66}$-*b*-polystyrene$_{190}$ with amine ending can be found in Figure 3.2). The amine groups on the poly (ethylene glycol) allow easy modification and subsequent functionalization with peptides. After synthesis of the block copolymer, platinum loaded block copolymer poly(ethylene glycol)-*b*-polystyrene based stomatocytes were obtained through self-assembly of the polymers.[11]

1% or 5% of amine functionalized poly(ethylene glycol)$_{66}$-*b*-polystyrene$_{190}$ was mixed with poly(ethylene glycol)$_{44}$-*b*-polystyrene$_{190}$. During self-assembly, preformed catalytic platinum nanoparticles were loaded into the cavity of the stomatocytes.[12] Catalytic platinum nanoparticles can provide propulsion by decomposing chemical fuel hydrogen peroxide.[6] The poly(ethylene glycol) on the surface imparts the stomatocyte motor with stealth properties and good biocompatibility in biological environments.

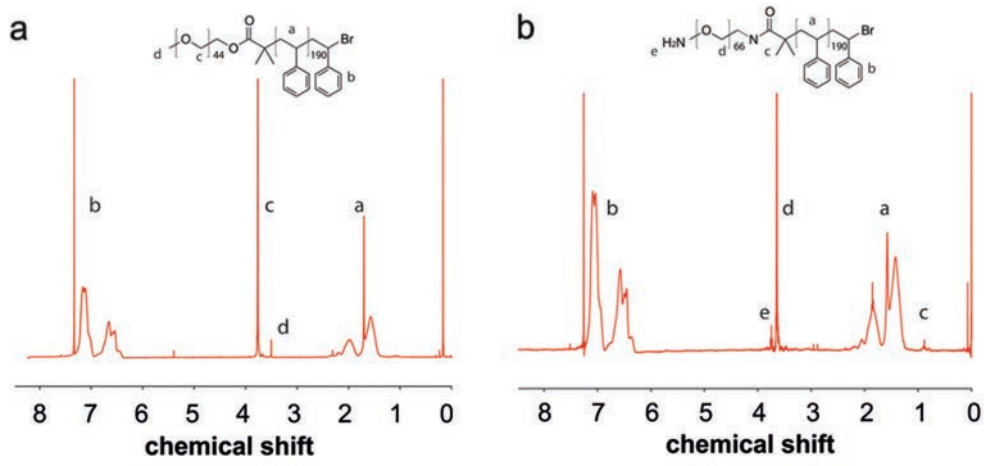

Figure 3.2. ^{1}H NMR spectrum of a) poly(ethylene glycol)$_{44}$-*b*-polystyrene$_{190}$ and b) amine functionalized poly(ethylene glycol)$_{66}$-*b*-polystyrene$_{190}$.

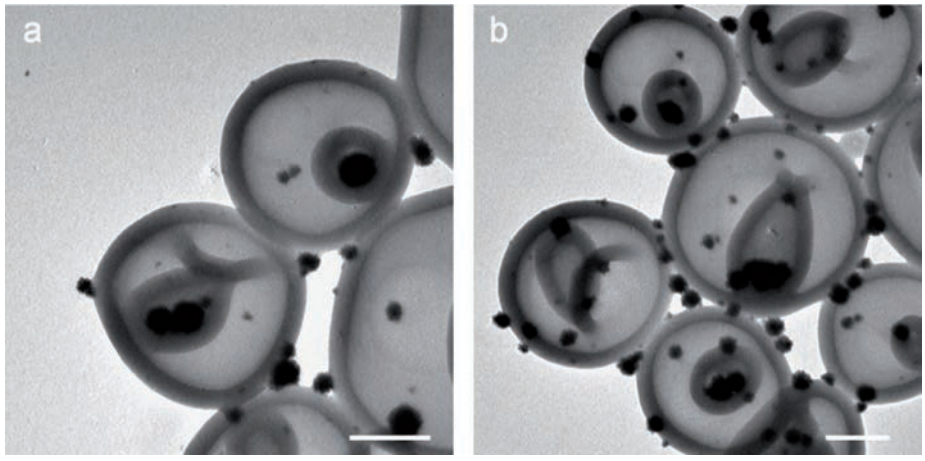

Figure 3.3. TEM images of a) 1% amine functionalized poly(ethylene glycol)-*b*-polystyrene stomatocytes; b) 5% amine functionalized poly(ethylene glycol)-*b*-polystyrene stomatocytes.

After forming platinum loaded poly(ethylene glycol)-*b*-polystyrene (1% or 5% amine) stomatocytes (Figure 3.3), the bifunctional agent 6-maleimidohexanoic acid N-hydroxysuccinimide ester was introduced on the surface via the coupling of the amine group with NHS. The maleimide groups present on the surface were then used for

modification with fluorescent fluorescein isothiocyanate (FITC) functionalized tat (Figure 3.4) through maleimide bonding with the cysteine group in tat.

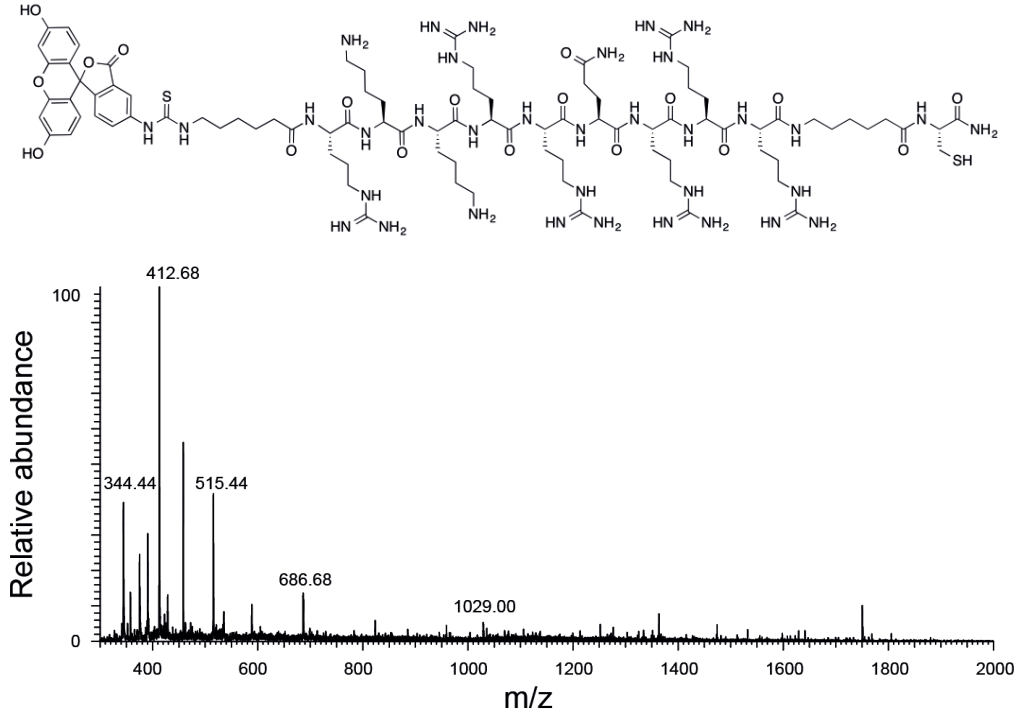

Figure 3.4. Molecular structure and electrospray ionisation mass spectrometry (ESI-MS) spectrum of FITC labelled tat peptide (expected molecular mass 2056.09), found m/z 344.44 at +6 charge, m/z 412.68 at +5 charge, m/z 515.44 at +4 charge, m/z 686.68 at +3 charge, m/z 1029.00 at +2 charge.

Three rounds of centrifugation and washing were used to remove unreacted peptide. The stomatocyte structure remained stable after FITC-tat functionalization (Figure 3.5a, b). TEM images at different tilting angle along the x axis corroborated that the platinum was indeed positioned in the cavity of the stomatocytes (Figure 3.5c-e). After tat peptide coupling, a decrease in zeta potential was observed for both 1% maleimide-functionalized stomatocytes and 5% maleimide-functionalized stomatocytes. Figure 3.5f shows a summary of zeta potentials before and after tat functionalization. For the 1% group, a slight decrease in zeta potential was observed. For the 5% group, the zeta potential experienced a more significant change from -29.3 mV for maleimide functionalized stomatocytes to -15.8 mV after tat coupling.

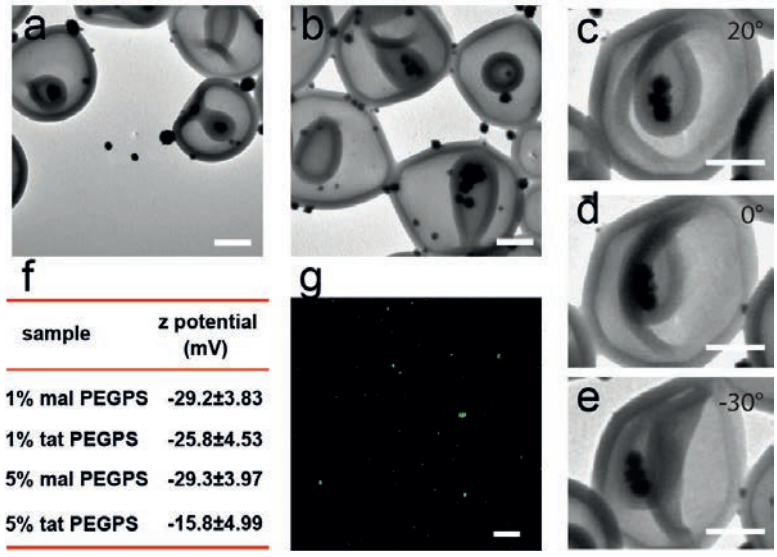

sample	z potential (mV)
1% mal PEGPS	-29.2±3.83
1% tat PEGPS	-25.8±4.53
5% mal PEGPS	-29.3±3.97
5% tat PEGPS	-15.8±4.99

Figure 3.5. Transmission electron microscopy images of a) 1% FITC-tat functionalized stomatocyte motors, b) 5% FITC-tat functionalized stomatocyte motors, scale bar is 100 nm; c-e) TEM images of one platinum loaded FITC-tat functionalized stomatocyte at different tilting angle through 20° to -30°, scale bar represents 100 nm; f) summary of zeta potential values before and after FITC-tat functionalization; g) confocal fluorescent image of 5% FITC-tat functionalized stomatocyte motors, scale bar represents 10 µm.

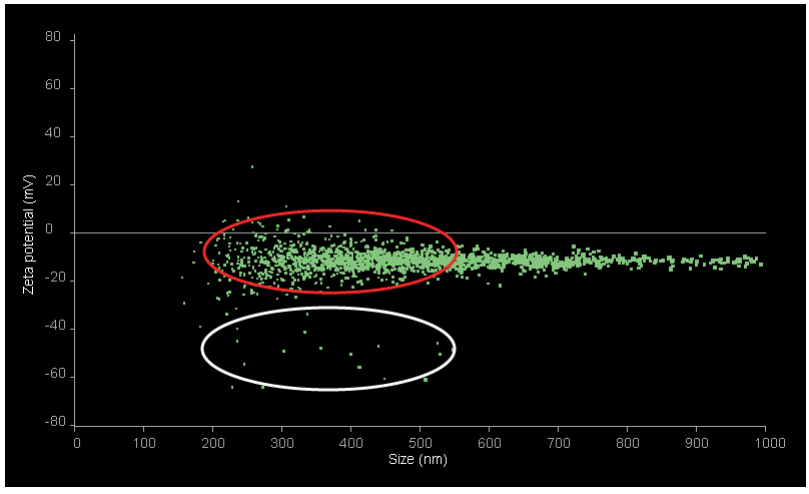

Figure 3.6. Zeta potential and size distribution of tat functionalized stomatocyte nanomotors determined with nanoparticle tracking analysis.

This indicates a higher modification percentage with tat since tat is a positively charged peptide and the introduction of tat is expected to lead to a less negatively charged surface. The decrease in the zeta potential for the 5% group was confirmed with zeta-potential measurements via nanoparticle tracking analysis (NTA). With this NTA technique it was also possible to get zeta potentials of individual particles and allow a demonstration of the charge distribution on the whole particle population. An average zeta potential of -17.2 ± 0.9 mV was obtained (Figure 3.6), correlating well with the data from DLS.

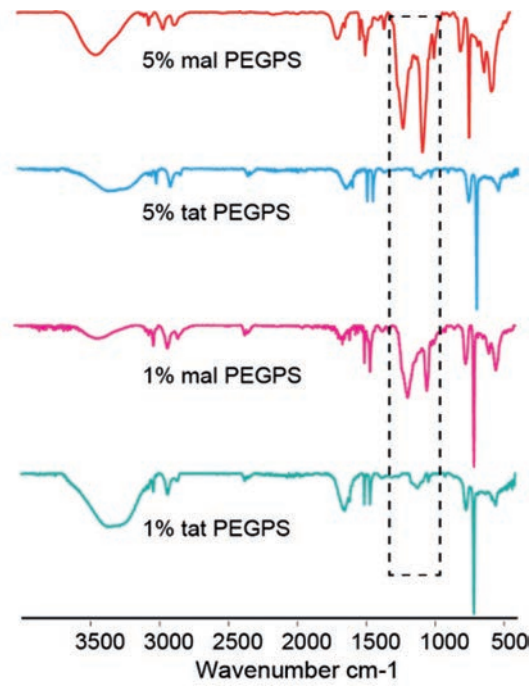

Figure 3.7. Infrared spectra of (from top to bottom) 5% maleimide-functionalized poly(ethylene glycol)-*b*-polystyrene stomatocytes; 5% tat functionalized poly(ethylene glycol) -*b*-polystyrene stomatocytes; 1% maleimide-functionalized poly(ethylene glycol)-*b*-polystyrene stomatocytes; 1% tat functionalized poly(ethylene glycol)-*b*-polystyrene stomatocytes.

From the zeta potential distribution data, it could also be observed that relatively high conjugation efficiency was obtained. According to IR spectra, a decrease in the peaks at 1260 cm^{-1} and 1040 cm^{-1} (Figure 3.7) showed the reduction of the =C-H vibration of maleimide (RCH=CHR'), indicating the successful conjugation between maleimide and cysteine of FITC-tat. Fluorescence observed with confocal fluorescent microscopy also

verified the successful ligation of peptides onto the surface of stomatocytes (Figure 3.5g). The fluorescent FITC facilitates the visualization by confocal fluorescent microscopy in subsequent cell uptake experiments.

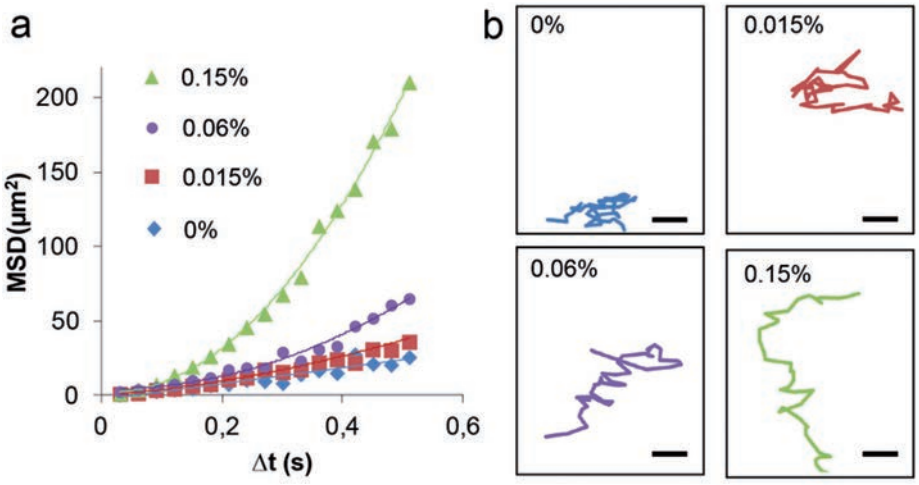

Figure 3.8. a) Plot of mean square displacement versus time intervals at different concentrations of hydrogen peroxide solution; b) tracking paths of nanomotors at different hydrogen peroxide levels, scale bar represents 6 μm.

The 5% functionalized stomatocytes motors were used for further studies. For tat free control groups, 5% amine functionalized stomatocytes were reacted with FITC. The utility of the nanomotor for cargo delivery was then tested with its directional moving capabilities. In the hydrogen peroxide solution, the tat functionalized motors preserved their ability to move. The motors clearly showed faster movement with increased level of hydrogen peroxide over the range of 0% to 0.15% (Figure 3.8a). From the MSD-Δt curve, the velocity of motors was derived with 9.3 μm/s at 0.015% hydrogen peroxide, 13.91 μm/s at 0.06% of hydrogen peroxide and 28.51 μm/s at 0.15% hydrogen peroxide. At the lowest hydrogen peroxide concentration used (0.015%), a parabolic curve was still observed, indicating a propulsive movement. The trajectory paths of stomatocyte motors at different concentrations of hydrogen peroxide solution are given in Figure 3.8b. In the absence of hydrogen peroxide, typical Brownian motion with random movement was observed. At higher levels of hydrogen peroxide, directional motion with intermittent tumbling was demonstrated.

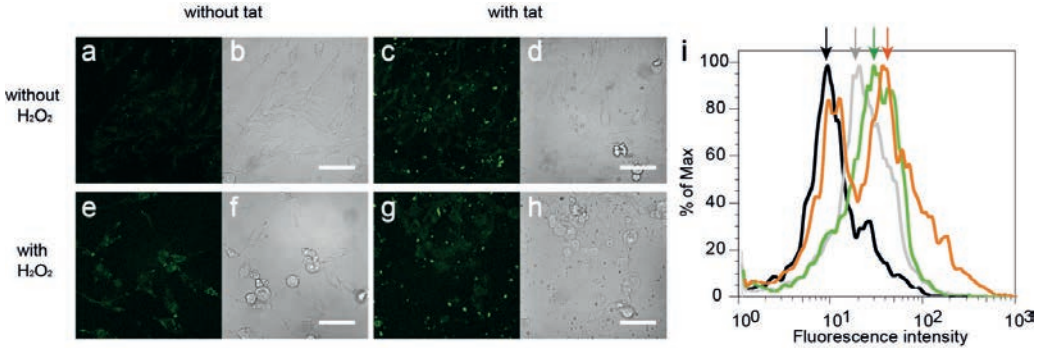

Figure 3.9. a) confocal fluorescent image and b) confocal bright field image of HeLa cells incubated with FITC PEG-PS Pt stomatocytes for 6 hours, c) confocal fluorescent image and d) confocal bright field image of HeLa cells incubated with FITC-tat PEG-PS Pt stomatocytes for 6 hours, e) confocal fluorescent image and f) confocal bright field image of HeLa cells incubated with FITC PEG-PS Pt stomatocytes in presence of 0.015% hydrogen peroxide for 6 hours, g) confocal fluorescent image and h) confocal bright field image of HeLa cells incubated with FITC-tat PEG-PS Pt stomatocytes in 0.015% hydrogen peroxide for 6 hours, scale bar represents 60 μm; i) quantitative comparison of cellular uptake for FITC PEG-PS Pt stomatocytes without hydrogen peroxide (grey curve), FITC PEG-PS Pt stomatocyte nanomotors with 0.015% hydrogen peroxide (green curve) or FITC-tat PEG-PS Pt stomatocytes nanomotors with 0.015% hydrogen peroxide (orange curve), while black curve represents basal fluorescence of HeLa cells.

HeLa cells, human cervical cancer cells were used as a model cell to investigate the cell penetrating and entry abilities of nanomotors. After incubating with FITC PEG-PS Pt stomatocytes or FITC-tat PEG-PS Pt stomatocytes for 6 hours with or without 0.015% hydrogen peroxide solution, confocal microscopy was used to visualize and evaluate the cellular uptake. From Figure 3.9, it was observed that in the presence of hydrogen peroxide there was an increased uptake of FITC PEG-PS Pt stomatocytes. A further increase was observed for the FITC-tat PEG-PS Pt stomatocytes with hydrogen peroxide group. At this low level of hydrogen peroxide, FITC-tat was robust and stable to promote effective penetration. For determination of the localization of FITC-tat PEGPS Pt stomatocytes, both cell membrane and nucleus staining agents were used. At this hydrogen peroxide level after 6 hours, the cell nucleus and cell membrane were demonstrated to remain intact.

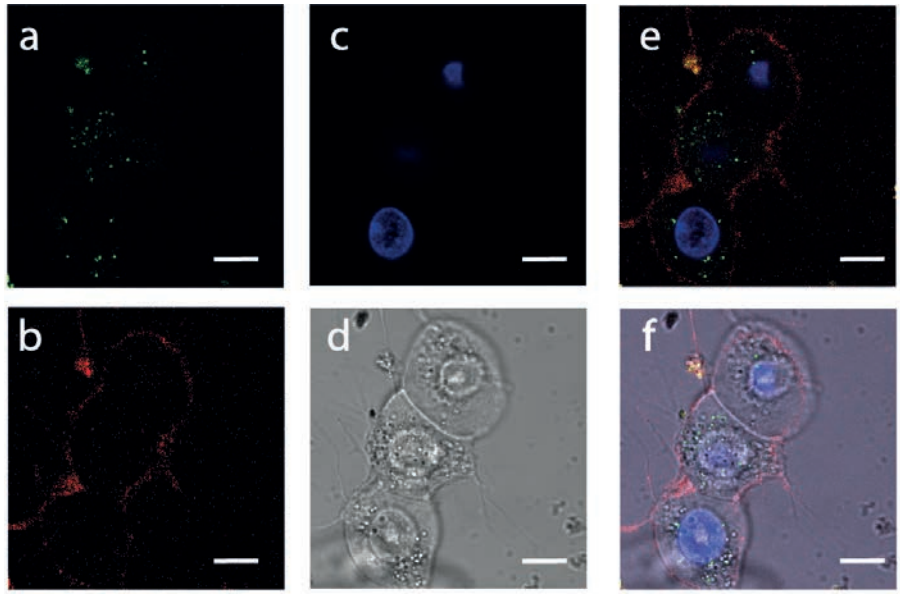

Figure 3.10. HeLa cells incubated with a) tat functionalized stomatocyte nanomotors in presence of 0.015% hydrogen peroxide for 6 hours and stained with b) cell mask deep red cell membrane stain; c) live cell nucleus dye Hoechst 33342; d) bright field image of the cells, scale bar represents 10 µm; e) merged image of a), b), c); f) merged image of a), b), c), d).

It could be observed that a significant amount of FITC-tat PEG-PS Pt stomatocytes was indeed taken up by the intact cells (Figure 3.10) while a small percentage of particles were attached onto the cell membrane which was generally acknowledged as the first step for cellular internalization. To remove the FITC-tat PEG-PS Pt stomatocytes attached onto the surface of the cell membrane and quantify the amount of stomatocytes sequestered by the cells, the cells were trypsinized and further analyzed with flow cytometry. The trypsin-EDTA used could effectively digest and dissociate the peptide functionalized stomatocytes attached to the outer membrane of cells.

An increase in the fluorescence was observed from FITC PEG-PS Pt stomatocytes (no hydrogen peroxide) to FITC PEG-PS Pt stomatocytes (in the presence of hydrogen peroxide – active nanomotors) and FITC-tat PEG-PS Pt stomatocytes (with hydrogen peroxide – functionalized active nanomotors) (Figure 3.9i), corroborating the results from confocal microscopy. For FITC-tat PEG-PS Pt stomatocytes (with hydrogen peroxide) two peaks were observed which was explained by the presence of PEG-PS Pt stomatocytes not functionalized with FITC-tat. Furthermore the zeta potential measurements with nanosight confirmed the incomplete functionalization. Two populations were observed with tat functionalized

stomatocytes at -18 - 10 mV while -50 - -30 mV was observed for unfunctionalized stomatocytes. The mean fluorescence value for FITC PEGPS Pt stomatocytes (no hydrogen peroxide), FITC PEG-PS Pt stomatocytes (hydrogen peroxide) and FITC-tat PEG-PS Pt stomatocytes (hydrogen peroxide) were respectively 26.3 ± 5.4 au, 30.5 ± 3.3 au and 50.4 ± 0.85 au while the basal fluorescence from cells was low with a value of 12.3 ± 3.7 au. We attributed the increased cell penetrating abilities for FITC-tat PEG-PS Pt stomatocytes to their directional active motion as well as the presence of tat peptide. Continuous propulsion of stomatocyte motors results in fast movement in cell culture medium, which induced faster and higher chances of motor-cell interaction. It was expected the enhanced interaction would lead to improved uptake and penetration into intact cells.

3.3. CONCLUSION

In conclusion we have demonstrated a strategy to fabricate peptide functionalized nanomotors in a simple and convenient way. By combining nanometer scale biological stealth motors with cell penetrating peptides, the motors displayed rapid and effective penetration. Such motors hold great promises for delivering agents into cells in a rapid way.

3.4. ACKNOWLEDGEMENTS

Saskia A. Bode is thanked for help with synthesis of the tat peptide. Peter van Galen is gratefully acknowledged for his help with the MS measurement of the peptide.

3.5. EXPERIMENTAL SECTION

Materials

Unless otherwise indicated all reagents are used as received. Copper bromide (CuBr), N,N,N',N",N"-pentamethyldi-ethylenetriamine (PMDETA), styrene, tert-butyl α-bromoisobutyrate, 1-phenyl-1-trimethylsiloxyethene, ethylene diamine tetra acetic acid (EDTA), α-ω-amino-poly(ethylene glycol), benzotriazol-1-yl-oxytripyrrolidinophosphonium hexafluorophosphate (PyBOP), 6-maleimidohexanoic acid N-hydroxysuccinimide ester, 4-(2-hydroxyethyl)-1-piperazineethanesulfonic acid (HEPES), Tris(2-carboxyethyl) phosphine (TCEP), polyvinylpyrrolidone (Mn10000), potassium tetrachloroplatinate (II) and L (+) ascorbic acid were purchased from Sigma-Aldrich. Tetrahydrofuran (THF), anisole and N,N-diisopropylethylamine (DIPEA) were obtained from Acros. Hydrochloric acid (37%) and hydrogen peroxide were purchased from J.T. Baker. 1,4-dioxane (Biosolve BV),

dichloromethane ($CH2Cl_2$, Fisher Chemical) were also used. Methanol of HPLC grade was purchased from Avantor Performance Materials and used without further purification. Spectra/Por dialysis membrane with a MW cut-off of 12000-14000 was used for dialysis. All solutions were prepared with MilliQ water, which was obtained with a MilliQ QPOD purification system, with an electrical resistance > 18.2 MΩ.

Instruments

Gel permeation chromatography (GPC) was performed on a Shodex GPC column equipped with UV SPD 20A detectors (254 nm, 215 nm). THF was used as eluent and the flow rate was kept constant at 1 mL/min. ^{1}H nuclear magnetic resonance spectra (^{1}H NMR) were measured on a Varian Inova 400 MHz spectrometer, with $CDCl_3$ as solvent. Dynamic light scattering (DLS) analysis was performed on Malvern Zetasizer Nano S with the following settings: temperature 20 °C, He-Ne laser wavelength 633 nm and detector angle 173°. Infrared (IR) spectroscopy was performed with an IR-ATR instrument (Bruker TENSOR 27). Transmission electron microscopy was performed with a JEOL 1010 Transmission Electron Microscope at an acceleration voltage of 60 kV.

Synthesis of poly(ethylene glycol)$_{44}$-*b*-polystyrene$_{190}$ (PEG_{44}-*b*-PS_{190})

Based on a modified literature method poly(ethylene glycol)$_{44}$-*b*-polystyrene$_{190}$ was synthesized. For monitoring the polymerization process, ^{1}H NMR and GPC were used to determine the molecular weight of the block copolymer. The reaction was terminated once the desired MW of 24000 was attained. According to the GPC, a block copolymer was obtained with a PDI of 1.07.

Synthesis of NH_2-poly(ethylene glycol)$_{66}$-*b*-polystyrene$_{190}$ (NH_2-PEG_{66}-*b*-PS_{190})

Poly(ethylene glycol)$_{66}$-*b*-polystyrene$_{190}$ with amine as ending group was synthesized as following. The schlenk tube with CuBr (45 mg, 0.32 mmol) was evacuated for 15 min and refilled with argon for three times. PMDETA (66 µL, 0.32 mmol) in anisole (0.5 mL) was added, followed by 15 min of vigorously stirring. Styrene (5.74 mL, 50 mmol) in anisole (0.5 mL) was added via a syringe and degassed for 15 min. After cooling the mixture to 0 °C, tert-butyl α-bromoisobutyrate (27 µL, 0.14 mmol) in anisole was injected and the solution was degassed for another 15 min. The Schlenk tube was transferred into an oil bath at 90 °C. ^{1}H-NMR was used for monitoring the reaction process. Upon attainment of the required molecular weight, the reaction was terminated by adding 1-phenyl-1-trimethylsiloxyethene (1.91 mL, 9.28 mmol). The mixture was left to stir for 2h. The solution was diluted with CH_2Cl_2 and extracted with an aqueous solution of EDTA (65 mM). The organic layer was collected and dried with $MgSO_4$ before concentration with a vacuum pump. The polymer obtained was precipitated in MeOH for three times and dried under vacuum overnight, giving polymer α-tert-butyloxycarbonyl-polystyrene. Then α-tert-Butyloxycarbonyl-

polystyrene (3 g) was dissolved in 1, 4-dioxane (30 mL) and concentrated HCl (1.5 mL, 37%) was added. The reaction was refluxed at 110 °C overnight. The mixture was dried using a rotary evaporator and then dissolved in CH_2Cl_2. The polymer (α-carboxylic acid-polystyrene) was obtained after precipitation in MeOH (3x) and then dried under vacuum overnight. The dried polymer α-carboxylic acid-polystyrene (1 g, 43.5 μmol), α-ω-amino-poly(ethylene glycol) (521.7 mg, 260 μmol) and DIPEA (17.4 μL, 100 μmol) were dissolved in DMF (12 mL). The solution was cooled to 0 °C and PyBOP (42 mg, 80 μmol) was added. The reaction was stirred overnight, while slowly warming to room temperature. The progress of the coupling was monitored by GPC. After that, the mixture was diluted with CH_2Cl_2 and extracted with $NaHCO_3$ solution (4 wt%) and saturated NaCl solution. The organic layer was collected and dried with $MgSO_4$ and concentrated. The pure polymer was obtained after precipitation in MeOH (3x) and dried under vacuum overnight. The final polymer was characterized by ^{1}H-NMR in $CDCl_3$.

Preparation of PtNP with PVP coating

To 2 mL K_2PtCl_4 (20 mM), 20 mg poly(vinyl pyrrolidone) (PVP, MW≈ 10,000) was added. The mixture was allowed to stir at room temperature for 48 hours. Then 1 mL ascorbic acid aqueous solution (35 mg/mL) was added to the above solution. After stirring for 1 min, the mixture was incubated in a sonication bath (VWR Ultrasonic Cleaner Model 75D) at room temperature for 1 h. The appearance of a black color indicated the formation of PtNP. The average size of particles was determined to be 74 nm with DLS.

Preparation of the platinum nanoparticles (PtNP)- loaded stomatocytes

The block copolymer poly(ethylene glycol)$_{44}$-*b*-polystyrene$_{190}$ and poly(ethylene glycol)$_{66}$-*b*-polystyrene$_{190}$ with an amine end group (for 5% functionalization, 9.5 mg: 0.5 mg; for 1% functionalization, 9.9 mg: 0.1 mg) were fully dissolved in 1 mL organic solvent (tetrahydrofuran:dioxane = 4 : 1). Deionized water (0.35 mL) was subsequently slowly added to the solution, followed by addition of 0.65 mL preformed PtNP aqueous solution. After dialysis for 48 hours, PtNP entrapped stomatocytes were obtained.

Functionalization of amine ended poly(ethylene glycol)-*b*-polystyrene stomatocytes with fluorescein isothiocyanate labelled tat peptide (FITC-tat)

The amine exposed poly(ethylene glycol)-*b*-polystyrene (2.5 mg polymer/mL) stomatocytes solution (800 μL) was diluted with 333 μL of phosphate buffer (pH 7.4, 80 mM), followed by addition of 6-maleimidohexanoic acid N-hydroxysuccinimide ester (2 mg/mL, for 5% functionalization 15 μL, 1% functionalization 3 μL). The mixture was allowed to stir vigorously for 2 hours before ultrafiltration with (4-(2-hydroxyethyl)-1-piperazineethanesulfonic acid) (HEPES) buffer for three times to remove unreacted 6-maleimidohexanoic acid N-hydroxysuccinimide ester and concentrate the solution to 4 mg polymer/mL. To 400 μL

of the obtained solution, FITC-tat (1 mg/mL) aqueous solution (for 5% 16 µL, 1% 3.2 µL), Tris(2-carboxyethyl)phosphine (TCEP, 1 mg/mL) aqueous solution (for 5% 8.2 µL, 1% 1.7 µL) and 100 µL HEPES buffer was added. The reaction mixture was agitated in the dark for 16 hours. Then three cycles of wash and centrifugation (6000 rpm, 10 min) were performed to remove unreacted FITC-tat and the stomatocytes pellet was redispersed with MilliQ water (4 mg polymer/mL).

Functionalization of amine ended poly(ethylene glycol)-*b*-polystyrene stomatocytes with fluorescein isothiocyanate (FITC)

The amine exposed poly(ethylene glycol)-*b*-polystyrene (2.5 mg polymer/mL) stomatocytes solution (800 µL) was diluted with 200 µL of borate buffer (pH 9, 80 mM), followed by addition of fluorescein isothiocyanate (FITC) in DMSO (2 mg/mL, for 5% 20 µL, 1% 4 µL). The reaction mixture was left to stir in dark before ultrafiltration for three times to remove unreacted FITC.

Transmission electron microscopy (TEM)

Samples were prepared with the following protocol: 6 µL of diluted sample aliquots were dropped onto carbon-coated copper grids. Excessive liquid was removed with filter paper and the grid was dried overnight at room temperature. Image acquisition was performed with iTEM software (Olympus).

Dynamic light scattering (DLS)

Dynamic light scattering analysis of PtNP in aqueous solution and zeta potential measurement of functionalized stomatocytes were performed using a Malvern Zetasizer Nano S instrument. Samples were typically loaded in Malvern disposable capillary cells.

Procedure to measure motion of nanomotors by nanosight

To investigate the motion of stomatocytes nanomotors, nanoparticle tracking analysis was carried out with a nanosight LM10 at a magnification of 20x. The nanoparticle tracking analysis provides visualization of the particles. We used this technique to study the effect of fuel concentration on the movement of the stomatocytes. In this experiment we analysed the movement of PtNP loaded stomatocytes at four concentrations of hydrogen peroxide (final concentration 0 v/v %, 0.015 v/v %, 0.06 v/v %, 0.15 v/v %). 30 µL of Milli Q water or freshly prepared hydrogen peroxide (5 v/v %, 2 v/v %, 0.5 v/v %) was added to 1 mL stomatocyte nanomotors solution with the appropriate concentration (6×10^8 particles/mL) before loading into the sample cell. A typical video of 90 seconds was recorded. By analyzing the video, x, y coordinates of each particle were determined as a function of time intervals. Mean square displacements obtained by averaging over 25 particles from the major size distribution observed with Nanosight were plotted versus the time intervals.

Cell culture and cellular uptake evaluation by confocal microscopy and flow cytometry

HeLa cells were cultured in a T flask at 37 °C with Dulbecco's modified Eagle's medium (DMEM) buffer which was supplemented with 100 U/mL penicillin, streptomycin and 10% fetal bovine serum. When reaching 90% confluency, cells were harvested by trypsinization and centrifugation at 1000 rpm for 5 minutes and then resuspended in fresh culture medium (2×10^5 cells/mL) before being seeded into 8 well micro dish (ibidi GmbH) and incubated overnight. After removing the cell culture medium, the cells were rinsed with PBS for 3 times and incubated with 200 μL FITC PEG-PS stomatocytes or FITC-tat PEG-PS stomatocytes (particle concentrations were kept constant at 7×10^9 particles/mL, as determined with nanoparticle tracking analysis) with hydrogen peroxide free or hydrogen peroxide added (final hydrogen peroxide concentration is 0.015%) in DMEM buffer at 37 °C for 6 hours. After 6 hours, the culture medium was removed followed by two washing steps with PBS. Then the cells were stained with live cell nucleus dye Hoechst 33342 and cellmask deep red cell membrane dye before another washing step with PBS and addition of fresh DMEM buffer. The cellular uptake was examined with a confocal microscope (Leica TCS SP2 AOBS). FITC was excited with an Ar laser at 488 nm and the emission was collected at 510 – 530 nm. The laser beam was focused on the sample through a 63x oil immersion objective. A pinhole of 400 was selected. For cellular uptake analysis with flow cytometry, culture medium was removed from the well after 6 hours of incubation followed by one washing step with PBS. Then cells were detached by trypsinization (trypsin-EDTA) for 5 minutes. The cells were collected by centrifugation (1000 rpm, 5 min) and resuspended in PBS supplemented with 1% BSA before measurement with a flow cytometer (laser line 488 nm).

3.6. REFERENCES

[1] a) C. J. Kearney, D. J. Mooney, *Nat. Mater.*, 2013, **12**, 1004-1017; b) S. Krol, *J. Control Release*, 2012, **164**, 145-155; c) M. Mimee, R. J. Citorik, T. K. Lu, *Adv. Drug. Deliv. Rev.*, 2016, **105**, 44-54.

[2] a) S. Sanchez, L. Soler, J. Katuri, *Angew. Chem. Int. Ed.*, 2015, **54**, 1414-1444; b) M. Guix, C. C. Mayorga-Martinez, A. Merkoci, *Chem. Rev.*, 2014, **114**, 6285-6322; c) V. V. Singh, J. Wang, *Nanoscale*, 2015, **7**, 19377-19389; d) K. Kim, J. Guo, Z. X. Liang, F. Q. Zhu, D. L. Fan, *Nanoscale*, 2016, **8**, 10471-10490; e) H. Wang, M. Pumera, *Chem. Rev.*, 2015, **115**, 8704-8735; f) W. Wang, W. T. Duan, S. Ahmed, T. E. Mallouk, A. Sen, *Nano Today*, 2013, **8**, 531-554.

[3] a) W. Gao, J. Wang, *Nanoscale*, 2014, **6**, 10486-10494; b) Z. G. Wu, Y. J. Wu, W. P. He, X. K. Lin, J. M. Sun, Q. He, *Angew. Chem. Int. Ed.*, 2013, **52**, 7000-7003; c) F. Z. Mou, C. R. Chen, Q. Zhong, Y. X. Yin, H. R. Ma, J. G. Guan, *ACS Appl. Mater. Inter.*, 2014, **6**, 9897-9903.

[4] a) J. Orozco, V. Garcia-Gradilla, M. D'Agostino, W. Gao, A. Cortes, J. Wang, *ACS Nano*, 2013, **7**, 818-824; b) D. Kagan, P. Calvo-Marzal, S. Balasubramanian, S. Sattayasamitsathit, K. M. Manesh, G. U. Flechsig, J. Wang, *J. Am. Chem. Soc.*, 2009, **131**, 12082-12083; c) J. G. S. Moo, H. Wang, G. J. Zhao, M. Pumera, *Chem-Eur. J.*, 2014, **20**, 4292-4296; d) J. Wu, S. Balasubramanian, D. Kagan, K. M. Manesh, S. Campuzano, J. Wang, *Nat. Commun.*, 2010, **1**.

[5] a) W. Gao, X. M. Feng, A. Pei, Y. E. Gu, J. X. Li, J. Wang, *Nanoscale*, 2013, **5**, 4696-4700; b) L. Soler, S. Sanchez, *Nanoscale*, 2014, **6**, 7175-7182; c) W. Gao, J. Wang, *ACS Nano*, 2014, **8**, 3170-3180; d) M. L. Zhang, X. Xie, M. Tang, C. S. Criddle, Y. Cui, S. X. Wang, *Nat. Commun.*, 2013, **4**; e) L. Soler, V. Magdanz, V. M. Fomin, S. Sanchez, O. G. Schmidt, *ACS Nano*, 2013, **7**, 9611-9620.

[6] F. Peng, Y. F. Tu, J. C. M. van Hest, D. A. Wilson, *Angew. Chem. Int. Ed.*, 2015, **54**, 11662-11665.

[7] J. Wang, *Lab Chip*, 2012, **12**, 1944-1950.

[8] a) X. K. Lin, Z. G. Wu, Y. J. Wu, M. J. Xuan, Q. He, *Adv. Mater.*, 2016, **28**, 1060-1072; b) Z. G. Wu, X. K. Lin, Y. J. Wu, T. Y. Si, J. M. Sun, Q. He, *ACS Nano*, 2014, **8**, 6097-6105; c) Y. Ikezoe, G. Washino, T. Uemura, S. Kitagawa, H. Matsui, *Nat. Mater.*, 2012, **11**, 1081-1085.

[9] a) D. M. Copolovici, K. Langel, E. Eriste, U. Langel, *ACS Nano*, 2014, **8**, 1972-1994; b) Y. Jiang, M. Li, Z. Zhang, T. Gong, X. Sun, *Curr. Pharm. Biotechnol.*, 2014, **15**, 256-266; c) C. Bechara, S. Sagan, *FEBS Lett.*, 2013, **587**, 1693-1702.

[10] a) H. Brooks, B. Lebleu, E. Vives, *Adv. Drug. Deliver. Rev.*, 2005, **57**, 559-577; b) E. Vives, J. P. Richard, C. Rispal, B. Lebleu, *Curr. Protein Pept. Sc.*, 2003, **4**, 125-132; c) A. Mishra, G. H. Lai, N. W. Schmidt, V. Z. Sun, A. R. Rodriguez, R. Tong, L. Tang, J. Cheng, T. J. Deming, D. T. Kamei, G. C. Wong, *Proc. Natl. Acad. Sci. U S A*, 2011, **108**, 16883-16888; d) L. M. Pan, Q. J. He, J. N. Liu, Y. Chen, M. Ma, L. L. Zhang, J. L. Shi, *J. Am. Chem. Soc.*, 2012, **134**, 5722-5725.

[11] D. A. Wilson, R. J. M. Nolte, J. C. M. van Hest, *Nat Chem*, 2012, **4**, 268-274.

[12] D. A. Wilson, B. de Nijs, A. van Blaaderen, R. J. M. Nolte, J. C. M. van Hest, *Nanoscale*, 2013, **5**, 1315-1318.

4

Supramolecular adaptive nanomotors with magnetotaxis behavior

This chapter has been published:
F. Peng, Y. F. Tu, Y. J. Men, J. C. M. van Hest, D. A. Wilson, *Adv Mater*, 2016,
DOI: 10.1002/adma.201604996.

4.1 INTRODUCTION

Synthetic nano- and micro-motors have become a central research topic since the report of their first prototype, centimeter sized motor.[1] In mimicking natural molecular motors[2] or moving micro-organisms,[3] these motors convert locally supplied chemical energy into motion, showing prospects in revolutionizing various fields such as microsurgery,[4] targeted drug delivery,[5] sensing,[6] imaging[7] and environmental remediation[8]. However, motors in general and especially nanoscale motors, are susceptible to random fluctuations,[9] therefore navigation of autonomous motors remains challenging. Compared to natural motors, synthetic motors are insufficient to perform complex functions. To tackle this challenge, recent efforts have been dedicated to develop motors able to respond to environmental clues such as temperature,[10] external field[11] and light.[12] Only few recent reports[13] have shown that motors can navigate themselves according to local stimuli and stimulatory gradients. Among these, magnetic field and magnetic field gradients provide a wireless, non-invasive way to gain control over the motion of these motors. In nature, magnetotactic bacteria (*Magnetospirillum Magnetotacticum*) which possess iron oxide crystals in their body[14] can sense the external magnetic field and reorient themselves to the direction of Earth's magnetic field. Inspired by this, we set out to explore the possibility of gaining directional control by integrating magnetic segments into our supramolecular motors[5c] (Figure 4.1) and steer the motor using both a magnetic field gradient as well as by changing the direction of a homogeneous magnetic field. Due to their minimal invasive nature, external magnetic fields are compatible with most living systems and widely used for drug delivery[15] and imaging[16]. When compared with optical, electrical or acoustic fields, magnetic fields offer the highest flexibility concerning achievable forces.[17] Using magnetic fields to remotely manipulate nanomotors in a biological medium allows safe maneuvering.[18] However it remains a question whether dynamic motors could be precisely manipulated at nanometer scale and move within a micron sized confined space such as a tumor tissue-related environment.

Here we demonstrate the design of magnetically actuated stomatocyte nanomotors, which achieve guided autonomous motion. Going beyond the conventional top-down method to incorporate a magnetic component,[19] we adopted a bottom-up approach which is familiar to natural systems and introduced magnetic metallic nickel in situ with the catalytic platinum nanoparticles (PtNP). In this way the geometric asymmetry of the system was not compromised and the co-presence of both nickel and platinum in stomatocytes was ensured. The movement of our original supramolecular nanomotors was powered by catalytic decomposition of hydrogen peroxide, which is an interesting biologically relevant signaling compound related with tumor cell metastasis and invasion.[20] After incorporating the magnetic nickel component, the synthetic motor was able to function in dual mode (catalytically powered by PtNP or magnetically powered by magnetized nickel). Furthermore, this design also provided the possibility for simultaneous guiding and steering

of catalytically powered motors with additional magnetic fields. A human cervical cancer (HeLa) cell laden collagen gel matrix was used as a tumor tissue model to demonstrate the guided motion of nickel incorporated nanomotors. Being in the nanometer scale regime, the nanomotors were readily guided into the micrometer sized gel mesh. In addition, like other self-assembled motors,[21] the supramolecular motors can be easily fabricated and easily loaded with drugs and have good biocompatibility in a biological setting. Able to operate with multiple energy sources, nanomotors presented in this chapter promise to expand the applicability of the motors in biomedicine.

4.2. RESULTS AND DISCUSSION

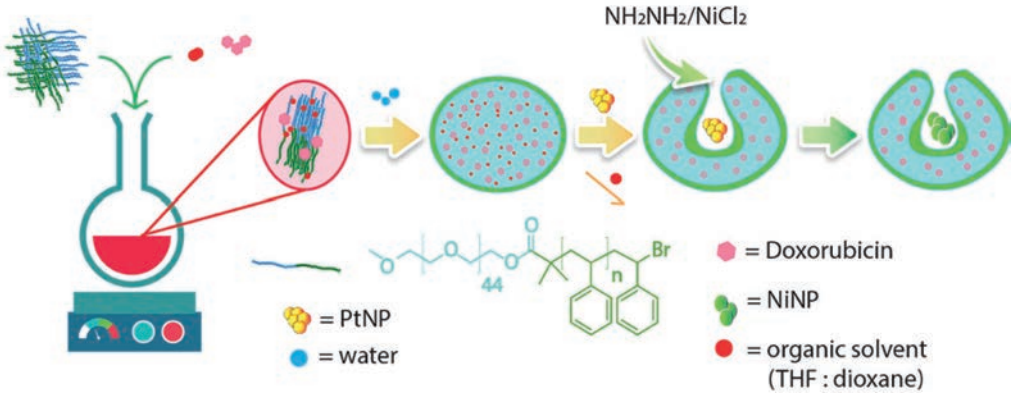

Figure 4.1. Preparation scheme of doxorubicin incorporated, platinum-nickel loaded stomatocytes.

Bowl shaped polymersomes or stomatocytes were assembled from diblock polymer poly(ethylene glycol)$_{44}$-*b*-polystyrene$_{190}$ via a controlled shape transformation.[22] The poly(ethylene glycol) segment allows the vesicles to be biologically stealthy and reduces the possibilities of immune attack and clearance. By adding preformed dendritic platinum nanoparticles into the polymer organic solution during self-assembly, nanoparticles were entrapped into the outer cavity of the stomatocytes (Figure 4.1). The loaded platinum nanoparticles serve as catalyst to decompose hydrogen peroxide into oxygen and are responsible for the propulsion of the entire system. Fluorescent anticancer drug doxorubicin (Dox), as a model drug, was mixed with the organic solvent containing the polymer, and was enclosed in the original lumen of the stomatocyte. After self-assembly and shape transformation into doxorubicin- and PtNP-loaded stomatocytes, metallic nickel was grown in situ directly onto the platinum nanoparticles which served both as catalyst and substrate.[23]

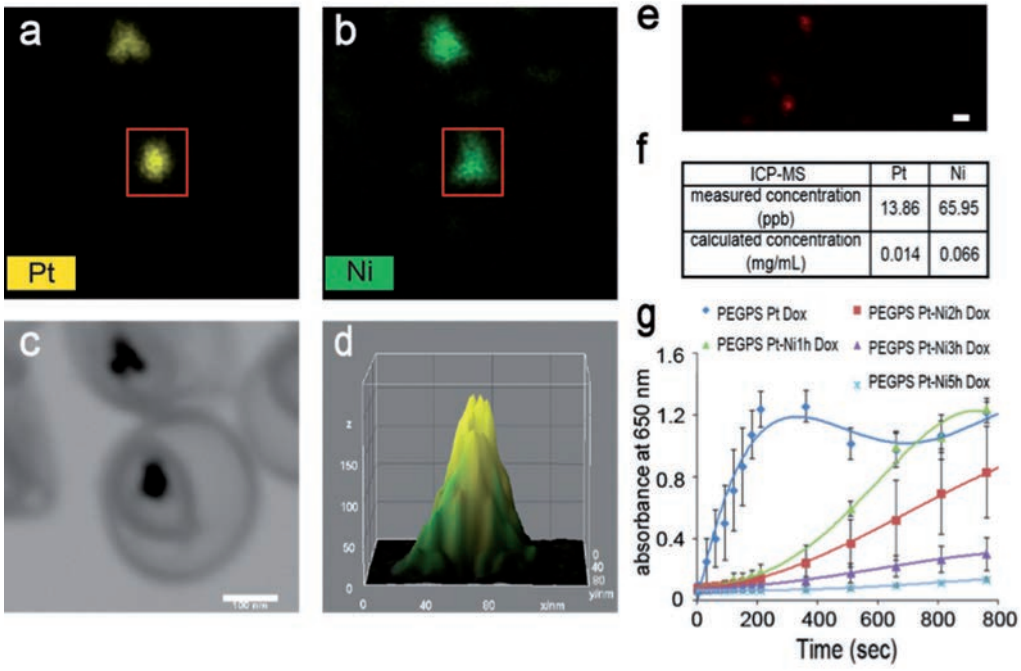

Figure 4.2. EDX mapping of a) platinum, yellow; b) nickel, green; c) corresponding STEM image of the assembled nanomotors, scale bar is 100 nm; d) 3D surface plot profile over the cross section of a doxorubicin platinum-nickel loaded stomatocyte, indicated by the red square in a) and b), giving intensity (z axis) with distance over the cross section (x, y axis); e) confocal fluorescence microscope image of doxorubicin platinum-nickel loaded stomatocytes, scale bar represents 1 µm; f) concentration of platinum and nickel by ICP-MS; g) comparison of reaction rate of platinum catalyzed tetramethylbenzidine-H_2O_2 reaction for doxorubicin platinum loaded stomatocytes (before nickel growth or nickel growth time 0 hours, blue) and doxorubicin platinum-nickel loaded stomatocytes with different nickel growth times of 1 hour (green), 2 hours (red), 3 hours (purple) and 5 hours (cyan).

Figure 4.1 summarizes the experimental procedure for preparing the platinum-nickel loaded stomatocytes. In the presence of reducing agent hydrazine, a nickel ion-hydrazine complex was first formed, followed by the reduction to metallic nickel by the platinum catalyst. No additives or stabilizers were needed. The reduction reaction was allowed to run at 40°C for 2 hours. After 2 hours, the reaction was stopped. Ultrafiltration was used to remove unreacted hydrazine and nickel ions before the Energy-dispersive X-ray spectroscopy (EDX) analysis. EDX was used to show the element distribution of the structure (platinum, yellow color and nickel, green color) (Figure 4.2a-c). ImageJ 3D surface plot plugin was used to analyze EDX mapping data, allowing the imaging of the elements distribution in all directions. At a rotation angle of 0°, it was shown that nickel (green color) covered the surface of this side (Figure 4.2d) and increased the surface thickness. When changing the

rotation angle to 120°, it could still be observed that nickel (green) was deposited on the surface (Figure 4.3a, pointed by the red arrow) while in certain areas platinum (yellow) was still present on the surface (Figure 4.3a, pointed by the blue arrow).

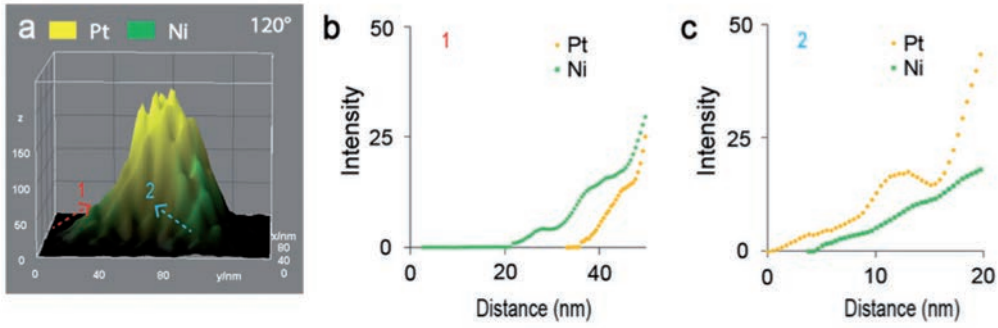

Figure 4.3. 3D surface plot profile of a cross section of platinum loaded stomatocytes after growing nickel for 2 hours, giving intensity (z axis) with distance of the cross section (x, y axis), platinum, yellow and nickel, green; a) at an angle of 120°, The cross section is indicated by the red square in Figure 4.2a, b. b) 2D plot profile of intensity versus distance of direction 1, pointed by red arrows; c) 2D plot profile of intensity versus distance of direction 2, pointed by blue arrows.

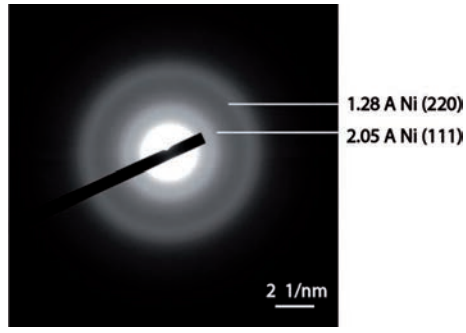

Figure 4.4. Selected area electron diffraction pattern of one platinum-nickel loaded stomatocyte. The obtained index of the rings and interplanar distance confirm the presence of nickel metal.

Inductively coupled plasma emission-mass spectrometry (ICP-MS) further confirmed the presence of nickel (Figure 4.2f). High magnification TEM in the selected area of one platinum-nickel loaded stomatocyte, showed the diffraction pattern typical for crystalline metallic nickel, demonstrating again the presence of nickel (Figure 4.4). As mild conditions were used for the reaction, the in situ growth of nickel did not induce a change of the stomatocyte morphology or encapsulation efficiency, as was observed from representative TEM images of only platinum loaded stomatocytes and platinum-nickel loaded stomatocytes (Figure 4.5).

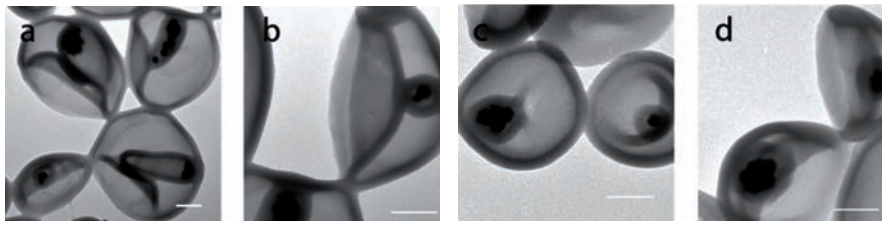

Figure 4.5. TEM images of (a, b) doxorubicin and platinum nanoparticles loaded stomatocytes; (c, d) doxorubicin and platinum-nickel loaded stomatocytes, scale bar represents 100 nm.

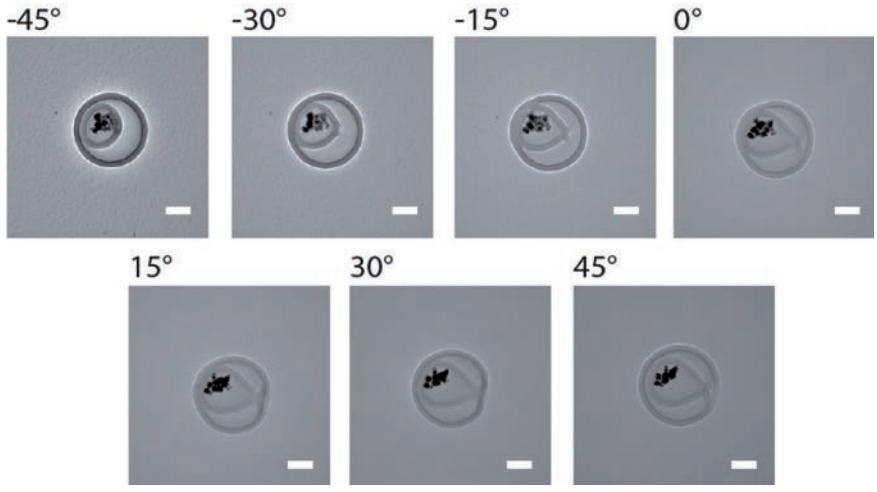

Figure 4.6. Cryo-TEM images at different rotation angles from -45° to 45 ° of doxorubicin and platinum-nickel nanoparticles loaded stomatocytes, scale bar represents 100 nm.

For platinum loaded stomatocytes, the positioning of the platinum nanoparticles in the cavity of stomatocytes has been demonstrated with TEM tomography in a previous report by our group.[24] In the case of doxorubicin platinum-nickel loaded stomatocytes, cryo-TEM at different rotation angles along the x-axis was performed, showing as expected, the entrapment of the particles inside the cavity of the stomatocytes (Figure 4.6). The fluorescence signal present inside the stomatocytes demonstrated the successful loading of the fluorescent antitumor model drug Dox (Figure 4.2e). The fluorescence of Dox facilitates the tracking of motion with confocal fluorescence microscopy. After growing nickel in situ, catalytic activity of platinum was examined to assess whether the hydrogen peroxide decomposing capability was maintained. Adding a solution of platinum-nickel loaded stomatocytes to concentrated hydrogen peroxide (0.5% v/v) led to bubble formation, indicating the preserved catalytic

activity. To quantitatively determine the catalytic activity, a 3,3',5,5'-tetramethylbenzidine-H_2O_2 assay was used.[25] 3,3',5,5'-tetramethylbenzidine (TMB) was oxidized by hydrogen peroxide in the presence of platinum nanoparticles to blue 3,3',5,5'-tetramethylbenzidine diimine and the reaction speed was quantitatively related with the catalytic activity of platinum. As demonstrated in Figure 4.2g, catalytic activities experienced a decrease after nickel growth for 2 hours, yet a clear residual activity was still present.

We speculate that the preservation of Pt catalytic activity is caused by a partial surface coverage of the platinum nanoparticles by the nickel layer and the high branching and porosity of the dendritic platinum nanoparticles. It was speculated that catalytic activity can be therefore preserved as long as the grown nickel does not form a complete shell over the particle which can block all the catalytic branches. To verify this, we followed the reduction process of the nickel precursor in time and explored different nickel growth times of 1 hour, 2 hours, 3 hours and 5 hours. A decrease in the catalytic activity was observed with increasing the reduction time/nickel growth time (Figure 4.2g). However the catalytic activity of platinum was preserved with nickel growth times shorter than 5 hours, indicating a partial coverage of the platinum surface. After growing nickel for 5 hours, platinum catalytic activity was finally hindered, indicating that 5 hours is the time point for complete coverage and formation of a closed nickel shell.

After confirming the structure of doxorubicin platinum-nickel loaded stomatocytes, we next tested the magnetic response of nickel containing stomatocytes. An NdFeB magnet (12 mm× 12 mm×12 mm) was used to generate a magnetic field gradient. With a hand held gauss meter, the decay of field strength with increasing distance from the magnetic pole was verified and measured (Figure 4.7a). The gradient field resulted in movement of the doxorubicin platinum-nickel loaded stomatocytes to the vicinity of the magnet, which was clearly visible as demonstrated by the inhomogeneous distribution of the particles in the bulk solution (Figure 4.7 b, c).

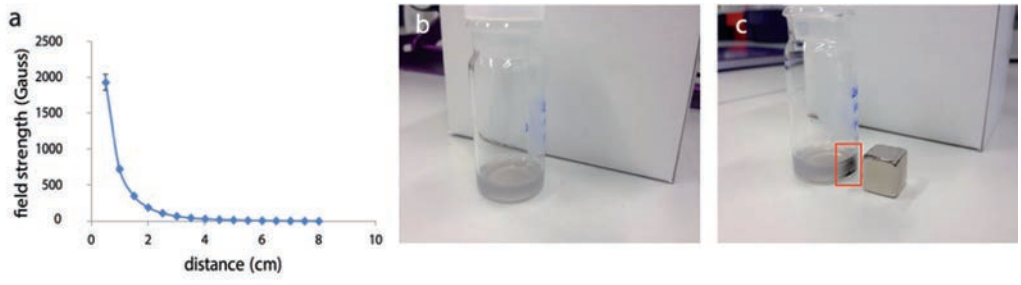

Figure 4.7. a) Plot of field strength with increasing distance away from the magnetic pole; Photographs of doxorubicin and platinum-nickel loaded stomatocytes b) in the absence of magnet and c) in the presence of magnet. The gradient magnetic field generated by the NdFeB magnet (12 mm× 12 mm× 12 mm) resulted in a movement of the doxorubicin platinum-nickel loaded stomatocytes to the vicinity of the magnet while the bulk solution became visibly inhomogeneous.

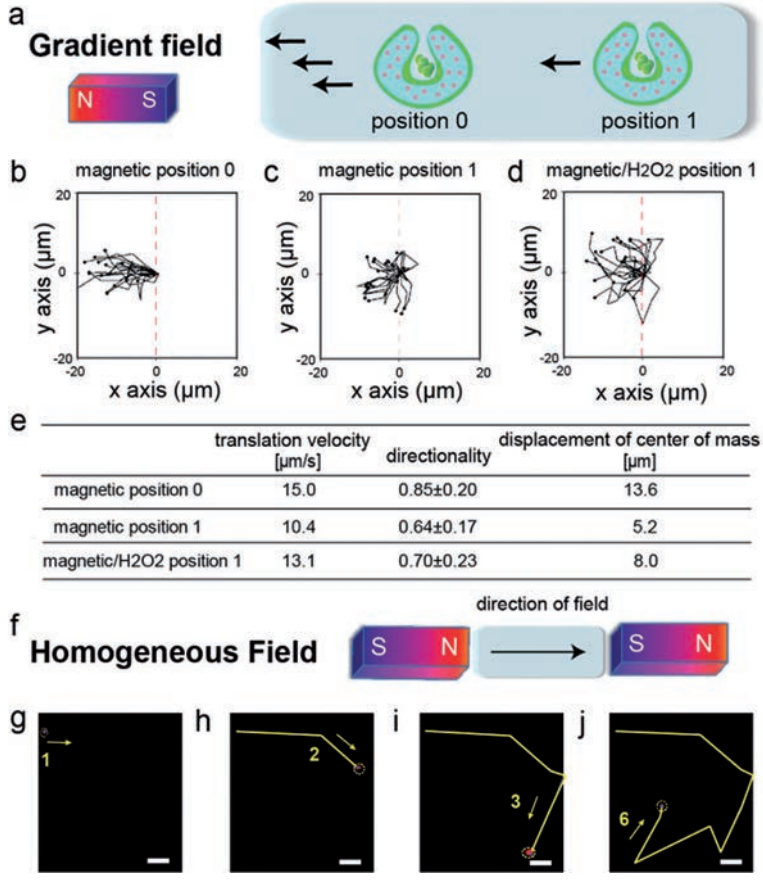

e

	translation velocity [μm/s]	directionality	displacement of center of mass [μm]
magnetic position 0	15.0	0.85±0.20	13.6
magnetic position 1	10.4	0.64±0.17	5.2
magnetic/H2O2 position 1	13.1	0.70±0.23	8.0

Figure 4.8. a) Schematic illustration of the doxorubicin platinum-nickel loaded stomatocytes movement to the left towards higher gradient magnetic field generated by an NdFeB magnet; Moving paths over 5 consecutive frames (time intervals= 268 ms) of the doxorubicin platinum-nickel loaded stomatocytes b) at position 0 (1 ± 0.1 cm away from the magnet) magnet-induced; c) at position 1 (3.5 ± 0.1 cm away from magnet) magnet-induced; d) at position 1, magnet/hydrogen peroxide induced. Starting points were normalized to the point of origin; e) summary table of translation velocity, directionality and displacement of center of mass for doxorubicin platinum-nickel loaded stomatocytes at position 0 with magnet in the left (25 stomatocytes analyzed), at position 1 with magnet in the left (26 stomatocytes analyzed) or at position 1 with both magnet and hydrogen peroxide (24 stomatocytes analyzed); f) Schematic illustration of the experimental set-up for homogeneous magnetic field generated by two parallel magnets; g-j) Confocal fluorescence images of the doxorubicin and platinum-nickel loaded stomatocyte movement in hydrogen peroxide solution (1.5% v/v) and their sequential steering by changing the direction of the field, time interval between video snapshots = 2304 ms, scale bar is 10 μm.

To remotely control the motion, magnetized nickel containing stomatocytes were exposed to the gradient magnetic field and visualized with confocal microscopy. When the magnet was placed to the left, collective motion of stomatocytes towards areas of higher field strength (left area) was observed (Figure 4.8a scheme). At a distance of 3.5 cm away (max distance used) from the magnet, the magnetic force of magnetized nickel was still sufficient to direct the motion of the stomatocytes. The field strength applied yielded approximately a magnetic torque of 6.0×10^{-19} J on the stomatocyte nanomotors. This was calculated from the formula $\tau = \mu \times B$ (where μ is the magnetic dipole moment $\mu = M \times m_{Ni} = 12$ emu/g $\times 1.1 \times 10^{-14}$ g; M, the saturation magnetization is the reference value[26] while m_{Ni} or mass of nickel assuming a thickness of nickel layer of 25 nm (from EDX data); B is the field strength 50 Gauss), exceeding the value of rotational thermal energy (2.06×10^{-21} J) by 2 orders of magnitude. The nickel-containing stomatocytes navigated towards the magnet at the left as indicated by the trajectory path (Figure 4.8b-d). Three parameters: average velocity, directionality and displacement of center of mass were used to quantitatively evaluate the directed motion. Directionality, averaged value of euclidian distance divided by accumulated distance, is a measure of the straightness of motion. The displacement of center of mass describes the average spatial distance between the starting and end point of the stomatocytes, which indicates the migration length. The applied magnetic field could provide a driving force as well as a guiding force to stomatocytes, as illustrated in Figure 4.8b-d, at both position 0 and position 1, respectively 1.0 ± 0.1 cm and 3.5 ± 0.1 cm away from the magnet. From Figure 4.7a, the exerted field strengths at the two distances were estimated to be 732 ± 28 Gauss and 50 ± 1 Gauss, respectively (hence a gradient of 1576 Gauss/cm and 67 Gauss/cm).

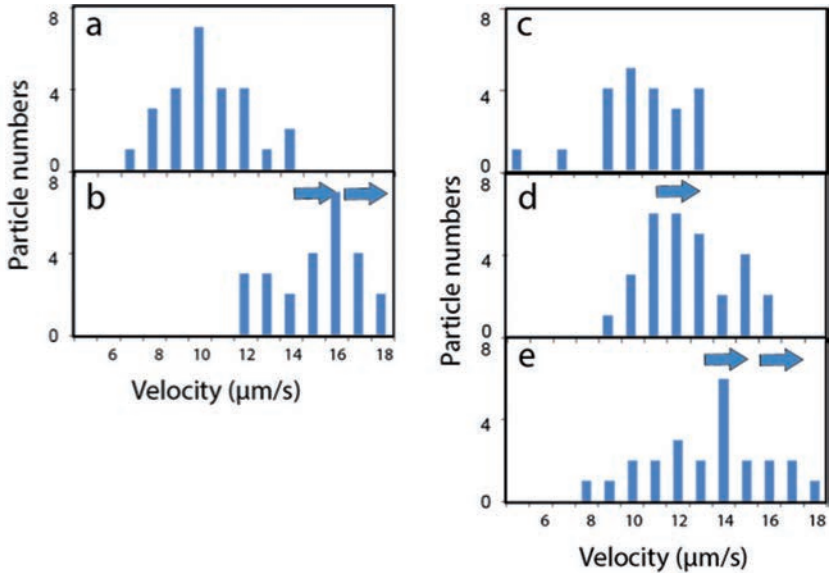

Figure 4.9. Velocity distribution of doxorubicin and platinum-nickel loaded stomatocytes motors a) with magnet at position 1; b) with magnet at position 0; c) with magnet and 0.025% hydrogen peroxide at position 1; d) with magnet and 0.25% hydrogen peroxide at position 1; e) with magnet and 1.5% hydrogen peroxide at position 1.

By moving towards the magnet, the stomatocyte motors experienced an increase in average velocity from 10.4 (position 1) to 15.0 μm/s (position 0) as well as a change in directionality from 0.64 to 0.85 (for velocity distribution of stomatocyte motors at both positions, see Figure 4.9a, b). The driving force increases with a decreased distance from the magnet. This is because gradient force increases as well as a higher torque induced by increasing field strength. When both a magnetic field and a hydrogen peroxide solution (1.5% v/v) were present (Figure 4.8d), at position 1 the translation velocity and displacement of center of mass experienced were increased to 13.1 μm/s and 8.0 μm (compared to 10.4 μm/s and 5.2 μm for the magnet-only system, Figure 4.8c). Therefore the combination of hydrogen peroxide fuel and magnetic attraction led to a directional motion towards the magnetic pole, yet at a higher velocity compared to applying the magnetic field alone. In the presence of the magnet and at position 1, the influence of different hydrogen peroxide concentrations over the movement was investigated. The stomatocyte motors moved faster with increasing levels of hydrogen peroxide (Figure 4.9c, d, e). Hydrogen peroxide is a bio-relevant chemical overproduced by human tumor cell lines[20] although there are also reports about its potential harm to cells including DNA lesions.[27] Here we used it as a proof of concept to use bio-relevant chemicals for propulsion. Attraction towards the magnet was not disturbed at all these hydrogen peroxide levels. In the absence of

both fuel and magnetic field, typical Brownian motion was observed (Figure 4.10a). The displacement of the center of mass was 2.0 µm. No favored moving direction was observed. The directionality was 0.45, significantly lower than in the presence of magnetic field/ hydrogen peroxide. The average mean square displacement (MSD) versus time interval curve (Figure 4.10b) showed a linear fit typical for Brownian motion, demonstrating that the stomatocytes move with random motion when without fuel and magnetic field.

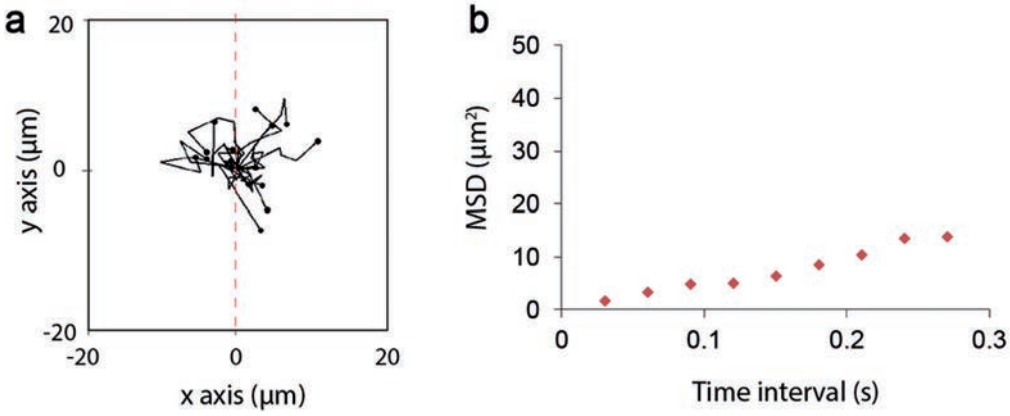

Figure 4.10. a) Tracking paths over 5 consecutive frames (time interval = 268 ms) of doxorubicin and platinum-nickel loaded stomatocytes without magnet/hydrogen peroxide (20 trajectories); b) average MSD versus time interval of the doxorubicin and platinum-nickel loaded stomatocytes motors in the absence of both hydrogen peroxide and magnetic field.

In addition to velocity as discussed above, moving direction can be governed by the profile of the applied field. Nickel-containing stomatocytes could readily sense the position change of the magnet and reorient their motion accordingly (Figure 4.11). The reorientation could be achieved repeatedly.

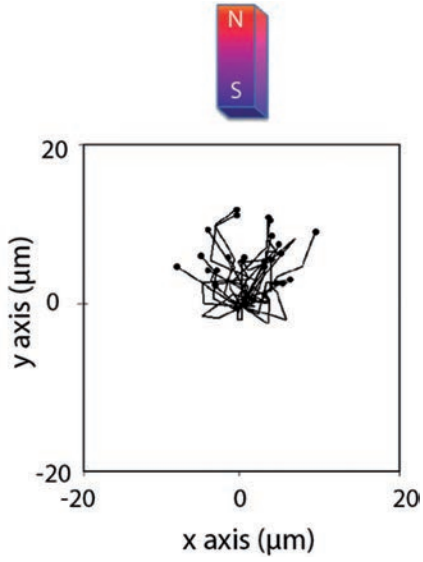

Figure 4.11. Tracking paths over 5 consecutive frames (time interval = 268 ms) of doxorubicin and platinum-nickel loaded stomatocytes after magnet position changed from left to top.

Besides the gradient field, we can also apply a homogeneous magnetic field by sandwiching the magnetized doxorubicin platinum-nickel loaded stomatocytes solution between two parallel magnets (NdFeB magnet, 12 mm× 12 mm×12 mm). By changing only the direction of the magnetic field (Figure 4.8g-j) not the positions of the magnets, we could precisely control the moving direction of the motors. After removing the external homogeneous field, dispersive movement with no favoured direction was observed. To test the transportation abilities of the stomatocyte motors in tissue, a tissue model was established by using microfluidic technology (illustrated in Figure 4.12). The micro slide consists of two chambers, which are connected through a narrow channel in the middle. In mimicking tissue,[28] firstly collagen (1 mg/mL) was used to form a gel network (mesh size approximately 10 μm, in agreement with previous report[29]) (Figure 4.12a, c, scanning electron microscope image and bright field image) in the left chamber and middle channel. After the gel formation, a diluted motor solution was added to the right channel. A low concentration of motors was used to avoid instant formation of bundles and hindered entrance into gel (2.8×10^9 particles/mL). The motors demonstrated Brownian motion.

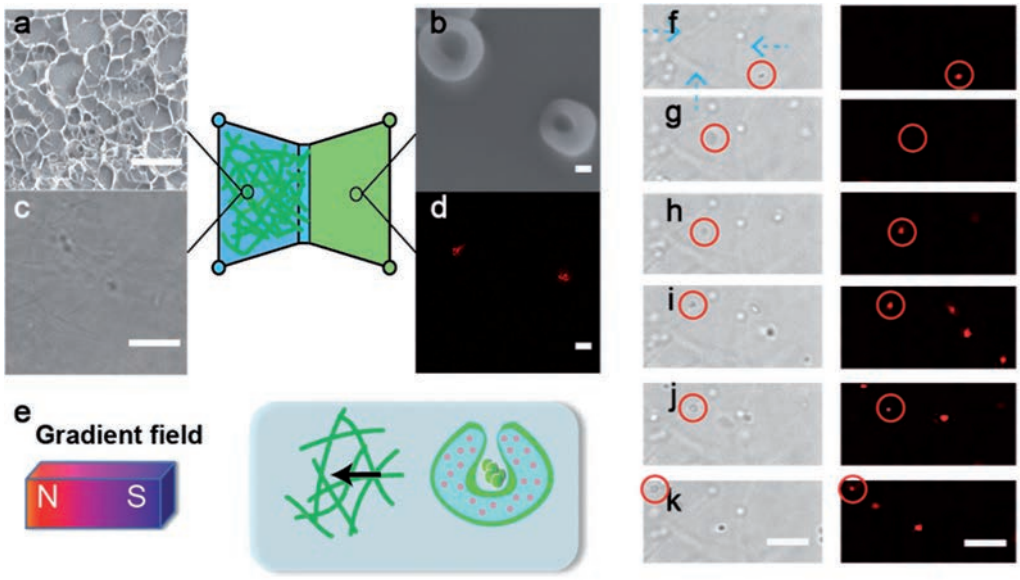

Figure 4.12. a) Cryo-SEM image of gel matrix, scale bar = 10 µm; b) SEM image of doxorubicin and platinum-nickel loaded stomatocytes, scale bar = 100 nm; c) confocal bright field image of gel matrix, scale bar = 10 µm; d) fluorescent image of doxorubicin and platinum-nickel loaded stomatocytes, scale bar represents 1 µm; e) scheme of the magnetic guidance of doxorubicin and platinum-nickel loaded stomatocytes towards the gel matrix; f-k) Doxorubicin platinum-nickel loaded stomatocytes could be guided through a collagen gel matrix by applying an external magnetic field (particle in red circle), video snapshots, time intervals 1.34 s, scale bar = 10 µm.

Then a magnet (NdFeB, 12 mm× 12 mm×12 mm) was placed on the left. Figure 4.12 f-k shows the gel boundary area. Stomatocyte motors could sense the magnetic field and be readily guided towards the gel mesh on the left. Upon entering the gel matrix (the blue arrows in Figure 4.12f point to the fibrils in a triangular gel mesh), the nanomotors demonstrated a guided motion through the gel mesh.

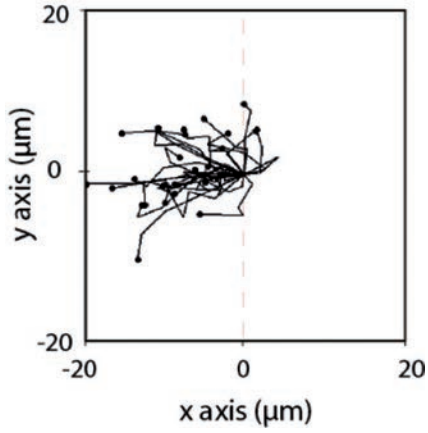

Figure 4.13. The tracking paths over 5 consecutive frames (time interval = 268 ms) of doxorubicin and platinum-nickel loaded stomatocytes through the gel mesh.

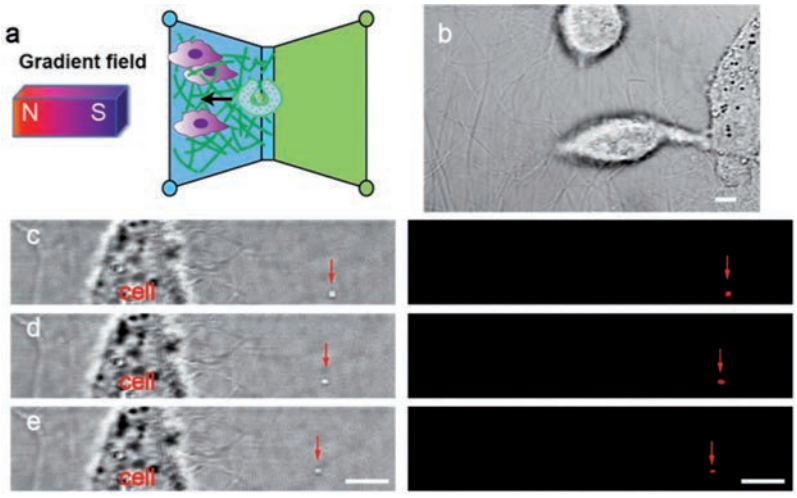

Figure 4.14. a) Schematic representation of the magnetic guidance of doxorubicin and platinum-nickel loaded stomatocytes through HeLa cell laden gel matrix; b) confocal bright field image of HeLa cell laden gel, scale bar represents 10 µm; c-e) Doxorubicin platinum-nickel loaded stomatocytes could be guided towards a cell in the collagen gel mesh by applying an external magnetic field (particle pointed by the red arrow), left: bright field, right: fluorescent field, tracking trajectories over 3 fames, time intervals 268 ms, scale bar = 10 µm.

The velocity of motors was 12.4 μm/s. The tracking path of motors was shown in Figure 4.13. Tuning the collagen concentration can vary the gel mesh density/crosslinking density of the collagen gel. By increasing the concentration to 1.5 mg/mL from 1 mg/mL, we obtained a gel with a decreased mesh size of 6 μm, which is in agreement with the literature data.[29] At this gel pore size, the movement of the stomatocytes remained unhindered in their guided motion towards the magnetic pole. After demonstrating the possibility of achieving guided motion in a pure gel, we replaced it with a gel loaded with human cervical cancer HeLa cells as a mimic of a tumour tissue. Figure 4.14a shows schematically the experimental design of magnetic guided motion of nickel containing stomatocytes towards the cell-laden gel. After placing the magnet to the left, doxorubicin and platinum-nickel loaded stomatocytes moved forward towards the magnet and travelled through the HeLa cell laden gel matrix. Collective motion towards left where the magnetic field strength was stronger was observed.

4.3. CONCLUSION

We fabricated magnetic nanomotors by using a convenient and mild bottom-up approach and presented a method to achieve directional control over nanometer scale stomatocyte motors. The nickel-platinum particles incorporated into the stomatocytes allowed both hydrogen peroxide/magnetic locomotion and remote magnetic guidance. Finally we have also shown that nanomotors can be guided through a tissue model formed from a collagen gel. Capable of steerable motion at a relatively high speed, the motors could transport drug molecules in a targeted specific way and hold promise for precise localized tissue drug delivery.

4.4. ACKNOWLEDGEMENTS

We want to thank the people from general instrument department, Geert-Jan Janssen, Liesbeth Pierson, Paul Van der Ven for their very kind help with the analysis in this chapter. Min Bao is acknowledged for the fruitful discussions about 3D cell culturing. We thank Roeland Nolte for his many valuable suggestions.

4.5. EXPERIMENTAL SECTION

Materials

Poly(vinyl pyrrolidone) (MW10000), potassium tetrachloroplatinate (II), L (+) ascorbic acid, hydrazine monohydrate, dimethylformamide, 3,3',5,5'-tetramethylbenzidine (TMB) and collagen solution from bovine skin were purchased from Sigma-Aldrich. Doxorubicin (Dox) was purchased from Bioconnect BV. Nickel chloride anhydrous was obtained from Alfa Aesar. Spectra/Por dialysis membrane with a MW cut-off of 12000-14000 Da was used for dialysis. All aqueous solutions were prepared with MilliQ water, purified with a MilliQ QPOD purification system (18.2 MΩ).

Instruments

^{1}H nuclear magnetic resonance spectra (^{1}H NMR) were performed on a Varian Inova 400 MHz spectrometer, with CDCl3 as solvent. Gel permeation chromatography (GPC) was obtained on a Shodex GPC column equipped with UV SPD 20A detectors (254 nm, 215 nm). THF was used as eluent and the flow rate was kept constant at 1 mL/min. Dynamic light scattering (DLS) analysis was performed on a Malvern Zetasizer Nano S with the following settings: temperature 25 °C, He-Ne laser wavelength 633 nm and detector angle 173°. Inductively Coupled Plasma - Mass Spectrometry (ICP-MS) measurement was carried out with a Thermo Fisher Scientific Xseries I quadrupole machine. For transmission electron microscopy (TEM), a JEOL 1010 Transmission Electron Microscope with MegaView Soft Imaging camera at an acceleration voltage of 60 kV was used. Energy-dispersive X-ray spectroscopy (EDX) and selected area electron diffraction (SAED) were performed on a JEOL TEM 2100 with high-quality Gatan 895 ultrascan 4000 bottom mount camera (4080x4080 pixels) incorporated. A Bruker Quantax EDS system with an STEM detector incorporated was used for element mapping (platinum and nickel). Scanning electron microscope (SEM) images were recorded on a JEOL 6330 field emission scanning electron microscope. Magnetic field strength was measured with a hand held Gaussmeter HGM09s (MAGSYS magnet system GmbH).

Synthesis of poly(ethylene glycol)$_{44}$-*b*-polystyrene$_{190}$ (PEG$_{44}$-*b*-PS$_{190}$)

The block copolymer poly(ethylene glycol)$_{44}$-*b*-polystyrene$_{190}$ was synthesized via the atom transfer radical polymerization method. The polymerization process was monitored by determining the molecular weight of the block copolymer with ^{1}H NMR and GPC. The reaction was terminated once the desired MW of 21 kg/mol was attained.

Preparation of platinum nanoparticles (PtNP) with PVP coating

To 2 mL K_2PtCl_4 (20 mM), 20 mg poly(vinyl pyrrolidone) (PVP, MW≈ 10,000) was added. The solution was left to stir at room temperature. After 48 hours, 1 mL ascorbic acid (0.2 M) was

added to the above solution. Then the mixture was incubated in a sonication bath (VWR Ultrasonic Cleaner Model 75D) at room temperature for 1 h. Average size of particles was determined to be 70 nm with DLS.

Preparation of the Dox and platinum nanoparticles (PtNP)-loaded stomatocytes

Poly(ethylene glycol)$_{44}$-*b*-polystyrene$_{190}$ (10 mg) was allowed to dissolve in 1 mL organic solvent mixture (tetrahydrofuran:dioxane = 4:1) for 30 min. Then 0.05 mg doxorubicin solution in DMF was added. After stirring for 5 minutes, MilliQ water (0.35 mL) was delivered to the solution with a syringe pump (1 mL/h), followed by addition of 0.65 mL PtNP aqueous solution. After delivery, the mixture was sealed in a dialysis bag and dialyzed for 48 hours. With dynamic light scattering (DLS), the diameter of the obtained structures was determined to be 308 nm.

Preparation of the Dox and platinum-nickel loaded stomatocytes

The above obtained Dox and PtNP loaded stomatocytes solution (500 µL) was ultra-filtered (Ultrafree-MC VV Centrifugal filter, pore size 0.1 µm, EMD Millipore) for 5 times to remove free PtNP and resuspended with MilliQ to 500 µL. To the solution, an aqueous nickel chloride solution (1.7×10^{-2} M, 1 mL) was added. The mixture was left to stir for 20 minutes before addition of hydrazine (17 µL). Then the mixture was stirred vigorously for 2 hours. After reaction ultrafiltration was used to remove unreacted nickel ions, salts and hydrazine.

Inductively Coupled Plasma-Mass Spectrometry (ICP-MS) measurement

The purified Dox and platinum-nickel loaded stomatocytes solution (10 µL) was destructed in 65% nitric acid (1.5 mL) at 80 °C for 3 hours. Then the volume was adjusted to 10 mL with MilliQ before measurement with Thermo Fisher Scientific Xseries I quadrupole machine.

Transmission electron microscopy (TEM)

6 µL of diluted sample aliquots were casted onto carbon-coated copper grids. The grids were allowed to dry overnight at room temperature. Image acquisition was performed with iTEM software (Olympus).

Determination of platinum catalytic activities

To prepare 3,3',5,5'-tetramethylbenzidine (TMB) assay solution, TMB in DMF solution (250 µL) was mixed with 300 µL hydrogen peroxide solution (30%, v/v). To the above mixture 4450 µL sodium citrate-citric acid buffer (pH = 4) was added. The catalytic reaction was carried out at 25 °C with 2 µL Dox and platinum-nickel loaded stomatocytes/Dox or platinum loaded stomatocytes (particle number maintained the same 3×10^{11} particles/mL) in 238 µL of TMB assay solution. For particle number measurement, NanoSight NS 500 (Malvern instrument) was used. A sample solution was pumped into the sample chamber. Then five

videos were recorded (rate 30 frames/s, each video duration time 60 s) and processed with Nanoparticle Tracking Analysis software. Particle concentration was obtained by determining the average particle number in one frame. Reaction kinetics were monitored by recording absorption at 650 nm with a microplate reader (TECAN, Infinite 200).

Scanning electron microscopy (SEM) sample preparation

For SEM visualization of the gel matrix structure, a JEOL 6330 field emission scanning electron microscope was used. 200 µL collagen gel matrix was rapidly frozen in liquid nitrogen and freeze fractured in the cooling prechamber of the microscope. After etching for 5 min, the sample was subjected to palladium-gold sputtering before transferring to the SEM microscope chamber maintained at -120 °C. For Dox and platinum-nickel loaded stomatocytes, 6 µL of diluted aliquots were casted onto carbon-coated copper grids. The grids were allowed to dry overnight at room temperature and then sputtered with palladium-gold (Cressington 208HR sputter coater) before analysis with the microscope.

Magnetic guided motion in solution

A confocal fluorescence laser scanning microscope (Leica TCS SP2 AOBS) was used to record the motion. The laser beam (488 nm argon laser) was focused on the sample through a 63x oil immersion objective. A pinhole of 400 µm was selected. Emission of particles was detected using a band pass 530-620 nm. To visualize particle motion, time lapse series were recorded (100 frames, time interval between each frames ΔT = 268 ms). Bidirectional scanning mode was used and the scanning speed was set at 1000 Hz to ensure a minimal time interval of 268 ms. Tracking image sequences were analyzed with ImageJ plugin manual tracking. With the x/y coordinates information, the distance a particle travelled within the 268 ms time interval was determined. By averaging the velocity of a particle over different time intervals, the average velocity of the particle was obtained. For each group 25 nanoparticles were tracked and the velocity determined, giving a final average velocity. The propulsion was performed with µ-Slide 8 Well (ibidi). For magnetization, 200 µL Dox and platinum-nickel loaded stomatocytes aqueous suspensions were magnetized by collecting them at the side of an eppendorf tube (1 mL) with a magnet for 1 min and redisperse them before being transferred to the well of µ-Slide. When an external magnetic field was applied, the stomatocyte nanomotors in solution gradually assembled to form chain-like structures (after 15 minutes). The as-formed chain-like bundles could be aligned in the direction of the field. Such self-assembly behaviour was not observed for platinum-only loaded stomatocytes. For dual mode propulsions, the well was filled with 200 µL magnetized Dox and platinum-nickel loaded stomatocytes hydrogen peroxide solution. For magnetic steering, by changing the field direction of the homogeneous field, magnetized Dox and platinum-nickel loaded stomatocyte suspensions were placed in a µ-Slide well between two parallel magnets (NdFeB magnet, 12 mm× 12 mm×12 mm), which generate constant field strength of 210 Gauss in the well for measurement and observation.

Cell culture

HeLa cells were cultured in a T flask at 37°C with Dulbecco's modified Eagle's medium (DMEM) buffer, which was supplemented with 100 U/mL penicillin, streptomycin and 10% fetal bovine serum. When reaching 90% confluency, cells were harvested by trypsinization and centrifugation at 1000 rpm for 5 minutes and then re-suspended in fresh culture medium (2×10^5 cells/mL) before use.

Magnetic guided motion in gel

For fabricating a gel matrix with mesh size of approximately 10 µm, the pH of 300 µL collagen solution (3 mg/mL) was adjusted to neutral with 21 µL of sodium bicarbonate (7.5%) in an ice bath and diluted to a final volume of 900 µL (collagen concentration 1 mg/mL). To obtain a gel with a mesh size of 6 µm, 150 µL collagen solution (3 mg/mL) was mixed with 10 µL of sodium bicarbonate (7.5%), followed by dilution to 300 µL (collagen concentration 1.5 mg/mL) with (DMEM) buffer. For HeLa cell laden gel matrix with 10 µm mesh size, 300 µL collagen solution (3 mg/mL) was mixed with 21 µL of sodium bicarbonate (7.5%) and diluted with cells suspension to 900 µL. A well-mixed pH-adjusted collagen suspension (without/with cells) was obtained after pipetting up and down for several times. Then the suspension (65 µL) was added to the left reservoir of a µ-Slide Chemotaxis (ibidi) and incubated at 37°C overnight. For magnetic guidance towards the gel matrix, 65 µL of Dox and platinum-nickel loaded stomatocytes (2.8×10^9 particles/mL) solution was added to the right reservoir of the µ-Slide Chemotaxis.

4.6. References

[1] R. F. Ismagilov, A. Schwartz, N. Bowden, G. M. Whitesides, *Angew. Chem. Int. Edit.* **2002**, *41*, 652-654.

[2] a) M. Schliwa, G. Woehlke, *Nature* **2003**, *422*, 759-765; b) R. L. Cross, *Nature* **2004**, *427*, 407-408.

[3] A. Bahat, I. Tur-Kaspa, A. Gakamsky, L. C. Giojalas, H. Breitbart, M. Eisenbach, *Nat. Med.* **2003**, *9*, 149-150.

[4] a) A. A. Solovev, W. Xi, D. H. Gracias, S. M. Harazim, C. Deneke, S. Sanchez, O. G. Schmidt, *ACS Nano* **2012**, *6*, 1751-1756; b) D. Kagan, M. J. Benchimol, J. C. Claussen, E. Chuluun-Erdene, S. Esener, J. Wang, *Angew. Chem. Int. Edit.* **2012**, *51*, 7519-7522.

[5] a) D. Kagan, R. Laocharoensuk, M. Zimmerman, C. Clawson, S. Balasubramanian, D. Kang, D. Bishop, S. Sattayasamitsathit, L. Zhang, J. Wang, *Small* **2010**, *6*, 2741-2747; b) W. Gao, J. Wang, *Nanoscale* **2014**, *6*, 10486-10494; c) F. Peng, Y. Tu, J. C. van Hest, D. A. Wilson, *Angew. Chem. Int. Ed.* **2015**, *54*, 11662-11665; d) S. Tottori, L. Zhang, F. Qiu, K. K. Krawczyk, A. Franco-Obregon, B. J. Nelson, *Adv. Mater.* **2012**, *24*, 811-816; e) K. Kim, X. B. Xu, J. H. Guo, D. L. Fan, *Nat. Commun.* **2014**, *5*; f) X. Xu, K. Kim, D. Fan, *Angew. Chem. Int. Ed.* **2015**, *54*, 2525-2529.

[6] a) L. K. E. A. Abdelmohsen, F. Peng, Y. F. Tu, D. A. Wilson, *J. Mater. Chem. B* **2014**, *2*, 2395-2408; b) B. Jurado-Sanchez, A. Escarpa, J. Wang, *Chem Commun.* **2015**, *51*, 14088-14091; c) B. Esteban-Fernandez de Avila, A. Martin, F. Soto, M. A. Lopez-Ramirez, S. Campuzano, G. M. Vasquez-Machado, W. Gao, L. Zhang, J. Wang, *ACS Nano* **2015**, *9*, 6756-6764.

[7] E. S. Olson, J. Orozco, Z. Wu, C. D. Malone, B. Yi, W. Gao, M. Eghtedari, J. Wang, R. F. Mattrey, *Biomaterials* **2013**, *34*, 8918-8924.

[8] a) L. Soler, S. Sanchez, *Nanoscale* **2014**, *6*, 7175-7182; b) W. Gao, X. M. Feng, A. Pei, Y. E. Gu, J. X. Li, J. Wang, *Nanoscale* **2013**, *5*, 4696-4700.

[9] a) J. R. Howse, R. A. L. Jones, A. J. Ryan, T. Gough, R. Vafabakhsh, R. Golestanian, *Phys. Rev. Lett.* **2007**, *99*; b) T. C. Lee, M. Alarcon-Correa, C. Miksch, K. Hahn, J. G. Gibbs, P. Fischer, *Nano Lett.* **2014**, *14*, 2407-2412; c) P. H. Colberg, S. Y. Reigh, B. Robertson, R. Kapral, *Acc. Chem. Res.* **2014**, *47*, 3504-3511.

[10] S. Sanchez, A. N. Ananth, V. M. Fomin, M. Viehrig, O. G. Schmidt, *J. Am. Chem. Soc.* **2011**, *133*, 14860-14863.

[11] a) T. R. Kline, W. F. Paxton, T. E. Mallouk, A. Sen, *Angew. Chem. Int. Edit.* **2005**, *44*, 744-746; b) V. Magdanz, S. Sanchez, O. G. Schmidt, *Adv. Mater.* **2013**, *25*, 6581-6588; c) S. Sanchez, L. Soler, J. Katuri, *Angew. Chem. Int. Edit.* **2015**, *54*, 1414-1444.

[12] A. A. Solovev, E. J. Smith, C. C. B. Bufon, S. Sanchez, O. G. Schmidt, *Angew. Chem. Int. Edit.* **2011**, *50*, 10875-10878.

[13] a) S. Sengupta, K. K. Dey, H. S. Muddana, T. Tabouillot, M. E. Ibele, P. J. Butler, A. Sen, *J. Am. Chem. Soc.* **2013**, *135*, 1406-1414; b) B. ten Hagen, F. Kummel, R. Wittkowski, D. Takagi, H. Lowen, C. Bechinger, *Nat. Commun.* **2014**, *5*; c) G. J. Zhao, M. Pumera, *Langmuir* **2013**, *29*, 7411-7415; d) L. Baraban, S. M. Harazim, S. Sanchez, O. G. Schmidt, *Angew. Chem. Int. Edit.* **2013**, *52*, 5552-5556.

[14] a) F. Popp, J. P. Armitage, D. Schuler, *Nat. Commun.* **2014**, *5*; b) A. P. Chen, V. M. Berounsky, M. K. Chan, M. G. Blackford, C. Cady, B. M. Moskowitz, P. Kraal, E. A. Lima, R. E. Kopp, G. R. Lumpkin, B. P. Weiss, P. Hesse, N. G. F. Vella, *Nat. Commun.* **2014**, *5*; c) S. Martel, M. Mohammadi, O. Felfoul, Z. Lu, P. Pouponneau, *Int. J. Robot. Res.* **2009**, *28*, 571-582.

[15] a) Z. Luo, K. Y. Cai, Y. Hu, J. H. Li, X. W. Ding, B. L. Zhang, D. W. Xu, W. H. Yang, P. Liu, *Adv. Mater.* **2012**, *24*, 431-435; b) P. Saint-Cricq, S. Deshayes, J. I. Zink, A. M. Kasko, *Nanoscale* **2015**, *7*, 13168-13172.

[16] J. M. Shin, R. M. Anisur, M. K. Ko, G. H. Im, J. H. Lee, I. S. Lee, *Angew. Chem. Int. Edit.* **2009**, *48*, 321-324.

[17] a) A. Celedon, I. M. Nodelman, B. Wildt, R. Dewan, P. Searson, D. Wirtz, G. D. Bowman, S. X. Sun, *Nano Lett.* **2009**, *9*, 1720-1725; b) R. M. Erb, N. J. Jenness, R. L. Clark, B. B. Yellen, *Adv. Mater.* **2009**, *21*, 4825-4829; c) R. S. M. Rikken, R. J. M. Nolte, J. C. Maan, J. C. M. van Hest, D. A. Wilson, P. C. M. Christianen, *Soft Matt.* **2014**, *10*, 1295-1308; d) A. La Porta, M. D. Wang, *Phys. Rev. Lett.* **2004**, *92*; e) S. Gangwal, O. J. Cayre, M. Z. Bazant, O. D. Velev, *Phys. Rev. Lett.* **2008**, *100*.

[18] a) L. Baraban, D. Makarov, R. Streubel, I. Monch, D. Grimm, S. Sanchez, O. G. Schmidt, *ACS Nano.* **2012**, *6*, 3383-3389; b) D. Schamel, A. G. Mark, J. G. Gibbs, C. Miksch, K. I. Morozov, A. M. Leshansky, P. Fischer, *ACS Nano.* **2014**, *8*, 8794-8801.

[19] P. Mandal, V. Chopra, A. Ghosh, *ACS Nano.* **2015**, *9*, 4717-4725.

[20] T. P. Szatrowski, C. F. Nathan, *Cancer Res.* **1991**, *51*, 794-798.

[21] a) Z. Wu, Y. Wu, W. He, X. Lin, J. Sun, Q. He, *Angew. Chem. Int. Edit.* **2013**, *52*, 7000-7003; b) Y. Wu, Z. Wu, X. Lin, Q. He, J. Li, *ACS Nano.* **2012**, *6*, 10910-10916; c) X. Lin, Z. Wu, Y. Wu, M. Xuan, Q. He, *Adv. Mater.* **2016**, *28*, 1060-1072; d) Z. Wu, T. Si, W. Gao, X. Lin, J. Wang, Q. He, *Small* **2016**, *12*, 577-582.

[22] a) D. A. Wilson, R. J. M. Nolte, J. C. M. van Hest, *Nat. Chem.* **2012**, *4*, 268-274; b) D. A. Wilson, R. J. M. Nolte, J. C. M. van Hest, *J. Am. Chem. Soc.* **2012**, *134*, 9894-9897.

[23] a) M. Sanles-Sobrido, M. Perez-Lorenzo, B. Rodriguez-Gonzalez, V. Salgueirino, M. A. Correa-Duarte, *Angew. Chem. Int. Edit.* **2012**, *51*, 3877-3882; b) M. Grzelczak, M. A. Correa-Duarte, V. Salgueirino-Maceira, B. Rodriguez-Gonzalez, J. Rivas, L. M. Liz-Marzan, *Angew. Chem. Int. Edit.* **2007**, *46*, 7026-7030.

[24] D. A. Wilson, B. de Nijs, A. van Blaaderen, R. J. M. Nolte, J. C. M. van Hest, *Nanoscale* **2013**, *5*, 1315-1318.

[25] a) X. L. Sun, S. J. Guo, C. S. Chung, W. L. Zhu, S. H. Sun, *Adv. Mater.* **2013**, *25*, 132-136; b) G. W. Wu, S. B. He, H. P. Peng, H. H. Deng, A. L. Liu, X. H. Lin, X. H. Xia, W. Chen, *Anal. Chem.* **2014**, *86*, 10955-10960.

[26] M. Sanles-Sobrido, M. Banobre-Lopez, V. Salgueirino, M. A. Correa-Duarte, B. Rodriguez-Gonzalez, J. Rivas, L. M. Liz-Marzan, *J. Mater. Chem.* **2010**, *20*, 7360-7365.

[27] J. Nakamura, E. R. Purvis and J. A. Swenberg, *Nucleic Acids Res.*, 2003, **31**, 1790-1795.

[28] a) M. D. Tang, A. P. Golden, J. Tien, *Adv. Mater.* **2004**, *16*, 1345-1348; b) N. Sasaki, C. Bos, J. M. Escoffre, G. Storm, C. Moonen, *Int. J. Pharm.* **2015**, *482*, 118-122.

[29] P. Banerjee, D. Lenz, J. P. Robinson, J. L. Rickus, A. K. Bhunia, *Lab Invest.* **2008**, *88*, 196-206.

5

Continuous fabrication of polymeric vesicles and nanotubes with fluidic channels

This chapter has been published:
F. Peng, N.N. Deng, Y. F. Tu, J. C. M. van Hest, D. A. Wilson, *Nanoscale*, 2017, DOI: 10.1039/C7NR00142H.

5.1. INTRODUCTION

Polymersomes are bilayer structures self-assembled from amphiphilic polymers.[1] Both the lumen and the polymersome membrane provide high loading efficiencies of hydrophilic and hydrophobic cargos, respectively. Being more robust and tunable[2] than their lipid-based counterparts, polymersomes have attracted increasing attention with regard to applications in pharmaceutics,[1b] cosmetics,[3] imaging[4] and catalysis.[5] To fabricate these polymersomes, cosolvent methods[6] and rehydration methods[7] have been applied traditionally. These methods have the limitation that it is difficult to vary size and they usually yield polymersomes with broad size distribution. Post-processing steps, such as membrane extrusion[8] and sonication[9] are therefore required to reduce the polydispersity of the polymersomes produced. However, these post-treatment steps could lead to undesired material membrane interactions and loss of encapsulated cargo.

In order to directly create polymersomes with well-defined sizes, microfluidic techniques have been developed. Weitz's group fabricated monodisperse polymersomes through droplet formation using two immiscible liquids.[10] The formed W/O/W double emulsions act as templates to form vesicles after removing residual organic solvent.[11] Monodisperse micrometer sized vesicles were fabricated in this way.[12] To generate vesicles in the nanometer size range, laminar mixing of two miscible liquids in a fluidic channel has been shown to be a promising approach.[13] Well-defined nanometer sized vesicles, especially those in the range of 50 nm - 200 nm, are important in drug delivery by ensuring a long circulation time in vivo and an optimal cellular uptake without interference of the cell metabolism.[14]

Besides size, shape is another important feature that can affect polymersome properties. Although a few batch processes are described to create vesicles with non-spherical morphologies,[15] to the best of our knowledge no continuous flow procedures have been reported on the shape control of polymersomes. In this chapter we report the use of a flow device to fabricate nanometer-sized vesicles and nanotubes through laminar mixing of a polymer organic solution and water,[16] ensuring high production rate as well as high reproducibility. In addition, the ease of combining this vesicle production method with cargo loading makes this a versatile method for the preparation of polymeric assemblies for various applications.

5.2. RESULTS AND DISCUSSION

For the preparation of the polymeric vesicles, the amphiphilic block copolymer poly(ethylene glycol)$_{44}$-*b*-polystyrene$_{190}$ was used, which was synthesized via atom-transfer radical polymerization (see experimental section, Figure 5.1).[17] A flow device was used as depicted in Figure 5.2.

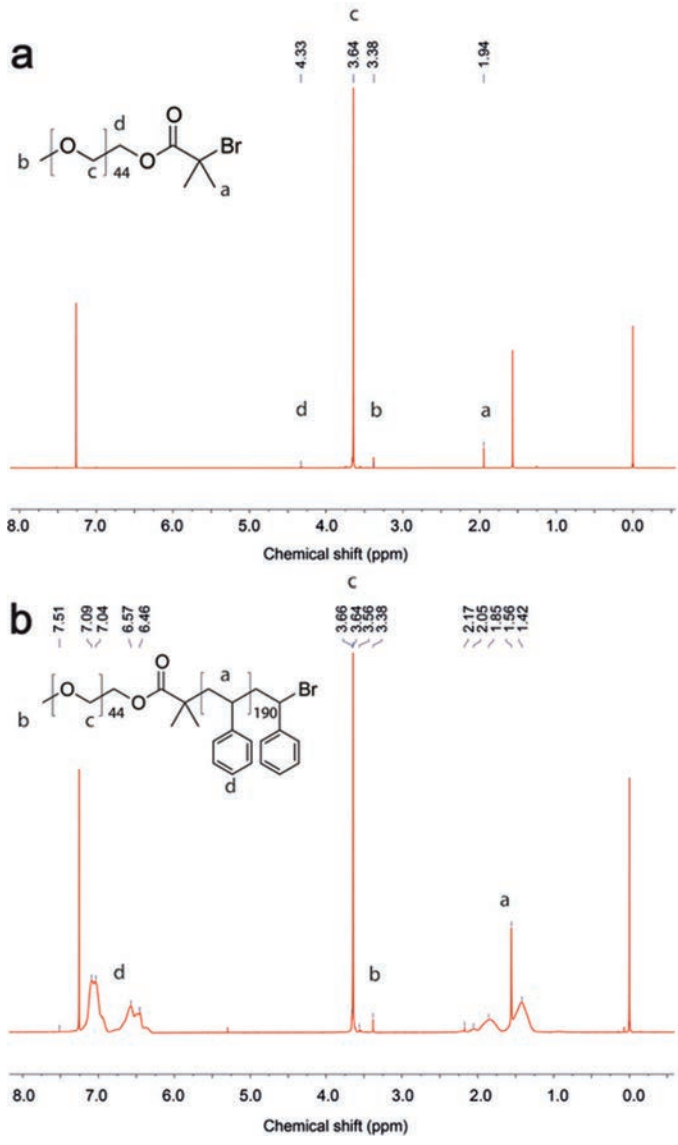

Figure 5.1. ^{1}H NMR spectrum in $CDCl_3$ at room temperature of a) PEG initiator δ: 1.94 ppm (s, 6H, $(CH_3)_2CBr$), 3.38 ppm (s, 3H, CH_3OCH_2), 3.64 ppm (br. s, PEG backbone), 4.33 ppm (t, 2H, $CH_2CH_2OC(O)C(CH_3)_2Br$); b) poly(ethylene glycol)$_{44}$-*b*-polystyrene$_{190}$ 1.42-2.17 ppm (br. m, PS backbone), 3.38 ppm (s, 3H), 3.56 – 3.66 ppm (br. s, PEG backbone), 6.46 – 7.51 ppm (br. m, aromatic ring of PS).

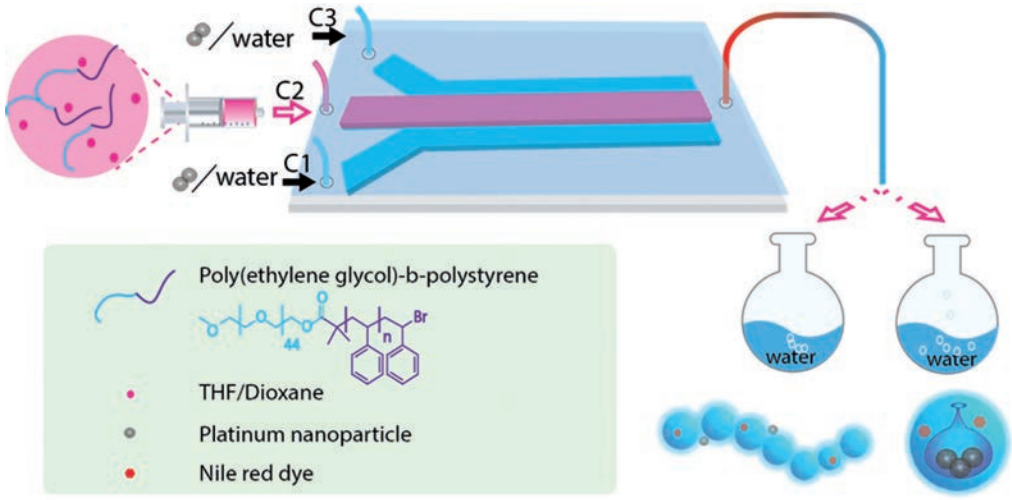

Figure 5.2. The fluidic platform for preparation of polymeric vesicles and nanotubes by varying the mode of collection and initial polymer concentration. The polymer dissolved in THF/dioxane was injected into the main channel (C2) and brought in contact with water in the two side channels (C1, C3) of the fluidic device.

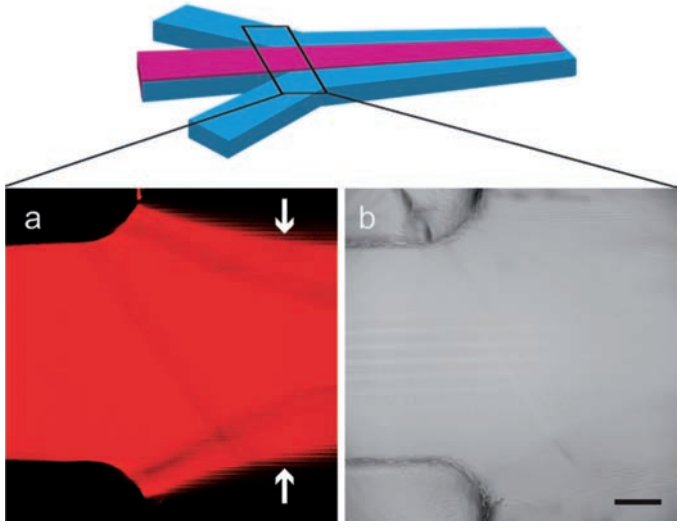

Figure 5.3. a) confocal microscopy image; b) corresponding bright field image of the section where the flows from 3 inlets meet, the white arrows point to the phase boundary. The scale bar represents 200 µm. Polymer/Nile red organic solution was injected through the middle inlet while aqueous solution was pumped in through 2 side inlets. Polymeric structures were formed at the periphery of the two phases.

An aqueous solution was injected through two side channels while the diblock copolymer in an organic solvent (THF/dioxane) solution was introduced in the middle channel (Figure 5.3). This device is a flow-focusing channel with the continuous phase flanking the dispersed one. Flow focusing has been used for the generation of spherical vesicles.[18] For the middle phase, both boundaries at the two sides are available for mixing. As both organic solvents are miscible with water, the diffusion between the two liquid phases resulted in a solution gradient, which induced self-assembly. With a traditional cosolvent method, the self-assembly process of PEG_{44}-*b*-PS_{190} starts when the THF content drops below approximately 77%. In the fast fluidic system, the steep solvent gradient at the two-phase boundary led to a small distance where the THF/dioxane content dropped to this limit. This short distance as well as the high surface to volume ratio resulted in a shortened timescale of mixing.[19]

In the traditional cosolvent method, the formation of structures starts with nucleation of a few unimer polymers, followed by a diffusion limited growth in size.[20] The final step is a slow exchange of unimer polymers to reach equilibrium. To study this process, copolymer was firstly dissolved in the organic solution in a batch experiment. Then water was delivered to it *via* a syringe pump. This process was monitored via dynamic light scattering (DLS) in a flow mode.[21] Both relaxation time and vesicle formation kinetics can be derived from the plot of the scattered light intensity against time, large positive amplitudes indicating vesicle

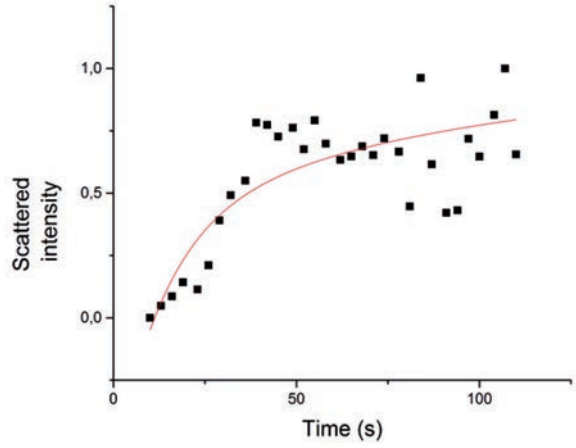

Figure 5.4. Scattered light intensity as a function of time (black squares); the plot was fitted with a double exponential function (red curve) I=1-(C1*exp(-t/τ1)+C2*exp(-t/τ2)). Relaxation approach is very useful for kinetics determination in liquid phase. In this experiment, the curve can be fitted with a double exponential function indicating a two step process involved in the initial stages of vesicle formation before it experience a longer process towards final equilibrium. The τ1 was derived as 33.7 s while τ2 was obtained as 152.1 s. The time was higher than the mixing time (in the range of 500 ms – 3 s) in a fluidic channel.

formation. In the case of the fluidic channel set-up, the calculated solvent mixing time is smaller than the aggregation time as determined from the batch experiment (see Figure 5.4). In addition, the polymer diffusion inside the organic solvent is two orders of magnitude lower than that of the two organic and aqueous phases.[22] The formation of polymeric assemblies is therefore dependent on flow rate/hydrodynamic conditions and the induced local polymer concentration, leading to kinetically trapped shapes instead of dynamic stable structures.

As flow rate and polymer concentration are expected to play an important role in control of self-assembly, we sought to vary the size and morphology of the structures by tuning the mixing factors employing this fluidic device. Additionally we hypothesized that maintaining flow conditions or not during collection would also affect the final morphology, so different collection methods were studied.

As initial conditions, we used a concentration of 10 mg/mL of PEG_{44}-*b*-PS_{190} and a flow rate of C1:C2:C3 = 10:10:10 mL/h. The self-assembled structures were collected in two ways: i) via the "insertion method" in which the collecting tube was inserted into water, ii)

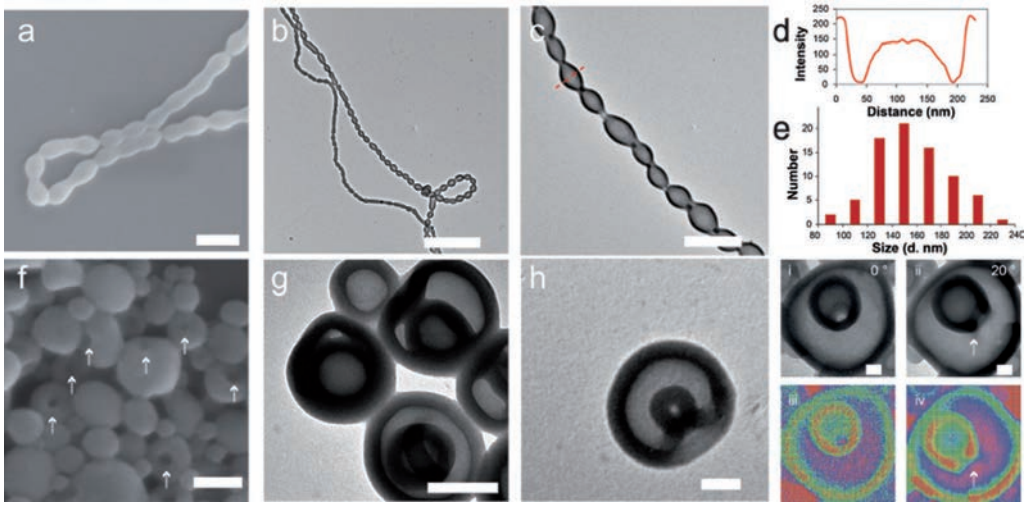

Figure 5.5. a) Scanning electron microscope (SEM) images of polymeric nanotubes, scale bar represents 500 nm; b) transmission electron microscope (TEM) images of polymeric nanotubes at lower magnification (scale bar = 2 μm); c) polymeric nanotubes at higher magnification (scale bar = 500 nm); d) plot profile of a vesicle unit/cross section in the polymeric nanotubes indicated by the red dashed line in c); showing intensity as function of distance over the cross section; e) size/diameter distribution diagram of the vesicle units in polymeric nanotubes (80 assemblies were counted); f) SEM images of polymeric vesicles, scale bar represents 150 nm, the white arrows pointing to the openings of stomatocyte vesicles; (g, h) TEM images of fabricated stomatocyte vesicles, scale bar is 100 nm and 50 nm respectively; (i, ii) TEM images of a polymersome stomatocyte at a tilting angle of 0° and 20°, respectively; (note the top and side view of the stomach) (iii, iv) corresponding 3D intensity profiles of the same stomatocyte, the white arrow pointing to the opening of the stomatocyte vesicle.

via the “dripping method” in which the output was dripped into water. Via both methods the outflow of the samples in a large excess of water led to the final vitrification of the vesicular structures. For determination of size and shape, the collected samples were then characterized by TEM without additional processing. In the case of the “dripping method”, vesicles were observed, while notably necklace-like nanotubes were generated via the “insertion method”. There are only a few reports about tubular structures, or necklace-like nanotubes. Helmerson *et al*. described the fabrication of necklace-like nanotubes with poly(butadiene-*b*-ethylene oxide) using a combination of optical tweezer pulling and micropipetting.[15d] In our case, necklace-like nanotubes could be generated in a simple and continuous way (Figure 5.5a, b, c).

The nanotube membrane was clearly observed in the TEM images, reflecting its vesicular properties. The average diameter of the polymeric nanotubes was 152 nm. (Shown in Figure 5.5d is the intensity profile of a vesicle unit in a polymeric nanotube. The diameter of this vesicle unit was approximately 150 nm.) Average diameter at the neck of the polymeric nanotubes was 45 nm. The tube lengths could reach 35 µm at maximum. For tuning the length of polymeric nanotubes, shearing forces (introduced by vigorous magnetic stirring) during collection were varied. When the stirring rate was increased to 500 rpm and 1000 rpm, the average tubes length decreased to 10.8 µm and 7.6 µm while the average length of tubes obtained without agitation was 14.8 µm (Figure 5.6a-c). In all other cases the outflow was collected without stirring. The membrane thickness of the polymeric nanotube was close to that of spherical vesicles obtained by the dripping method (20 nm). Polymeric nanotubes were only observed with the “insertion method”. Furthermore, sampling of the outflow directly from the device exit tube and fast quenching of the structures into liquid nitrogen shows the presence of vesicles by TEM. This indicates that the nanotube formation occurs outside of the device. We think that the high concentration of flexible vesicles pushed by the flow and slowed down at the exit in water as well as the presence of high concentration of plasticizing agent in a small local volume facilitate the colliding and merging of the vesicles.

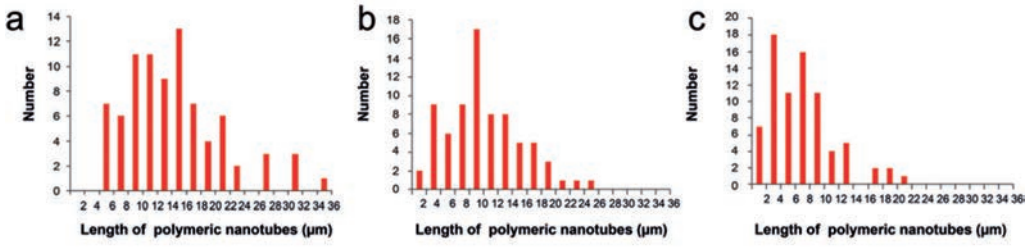

Figure 5.6. TEM analysis of the length of polymeric nanotubes collected with the insertion method a) at a stirring rate of 0 rpm; b) at a stirring rate of 500 rpm; c) at a stirring rate of 1000 rpm; For each analysis 80 assemblies were counted.

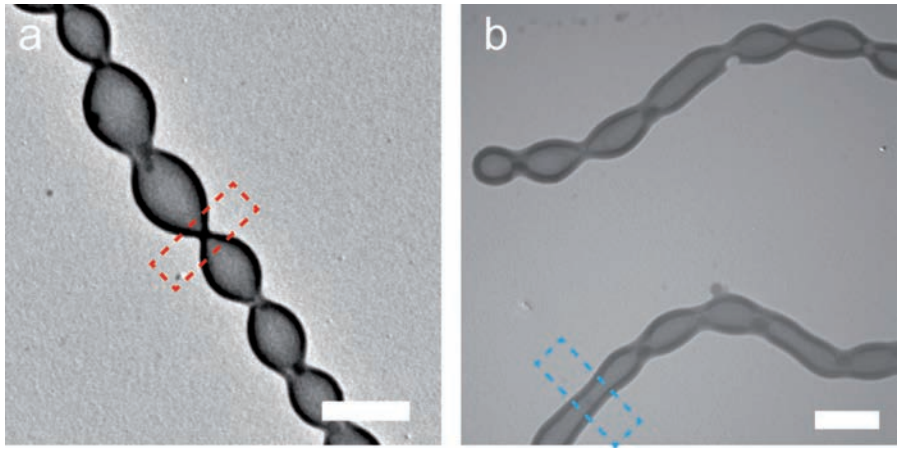

Figure 5.7. Transmission electron microscopy image of polymer nanotubes. a) Shown in rectangle is the connecting section of two neighbouring vesicles in hemifusion state; b) within the rectangle is the area where two neighbouring vesicles are more connected. The scale bar represents 300 nm.

The flow direction and shear force favour the formation of one-directional polymeric nanotubes instead of merged large vesicles. The fusion could be indicated by the fact that in certain sections, the neighbouring vesicle unit was not completely connected but instead shared a center wall and was in a hemifusion state (Figure 5.7a). This was suggested previously as an intermediate state of unilamilar polymersomes fusion.[23] Previous reports[24] have shown that vesicle to fused nanorod transition occurs two order of magnitude more rapid than its reverse way. Therefore we think the likelyhood of first formation of giant vesicles and later fission into polymersome necklaces is relatively low. Another possibility to explain the nanotube formation was previously suggested to be unimer insertion, however this was connected to an experiment in a dilute batch system with no possibility for fusion.[25] In this case, the growth rate (insertion of new unimers) is faster than the birth rate of new vesicles. Due to immiscibility of constitutional polymer chains in the bilayer vesicle membrane, one copolymer has to overcome very high-energy barrier to go from the outer layer into the inner layer of the vesicles. Therefore the outer membrane would grow faster than the inner ones. To reduce the resulting tension, elongated structures are obtained. In this case vesicle curvature is expected to decrease. This could be an explanation for the less curved section in the nanotubes (Figure 5.7b).

With the “dripping method”, the vesicles and plasticizing agent were diluted and quenched by a large amount of water in a short time, therefore only vesicles were obtained. It is interesting to observe that among polymeric vesicles, bowl shaped vesicles/“stomatocytes” could be formed (Figure 5.5f, g, h). In Figure 5.5f, the openings of stomatocytes were clearly

shown. To be noted only openings facing towards the front were visible in the SEM images. In TEM images (Figure 5.5g, h), the polymer membrane fold-in and the formed cavities were clear. The stomatocytes structure could account for maximum 54% in the vesicle population (based on 155 specimen assessed by TEM). Shown in Figure 5.5i-iv was the TEM of stomatocytes at different angles (top view and side view), in which the top view of the stomatocyte should be differentiated from the multilamellar vesicle. One possible mechanism could be that during the fast mixing process at the interface of two liquid phases, the inner compartment of the formed spherical vesicles is still filled with THF/dioxane.

With the tuned ratio of THF/dioxane, the swelling extent of PS can be so well controlled that the newly formed membrane is only permeable to organic solvent but not to water. At the phase boundary, the solvent gradient induced organic solvent outward diffusion and evaporation of the organic solvent entrapped inside could be responsible for the formation of an osmotic gradient, leading to membrane folding and bowl-shaped structures formation.[26]

Besides the collecting methods, we also explored the impact of initial polymer concentration

a

	polymeric structure morphology	
polymer concentration (mg/mL)	insertion method	dripping method
1	vesicles	vesicles
10	polymeric nanotubes	vesicles
20	polymeric nanotubes	polymeric nanotubes

b

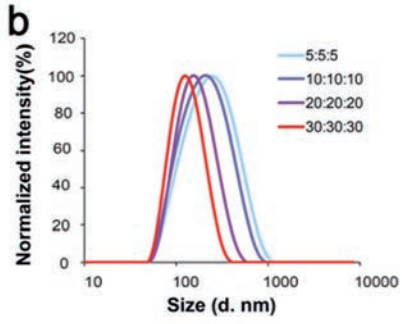

c

polymer concentration (mg/mL)	polymeric structure morphology	flow rate C1:C2:C3 (mL/h)	size (d. nm)	polydispersity index
1	vesicles	30:30:30	123.8	0.092
2	vesicles	30:30:30	130.9	0.156
3	vesicles	30:30:30	150.0	0.173
10	vesicles	30:30:30	200.9	0.169
1	vesicles	10:10:10	214.1	0.180
1	vesicles	10:5:10	189.3	0.220

Figure 5.8. a) Morphologies of polymeric structures were tuned by changing collecting methods and polymer concentration; b) sizes of vesicles were tuned by changing flow rate; particles intensity percentage was plotted against the diameter of the vesicles (dynamic light scattering/DLS data); c) Tuning size/diameter (DLS data) of vesicles by changing polymer concentration and flow ratio between main channel and side channel.

on the morphology. We already know at a concentration of 10 mg/mL vesicles were obtained with the dripping method and nanotubes were generated with the insertion method. At a lower concentration (1 mg/mL) we found that only vesicles were observed using either "insertion method" or "dripping method", while nanotube structures were observed in both cases for the higher initial polymer concentration of 20 mg/mL (Figure 5.8a).

Next, we explored the ability to control the size of the vesicles via modifying the hydrodynamic parameters. A low concentration of polymer solution (1 mg/mL) was used to avoid the formation of polymeric nanotube structures. The dripping method was used to collect outflow from the fluidic channel. Keeping the flow ratio of polymer solution and aqueous solution constant at 1:1, the vesicles experienced a decrease in diameter from 218 to 123 nm when the flow rate was elevated from 5 mL/h to 30 mL/h (Figure 5.8b, DLS data). This is a result of the faster mixing process, which leads to a lower local polymer

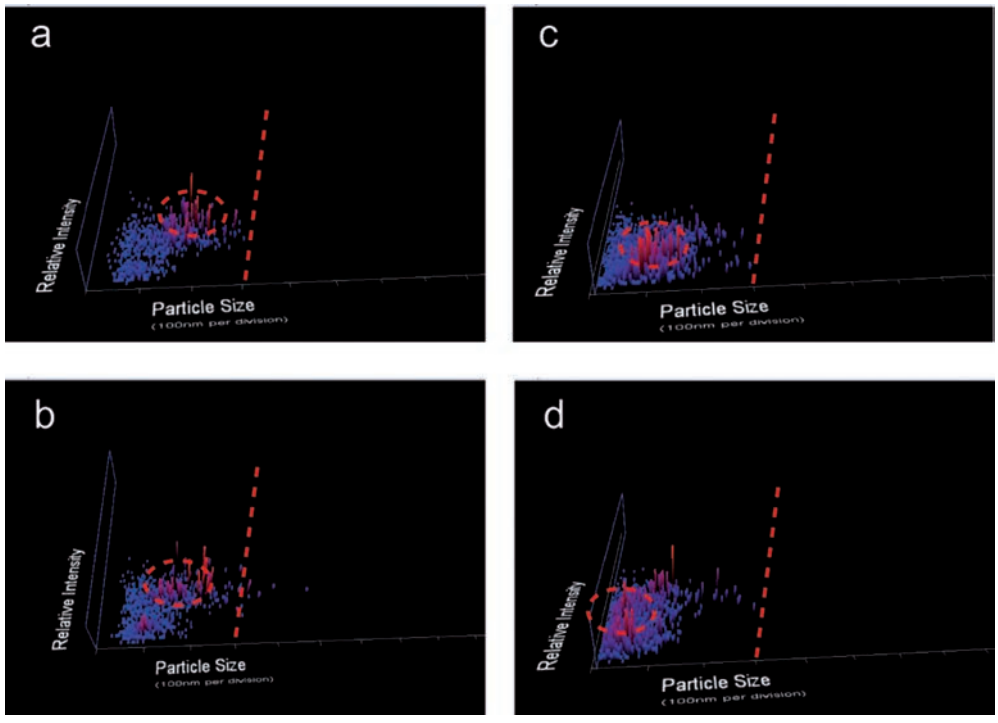

Figure 5.9. Vesicle size experienced a decrease by increasing flow rate a) 5 mL/h; b) 10 mL/h; c) 20 mL/h; d) 30 mL/h (nanoparticle tracking analysis/NTA data). Shown above are 3D plots of particle size (x axis) vs. intensity (y axis, 100 nm per division) vs. particle concentration (z axis).The red bars (within the red dashed circle) represent the main particle population. The NTA technique is based on particle-by-particle tracking and can translate the obtained diffusion data to size using Stokes- Einstein equation. The NTA approach is not biased towards subgroups in a particle population.

concentration available to form vesicles. The results were also confirmed with nanoparticle tracking analysis (NTA) technique (Figure 5.9).

This NTA technique allows individual particle detection with a minimum detection limit as low as 10 nm. At a constant flow rate of polymer solution and aqueous solution of 30 mL/h, an increasing trend in size was observed when the initial polymer concentration was increased from 1 mg/mL to 10 mg/mL (Figure 5.8c). In addition with a concentration of 1 mg/mL polymer solution, the size of vesicles decreased from 214 to 189 nm when the flow

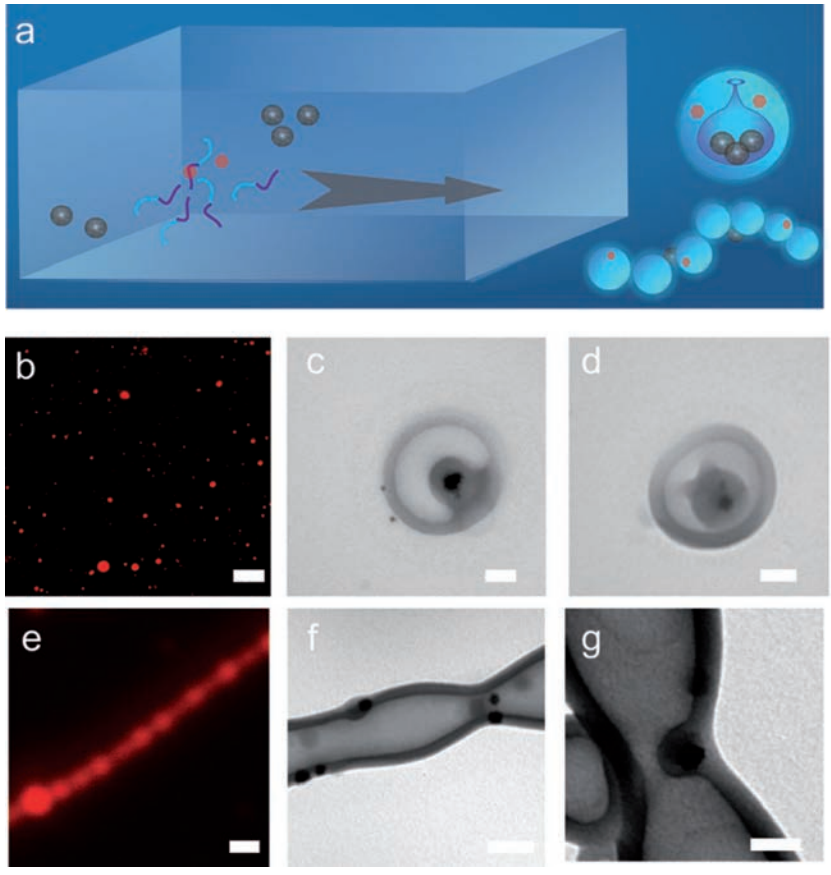

Figure 5.10. a) Schematic illustration of in situ loading of Nile red/platinum nanoparticles into stomatocyte vesicles and polymeric nanotubes. The Nile red/polymer in THF/dioxane solution was injected into the main channel (C2); platinum nanoparticles aqueous solution was pumped through the two side channels (C1/C3) of the fluidic device into the main fluidic channel; b) confocal fluorescent microscopy image of Nile red loaded vesicles, scale bar represents 2 µm; (c, d) TEM images of platinum nanoparticles loaded stomatocytes fabricated through the microfluidic method, scale bar represents 50 nm; e) confocal fluorescent microscopy image of Nile red loaded vesicles, scale bar represents 500 nm; (f, g) TEM images of polymeric nanotubes functionalized with PVP coated platinum nanoparticles. Scale bar is 50 nm.

ratio of polymer solution and aqueous solution (C2: C1/C3) was changed from 1:1 to 1:2. It should be noted that all the vesicles prepared above were narrowly distributed in size as indicated by the polydispersity value in Figure 5.8c.

After obtaining the polymeric nanotube and vesicle structures, we investigated the ability to incorporate hydrophobic cargo, by mixing the fluorescent dye Nile red with the polymer organic solution before injection into the middle channel (Figure 5.10a). An initial polymer concentration of 10 mg/mL was used and the flow rate of side and main channels was maintained at 10 mL/h. Polymeric nanotubes obtained by insertion method and vesicles generated by dripping method could be clearly visualized with confocal fluorescence microscopy using Nile red's fluorescence (Figure 5.10b, e) Since the diffraction limit of the confocal microscope is about 200 nm,[27] it could not be differentiated whether Nile red was localized on the membrane or the inner compartments. Besides the hydrophobic Nile red, the hydrophilic fluorescent drug doxorubicin could also be loaded. (Figure 5.11)

We subsequently explored the possibility of entrapping nanoparticles in the stomatocyte and nanotube structures by addition of platinum nanoparticles (PtNPs) to the aqueous solution. The initial polymer concentration in THF/dioxane was kept at 10 mg/mL. PtNPs were fabricated through reduction of $KPtCl_4$ and capped with poly(vinyl pyrrolidone) (PVP, MW 10000 Da).[28] The platinum nanoparticles were well dispersed in water (48.9 ± 3.3 nm, 5.06 ± 0.1 × 10^{11} particles/mL). With a flow rate of 10 mL/h, PtNPs-loaded stomatocytes were obtained with the "dripping method" (Figure 5.10c, d). The PtNPs loading efficiency reached approximately 42% (TEM assessment on 50 specimens). Smaller PtNPs loaded stomatocytes (189 nm) were obtained, compared to stomatocytes prepared by the conventional cosolvent method (325 nm). In previous reports inorganic nanoparticles were

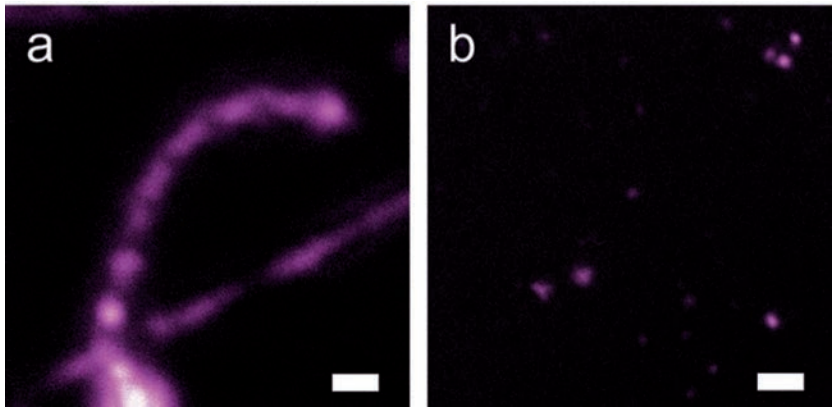

Figure 5.11. Confocal microscopy fluorescent images of hydrophilic doxorubicin hydrochloride loaded a) nanotubes, scale bar = 500 nm; b) vesicles, scale bar = 2 μm.

loaded into the membrane of polymersomes so only nanoparticles smaller than membrane thickness could be loaded.[29] In our case PtNPs were loaded in the cavity of polymersome stomatocytes. Therefore there will be no influence on the vesicle membrane and the stability of the vesicles. When the "insertion method" was applied, polymeric nanotubes were obtained which were functionalized with PtNPs (Figure 5.10f, g). The PVP capped PtNPs were found to be preferentially located in the junction of the nanotube where the curvature was highest.

5.3. CONCLUSION

A fast and simple method has been developed to fabricate self-assemblies with non-spherical morphology. With our method, nanotubes and stomatocytes could be produced in a continuous and well-defined fashion. Furthermore, injection of an aqueous solution containing PtNPs into the microfluidic channel resulted in encapsulation of the particles in both types of structures. This versatile approach can be used for scaled-up production of polymeric vesicles with non-spherical morphologies.

5.4. ACKNOWLEDGEMENTS

Yingfeng Tu and Nan-nan Deng are gratefully acknowledged for their contribution to this chapter. Roeland Nolte is thanked for valuable discussions.

5.5. EXPERIMENTAL SECTION

Materials

Styrene, N, N, N', N", N"-pentamethyl diethylene triamine (PMDETA), methoxy poly(ethylene glycol) (MW 2000 Da), poly(vinyl pyrrolidone) (MW 10000 Da), potassium tetrachloro platinate (II), L (+) ascorbic acid were purchased from Sigma-Aldrich. Nile red was obtained from Chem-Impex. Doxorubicin hydrochloride was purchased from LC Laboratories. Styrene was purified by distillation under reduced vacuum prior to use. Copper bromide was obtained from Fluka. Anisole and tetrahydrofuran (THF) were purchased from Acros. Dioxane was from Biosolve. All chemicals are used as received unless otherwise indicated. Aqueous solutions were prepared with MilliQ water, which was double deionized with a MilliQ QPOD purification system (18.2 MΩ).

Instruments

^{1}H nuclear magnetic resonance spectra (^{1}H NMR) were measured on a Varian Inova 400 MHz spectrometer, with $CDCl_3$ as solvent. The hydrodynamic diameter of polymeric vesicles was determined with a Malvern Zetasizer Nano S using the following conditions: temperature 25°C, He-Ne laser wavelength 633 nm and detector angle 173°. Transmission electron microscopy was performed on a JEOL 1010 Transmission Electron Microscope with MegaView Soft Imaging camera at an acceleration voltage of 60 kV. Scanning electron microscopy images were obtained with JEOL 6330 Cryo Field Emission Scanning Electron Microscope (FESEM). For nanoparticle tracking measurements, a NanoSight NS500 (Malvern Instruments) was used.

Synthesis of poly(ethylene glycol)$_{44}$-*b*-polystyrene$_{190}$ (PEG$_{44}$-*b*-PS$_{190}$)

Poly(ethylene glycol)$_{44}$-*b*-polystyrene$_{190}$ was synthesized by atom transfer radical polymerization, via a protocol reported in literature.[17a] To monitor the polymerization process, ^{1}H NMR spectroscopy was used for determining the molecular weight of the block copolymer. The reaction was terminated once the desired MW 21 kg/mol was reached. The crude product was purified by precipitation three times from dichloromethane in methanol. The ^{1}H NMR spectra of the PEG initiator and purified copolymer are shown in Figure 5.1.

Fabrication of platinum nanoparticles/PtNPs with PVP coating

Platinum nanoparticles capped with poly(vinyl pyrrolidone) (PVP) were synthesized according to a previously reported method. Briefly, PVP (MW = 10000 Da, 20 mg) was mixed with an aqueous solution of K_2PtCl_4 (20 mM, 2 mL). After magnetic stirring for 48 hours at room temperature, 1 mL of reducing agent ascorbic acid (0.2 mM) was rapidly injected to the above solution. After stirring for 1 min, the resulting solution was incubated in a sonication bath (VWR Ultrasonic Cleaner Model 75D) at room temperature for 40 min. The appearance of a black color indicated the completion of reduction. The obtained platinum nanoparticles were centrifuged (12000 rpm, 10 min) and washed 3 times with MilliQ water to remove remaining salt. Before each use, the above obtained platinum solution was sonicated for 20 seconds and diluted with MilliQ water. The concentration and size of platinum nanoparticles were determined by the Nanosight.

Preparation of polymer vesicles with co-solvent method

10 mg poly(ethylene glycol)$_{44}$-*b*-polystyrene$_{190}$ was dissolved in 1 mL THF/dioxane (4:1, v:v) and stirred for 30 min. Then MilliQ water (3 mL) was slowly added into the polymer organic solvent through a syringe pump (Fusion 100, KR analytical) with a rate of 1 mL/h. After addition of water, the solution was immediately transferred to a dialysis bag (MW cutoff 12000-14000 Da) and dialyzed against MilliQ water (800 mL) for at least 48 hours to

remove remaining organic solvent. For monitoring the kinetic process of vesicle formation, MilliQ water was delivered to the polymer organic solution in a flow cuvette. The plot of scattered light intensity along time was recorded under the flow mode of dynamic light scattering (DLS).

Preparation of platinum nanoparticles/PtNPs loaded stomatocytes with co-solvent method

Poly(ethylene glycol)$_{44}$-*b*-polystyrene$_{190}$ (10 mg) was allowed to be fully dissolved in 1 mL THF/dioxane (4:1) solvent. Then MilliQ water (0.35 mL), followed by a platinum nanoparticle solution (0.65 mL) was slowly delivered into the polymer organic solvent through a syringe pump (Fusion 100, KR analytical) (1 mL/h) with vigorous stirring. After 1 h, the solution was transferred to a dialysis bag (MW cutoff 12000-14000 Da) and dialyzed against MilliQ water (800 mL) for at least 48 hours with frequent change of water.

Preparation of polymer vesicles with fluidic channels

The fluidic channel (glass/plastic) consisted of three inlet channels (0.4 mm deep, 1 mm wide, 12 mm long) and a main channel (0.4 mm deep, 3 mm wide, 24 mm long). Poly(ethylene glycol)$_{44}$-*b*-polystyrene$_{190}$ was dissolved in THF/dioxane (4:1, v:v) to obtain the desired polymer concentration, and injected into the main channel via the middle inlet channel, while water was injected into the two side channels using syringe pumps (Fusion 100, KR analytical) at a set flow rate. For Nile red loading, 20 µL of Nile red in DMF (6 mg/mL) was added to the polymer solution. In case doxorubicin hydrochloride was loaded, a 0.5 mg/mL aqueous solution instead of water was pumped through the two side channels. For the loading of platinum nanoparticles an aqueous PtNPs solution (PtNPs concentration 5.06 ± 0.1 × 10^{11} particles/mL) instead of water was injected into the side channels. For polymeric nanotubes collection with shearing force, outflow was collected while magnetically stirred at 0, 500, 1000 rpm (IKA® Big Squid magnetic stirrers).

Transmission electron microscopy (TEM)

Sample specimens were prepared by casting 6 µL of diluted fresh sample aliquots onto 300 mesh copper grids coated with carbon films. The grid was allowed to dry for at least 8 hours at room temperature. For the “freezing” sample preparation, 6 µL of channel outflow was quickly casted onto the carbon film coated grid and transferred to liquid nitrogen (approximately 3 s) for structure “freezing”. Then the grid was left to dry under vacuum overnight. Image acquisition was operated with iTEM software (Olympus). For diameter and membrane thickness measurement, ImageJ software plot profile plugin was used. 80 vesicles or nanotubes were measured to determine an average diameter/membrane thickness.

Scanning electron microscopy (SEM)

6 µL of aqueous sample was applied on a copper grid and allowed to dry overnight. The grid was placed on a SEM mount with a double sided tape, followed by gold (60%)/palladium (40%) sputtering for 30 seconds in a Cressington 208 HR sputter coater. Then the grid was transferred to the microscope chamber for imaging.

Dynamic light scattering (DLS)

Dynamic light scattering analysis of samples was performed on a Malvern Zetasizer Nano S instrument. Samples were typically loaded in Malvern microcuvettes with a minimum volume of 60 µL. The data acquired was processed with Malvern Instruments Dispersion Technology software.

Nanoparticle tracking analysis technique (NTA)

The sample solution was diluted 2000 times and pumped into the NanoSight NS500 sample chamber. Five videos (each video duration time 60 seconds, rate 30 frames/sec) were recorded and the particle movement was analyzed with nanoparticle tracking technique software. Particle concentration was based on the average particle number in a frame. After averaging the values obtained from 5 videos, the concentration of the platinum nanoparticles solution before dilution was determined to be $5.06 \pm 0.1 \times 10^{11}$ particles/mL while the mean size of the particles was obtained as 48.9 ± 3.3 nm.

Confocal laser scanning microscope (CLSM)

Fluorescent Nile red/doxorubicin hydrochloride loaded polymer structures were visualized with a confocal fluorescence laser scanning microscope (Leica TCS SP2 AOBS). To observe Nile red, an argon laser line (514 nm) with a detection window of 590 – 650 nm was used. Doxorubicin hydrochloride was excited with an argon laser line (488 nm) and the resulting emission was collected between 550-650 nm. The laser beam was focused on the sample through a 63X oil immersion lens. A pinhole of 400 µm was selected. An average of two scans was used.

5.6. REFERENCES

[1] a) B. M. Discher, Y. Y. Won, D. S. Ege, J. C. M. Lee, F. S. Bates, D. E. Discher, D. A. Hammer, *Science* **1999**, *284*, 1143-1146; b) F. Ahmed, R. I. Pakunlu, G. Srinivas, A. Brannan, F. Bates, M. L. Klein, T. Minko, D. E. Discher, *Mol. Pharm.* **2006**, *3*, 340-350; c) H. E. Colley, V. Hearnden, M. Avila-Olias, D. Cecchin, I. Canton, J. Madsen, S. MacNeil, N. Warren, K. Hu, J. A. McKeating, S. P. Armes, C. Murdoch, M. H. Thornhill, G. Battaglia, *Mol. Pharm.* **2014**, *11*, 1176-1188.

[2] a) H. Bermudez, A. K. Brannan, D. A. Hammer, F. S. Bates, D. E. Discher, *Macromolecules* **2002**, *35*, 8203-8208; b) R. Rodriguez-Garcia, M. Mell, I. Lopez-Montero, J. Netzel, T. Hellweg, F. Monroy, *Soft Matter* **2011**, *7*, 1532-1542.

[3] S. H. Kim, H. C. Shum, J. W. Kim, J. C. Cho, D. A. Weitz, *J. Am. Chem. Soc.* **2011**, *133*, 15165-15171.

[4] R. P. Brinkhuis, K. Stojanov, P. Laverman, J. Eilander, I. S. Zuhorn, F. P. Rutjes, J. C. van Hest, *Bioconjug. Chem.* **2012**, *23*, 958-965.

[5] Z. Wang, M. C. van Oers, F. P. Rutjes, J. C. van Hest, *Angew. Chem. Int. Ed.* **2012**, *51*, 10746-10750.

[6] P. L. Soo, A. Eisenberg, *J. Polym. Sci. Pol. Phys.* **2004**, *42*, 923-938.

[7] a) J. R. Howse, R. A. Jones, G. Battaglia, R. E. Ducker, G. J. Leggett, A. J. Ryan, *Nat. Mater.* **2009**, *8*, 507-511; b) P. P. Ghoroghchian, G. Z. Li, D. H. Levine, K. P. Davis, F. S. Bates, D. A. Hammer, M. J. Therien, *Macromolecules* **2006**, *39*, 1673-1675.

[8] S. Rameez, I. Bamba, A. F. Palmer, *Langmuir* **2010**, *26*, 5279-5285.

[9] P. P. Ghoroghchian, P. R. Frail, K. Susumu, D. Blessington, A. K. Brannan, F. S. Bates, B. Chance, D. A. Hammer, M. J. Therien, *P. Natl. Acad. Sci. USA* **2005**, *102*, 2922-2927.

[10] H. C. Shum, J. W. Kim, D. A. Weitz, *J. Am. Chem. Soc.* **2008**, *130*, 9543-9549.

[11] J. Thiele, V. Chokkalingam, S. H. Ma, D. A. Wilson, W. T. S. Huck, *Mater. Horizons* **2014**, *1*, 96-101.

[12] N. N. Deng, J. Sun, W. Wang, X. J. Ju, R. Xie, L. Y. Chu, *ACS Appl. Mater. Inter.* **2014**, *6*, 3817-3821.

[13] a) J. Thiele, D. Steinhauser, T. Pfohl, S. Forster, *Langmuir* **2010**, *26*, 6860-6863; b) R. Bleul, R. Thiermann, G. U. Marten, M. J. House, T. G. St Pierre, U. O. Hafeli, M. Maskos, *Nanoscale* **2013**, *5*, 11385-11393; c) L. Brown, S. L. McArthur, P. C. Wright, A. Lewis, G. Battaglia, *Lab Chip* **2010**, *10*, 1922-1928.

[14] a) K. Y. Win, S. S. Feng, *Biomaterials* **2005**, *26*, 2713-2722; b) A. Prokop, J. M. Davidson, *J. Pharm. Sci.* **2008**, *97*, 3518-3590.

[15] a) J. Grumelard, A. Taubert, W. Meier, *Chem. Commun.* **2004**, 1462-1463; b) J. D. Robertson, G. Yealland, M. Avila-Olias, L. Chierico, O. Bandmann, S. A. Renshaw, G. Battaglia, *ACS Nano* **2014**, *8*, 4650-4661; c) J. He, Y. J. Liu, T. Babu, Z. J. Wei, Z. H. Nie, *J. Am. Chem. Soc.* **2012**, *134*, 11342-11345; d) J. E. Reiner, J. M. Wells, R. B. Kishore, C. Pfefferkorn, K. Helmerson, *Proc. Natl. Acad. Sci. U S A* **2006**, *103*, 1173-1177; e) J. Raez, R. Barjovanu, J. A. Massey, M. A. Winnik, I. Manners, *Angew. Chem. Int. Ed.* **2000**, *39*, 3862-3865; f) J. Raez, I. Manners, M. A. Winnik, *J. Am. Chem. Soc.* **2002**, *124*, 10381-10395.

[16] S. Takayama, E. Ostuni, X. P. Qian, J. C. McDonald, X. Y. Jiang, P. LeDuc, M. H. Wu, D. E. Ingber, G. M. Whitesides, *Adv. Mater.* **2001**, *13*, 570-574.

[17] a) K. T. Kim, J. J. L. M. Cornelissen, R. J. M. Nolte, J. C. M. van Hest, *Adv. Mater.* **2009**, *21*, 2787-2791; b) F. H. Meng, G. H. M. Engbers, A. Gessner, R. H. Muller, J. Feijen, *J. Biomed. Mater. Res. A* **2004**, *70A*, 97-106.

[18] A. S. Utada, E. Lorenceau, D. R. Link, P. D. Kaplan, H. A. Stone, D. A. Weitz, *Science* **2005**, *308*, 537-541.

[19] R. Karnik, F. Gu, P. Basto, C. Cannizzaro, L. Dean, W. Kyei-Manu, R. Langer, O. C. Farokhzad, *Nano Lett.* **2008**, *8*, 2906-2912.

[20] B. K. Johnson, R. K. Prud'homme, *Phys. Rev. Lett.* **2003**, *91*, 118302.

[21] a) L. Shen, J. Z. Du, S. P. Armes, S. Y. Liu, *Langmuir* **2008**, *24*, 10019-10025; b) L. Chen, H. W. Shen, A. Eisenberg, *J. Phys. Chem. B* **1999**, *103*, 9488-9497.

[22] R. Thiermann, W. Mueller, A. Montesinos-Castellanos, D. Metzke, P. Lob, V. Hessel, M. Maskos, *Polymer* **2012**, *53*, 2205-2210.

[23] H. Y. Chang, Y. L. Lin, Y. J. Sheng, H. K. Tsao, *Macromolecules* **2013**, *46*, 5644-5656.

[24] L. B. Luo, A. Eisenberg, *Langmuir* **2001**, *17*, 6804-6811.

[25] K. Iyama, T. Nose, *Macromolecules* **1998**, *31*, 7356-7364.

[26] a) D. A. Wilson, R. J. M. Nolte, J. C. M. van Hest, *Nat. Chem.* **2012**, *4*, 268-274; b) F. Peng, Y. F. Tu, J. C. M. van Hest, D. A. Wilson, *Angew. Chem. Int. Ed.* **2015**, *54*, 11662-11665; c) L. K. E. A. Abdelmohsen, M. Nijemeisland, G. M. Pawar, G. J. A. Janssen, R. J. M. Nolte, J. C. M. van Hest, D. A. Wilson, *ACS Nano* **2016**, *10*, 2652-2660.

[27] a) Z. B. Wang, W. Guo, L. Li, B. Luk'yanchuk, A. Khan, Z. Liu, Z. C. Chen, M. H. Hong, *Nat. Commun.* **2011**, *2*, 218; b) M. Fukuta, S. Kanamori, T. Furukawa, Y. Nawa, W. Inami, S. Lin, Y. Kawata, S. Terakawa, *Sci. Rep. Uk* **2015**, *5*, 16068.

[28] a) E. G. Jung, Y. Shin, M. Lee, J. Yo, T. Kang, *ACS Appl. Mater. Inter.* **2015**, *7*, 10666-10670; b) Y. J. Song, Y. Yang, C. J. Medforth, E. Pereira, A. K. Singh, H. F. Xu, Y. B. Jiang, C. J. Brinker, F. van Swol, J. A. Shelnutt, *J. Am. Chem. Soc.* **2004**, *126*, 635-645; c) L. Wang, Y. Yamauchi, *J. Am. Chem. Soc.* **2009**, *131*, 9152-9153.

[29] a) R. J. Hickey, A. S. Haynes, J. M. Kikkawa, S. J. Park, *J. Am. Chem. Soc.* **2011**, *133*, 1517-1525; b) B. M. Geilich, A. L. van de Ven, G. L. Singleton, L. J. Sepulveda, S. Sridhar, T. J. Webster, *Nanoscale* **2015**, *7*, 3511-3519.

6 Perspective and outlook

FROM CONCEPTION TO REALIZATION

The visionary talk given by Richard Feynman “there is plenty room in the bottom” has very much inspired the start and development of nanotechnology. The field of synthetic motors has evolved from a centimeter sized motor prototype to micron sized and nanometer sized motors (as small as 30 nm). Synthetic motility is demonstrated not only at a macroscopic range but also at the nanometer scale where different physical parameters are dominant. The miniaturized devices promise to interact with and manipulate objects through directed and controlled motion, from micrometer scale to nanometer scale. Developing the ability to manipulate at smaller dimensions and with increasing speeds has the potential to bring revolutionary transformation to multiple fields.

Over the past decade, the research field of micron- and nano-sized motors has expanded considerably, with objects of different composition, different designs and different propulsion mechanisms being developed. With the broadened choices of devices, extending the application scope is a logical next step. Using intelligent miniaturized motors for the biomedical domain is an interesting direction.

Micro- and nano-sized devices are excellent candidates for carrying out non-invasive investigations of organ, tissue, even cell behavior. How intelligent the devices could be is a frequently asked question. Being small, the motors usually lack the sophistication of their biological counterparts and more macroscopic synthetic objects. It would be exciting and feasible to incorporate multiple functions, for instance diagnosis, therapy and post-therapy evaluation, into a single motor system. In addition developing motors that are interactive with an external field or communicative with controlling software is attractive. A motor system with a built-in communication module may function as a diagnose-therapy platform for personalized medication.

Besides a field responsive motor, a motor system that is responsive to local stimuli and can be self guided to the biological target (taxis) seems mandatory when considering the complex vasculature network system. A next step would therefore be the development of motors that can smartly sense different stimuli (besides hydrogen peroxide) and automatically make decisions. An in-depth investigation of taxis mechanism is required to guide the future design of motors with taxis behavior.

In a general sense, micro/nanomotors belong to the family of micro/nano machines/ robotics. The tasks performed by micro/nano machines should also be possible for motors to carry out, yet at higher velocity. For the micro/nanomachines, many opportunities arise in the fields of microbiology (transport or being transported by microorganism), hematology (oxygen transporting, clotting), dentistry (penetrating dental tubules, root canal procedure), neurosurgery (axon transection). In principle these are also applicable to motor systems at a higher speed. The applications for motors are not necessarily limited to those already found with existing micro/nanomachine systems. Very interesting advantages arise from

using the autonomous motion of fast moving particle. With autonomous motion, it is envisioned that the device is not restricted by the blood/lymphatic fluid flow and enables more facile access to diseased tissues or deep solid tumors. The motion induced liquid mixing can be also used for drug dispensing.

When applied in a clinical setting, biocompatibility, biodegradability and recyclability are important issues to consider. As a large amount of motor systems (especially motors powered via electrophoresis) are non-degradable metal-based, the fate of these motors in biological systems needs to be carefully examined. Developing motors that can be recycled or composed of biodegradable/biocompatible materials will be a solution.

Other practical issues involve the mass production of motors. Most motors now are synthesized via complicated construction procedures which rely on expensive instruments, such as micro-electro-mechanical techniques for fabrication. For commercialization and realistic use, simplification of the production process is needed.

Summary

Nature has been a great inspiration for the science community. Taking inspiration from the highly efficient biological motors, scientists are aiming to develop their synthetic counterparts. After a decade of booming research interest, micro and nanomotors comprising a diverse set of materials, sizes and propulsion mechanisms are presented. How to translate the proof-of-concept research into realistic application remains an interesting yet challenging question. **Chapter 1** first describes briefly the development of the micro/nanomotors, followed by an overview of the efforts to implement these motor systems for diverse in vivo applications. In this chapter the emerging applications of nanomotors at the cell, tissue, and body fluid level are illustrated. Successful trials and possible limitations lying ahead are discussed.

As drug delivery is an important aspect for biomedical applications, we explore the possibility of using our nanoscale bowl shaped polymersome based motors for drug delivery in the rest of the thesis. The utilities of bowl shaped polymersome motors in different biologically relevant environments are explored.

Achieving precise delivery in complicated biological environments has been a long standing problem for medication therapy. Especially regarding treatment of cancer and other chronic diseases, nanomedicine has not fully lived up to its promises. Conventional targeted delivery relies on “enhanced permeation and retention” through leaky tumor vasculatures and recognition of antigens. Side effects caused by “off-target” drugs are often high, however. Alternative approaches are therefore required. Nature uses the idea of “taxis” for organism guidance. In **chapter 2** we found the motility (diffusion) of nanomotors increases with elevated fuel concentrations. In a fuel gradient, there is a net displacement towards fuel rich regions, thus chemotaxis. With this we demonstrated the possibility of guiding nanomotors loaded with the antitumor drug doxorubicin towards hydrogen peroxide secreting neutrophils.

The hydrophobic nature and intactness of the cell membrane protect the cells from external molecules as well as therapeutic agents. For effective delivery, the cell membrane is one important barrier to overcome. After demonstrating targeted delivery towards model cells, in **chapter 3** we aimed to deliver drugs into the cell with the aid of peptide functionalized nanomotors. The nanomotors were grafted with a tat cell-penetrating peptide. For peptide modification, we used the reaction between cysteine group in tat and maleimide introduced on the nanomotor surface. The tat peptide, a basic domain from the tat protein of HIV, is responsible for facilitating efficient virus entry into host cells. By combining the cell penetrating peptide with autonomously moving motors, efficient penetration into intact cells was observed with confocal fluorescent microscopy.

In nature magnetotaxis is an interesting behavior observed in bacteria. These magnetotactic bacteria, for instance *Magnetospirillum magnetotacticum*, can produce a chain of nanometer sized iron oxide particles inside their body through a biomineralization process. With the chain of iron oxide nanoparticles coated with protein (magnetosome),

the bacteria can orient with the earth magnetic field direction as well as being attracted by an external magnetic field. Such magnetotaxis behavior shows profound potential in isolation/ accumulation, targeted delivery and magnetically induced hyperthermia therapy. In **chapter 4** we set out to mimic this behavior. Starting with doxorubicin incorporated and platinum nanoparticles preloaded stomatocytes, nickel metal was deposited *in situ* on the Pt surface in a controllable way using the catalytic activity of the platinum nanoparticles. The drug and Pt-Ni loaded stomatocytes in solution were found to be responsive to external magnetic fields. The system was dual-propelled (hydrogen peroxide powered and/or magnetic powered). The moving direction was varied on demand by changing the magnetic position or the field direction. This behavior was also demonstrated in a tumor tissue model with human cervical cancer cell (HeLa) loaded collagen gels. With an external field, the motors demonstrated guided motion in the tissue mimicking model and moved through the meshes of the gel.

It is known that the shape factor is very important for the circulation time and uptake process. In **chapter 5** we developed a flow method for fabricating non-spherical vesicles. As the mixing time of the flow device is shorter than the vesicle formation time, we could easily tune the hydrodynamic parameters and obtain kinetically trapped vesicles. With different flow rates/ratios and different initial polymer concentrations, vesicles of different shape (bowl shaped vesicles and vesicle necklaces) and size were produced. The collecting methods were also found to influence the final morphology of vesicles. Multiple payloads including hydrophilic and hydrophobic dyes/drugs and platinum nanoparticles were readily loaded. The incorporation of platinum nanoparticles makes it possible for the vesicles to act as motor systems. As the approach provides the possibility for up-scaling and continuous production of vesicles or vesicle based motors, new horizons are opened for practical applications.

Acknowledgement

The PhD journey which I described in the thesis was not carried out alone, it is a collaborative work of many many people I would like to express my big thanks! First and foremost, I would like to express my sincere gratitude to my supervisor Daniela. Always being optimistic and inspiring, your very positive attitude is motivating me along my whole PhD period. Besides inspiring me to have new ideas myself and make me firmly believe “there is plenty of projects we could do”, you always have so many ideas and tips when we have discussions. Each time after our discussion, I am offered so many choices that I knew I had plenty of things to do before next meeting. Thank you for your career suggestions! I will always remember the time that you asked me “what’s your future plan” in my second year. Thank you so much for reminding me and preparing me in advance of time for the future career. I will remember those moments that you share your experience very generously and set the perfect role model.

I am very grateful to my supervisor Jan. Thank you very much for giving me the opportunity to come to Netherlands and carry out my research in the group. I remember the first time I arrived, you asked “how do you like the weather of Netherlands”. Now I must say it really rains a lot especially this spring yet the people here are very sunny. You are always very friendly, warm and ready to help. Your way of cheering people has very much encouraged me to go on and explore. Those two week meetings, your very logical thinking way enlightened very much my scientific thinking. You are always suggesting me with many opportunities of collaboration, discussions and conferences. I benefit a lot from your encouragement of going out of the research field I focused and exploring the outside.

I would like to extend my great appreciations to Prof. Roeland Nolte, thank you so much for your many valuable suggestions and advices during those group meetings.

Many many thanks also go to Dennis, Jordi, Yingfeng, Yongjun, loai, Zhipeng, Xiaofeng, Roger, Alaa, Jelle, Shauni, Toni, Marlies, Ruud, Emilia, Silvie, Joep, Britta, Petra, Dave, Saskia, Anika, Annika, Matthijs, Marcel, Nanda, Lise, Hailong, Jan, Mark and other colleagues from both wing 8 and wing 1. Dennis and Jordi, thank you for your kind help with the CPP synthesis and the whole peptide project. Yingfeng, thank you so much for so many joint collaborations. Yongjun, you know almost every field from chemistry, physics, economics and even Fashion! I hope you would really start your handbag designing business someday when you have time. Thank you so much for giving me nice and interesting answer each time I came up with a super weird question beyond our field. You are always a fun friend to play with and a good cook when visiting. Thank you for sharing your secrets on how to make a really delicious scallion pancake. Silvie, thank you so much for your efforts to introduce me to the polymersomes/nanoreactors and every detailed answer to my first year questions. Joep, many thanks go to you for teaching me how to carry out polymerization and let me touch my very first drop of polymer solution and to have a real feeling of polymer chemistry. I still remember the time that you wanted to

make sure that I learned everything and stayed late for my first polymerization reaction. Emilia, thank you for being a nice roommate on almost every conference we went to. Sorry for the time that I suddenly sat up, spoke to you in Chinese in the mid-night and startled you the first time we shared a room. Zhipeng, I owe many thanks to you for your discussions about my project. I remember that time you were startled by how much I try to achieve at one time and suggest me why not try from the most simple system. I am still very grateful for that suggestion. Xiaofeng, thank you so much for giving me so much ideas and direction choices in the beginning year of my PhD. You are also very generous in giving suggestions and sharing experiences and tips with us. Roger, I would like to express my appreciation for all the very timely emails you respond to my questions and I like very much your enthusiastic way of speech.

I also owe many thanks to other colleagues of the cluster. Min and Jing, thanks for so many laughters we had together in the cell culture room. Jose, I appreciate much your help with my starting the new cell lines.

Dear joyful Peter, thank you so much for always being a great help! I always think what Peter could not do, you are definitely engineer, accountant, chemist… I enjoy very much your funny jokes (sometimes I really thought it was real) and I will definitely miss that. Dear Jan Dommerholt, thank you for those contactings to make sure that I could get the chemicals/microplates in time. Dear Marieke and Desiree, thank you so much for the daily matters and kind help! I also owe my sincere thanks to many technicians and staff members for their warm helping during my PhD years. Thank you Liesbeth, Geert-Jan, Helene, Paul Peter van Galen and Paul white. I would not know what to do without these very nice people from general instrumentation, technical department telling me what is available, where to find the place for tailor made device(glass/metal), how to do the analysis…

Great thanks also go to my other colleagues Alain, Ashish! Thank you both for your many many contributions during the time we worked together. Your hardwork, intelligence, and enthusiasm for science really impressed me. I hope both of you would have a successful and fruitful research career. My acknowledgements also go to Peer, Hans, Sema, Pim, Wei, Hongbo, Maarten, Daniel, Paula, Onno, Max, Bao, Joan, Ying, Sara, Noel, Martin... Hans, thank you Hans and Sema, for appreciating my spicy food and sushi. Hans, I must say I was really considering starting a small food booth downstairs after you offered to start up the small business together (yet the share ratio you asked for was too high, I wouldnot earn after serious calculation). Pim, I really missed those table-top games evening, it is really fun! Pim, I also hope that you will continue on with your really amazing trials with Korean food and I really wish that I will see you on MasterChef in the future.

I would like to extend my aknowledgements to the collaborators at Radboud Institute for Molecular Life Sciences. Thank you Fang and Jiamian, I owe many thanks for the

collaboration project we did together on macrophage and electrospinning project. Mangala, Edyta, thank you so much for always being there to arrange and help with the fluovivo machines everytime that I suddenly need to measure.

Great thanks to my dearest Mama and Papa, thank you for your endless support and love!

ABOUT THE AUTHOR

Fei Peng was born on November 21th 1988 in Hengyang, China. In 2006 she enrolled in the Capital Medical University, China and studied chemical biology and pharmacy. Then she moved on to the school of pharmacy, Peking University in 2010. During her stay there, she carried out research on dendrimers as drug delivery vehicles. This project was performed under the supervision of Associate Prof. Xin Hu. After obtaining the master of science degree in 2013, she came to Radboud University Nijmegen to pursue her PhD in the Department of Bio-organic Chemistry. Under the supervision of Prof. Daniela A. Wilson and Prof. Jan C. M. van Hest, she focused on the development of supramolecular nanomotor systems for biomedical applications. The results of the research are described in this thesis.

LIST OF PUBLICATIONS

Peng, F. Tu, Y. F. Wilson, D. A. Micro/nanomotors towards in vivo application, *Chemical Society Reviews*, accepted.

Tu, Y. F.‡ **Peng, F.** ‡ Men, Y. J. Andre, A, van Hest, J. C. M. Wilson, D. A. Biodegradable hybrid stomatocytes nanomotors for drug delivery. *ACS Nano*, 2017, DOI: 10.1021/acsnano.6b08079 (‡ contributed equally as first author).

Peng, F. Deng, N. N. Tu, Y. F. van Hest, J. C. M. Wilson, D. A. Continuous fabrication of polymeric vesicles and nanotubes with fluidic channels. *Nanoscale*, 2017, DOI: 10.1039/C7NR00142H.

Peng, F. Tu, Y. F. Men, Y. J. van Hest, J. C. M. Wilson, D. A. Supramolecular adaptive nanomotors with magnetotaxis behavior. *Advanced Materials*, 2016, DOI: 10.1002/adma.201604996.

Peng, F. Tu, Y. F. Adhikari, A. Hintzen, J. C. J. Lowik, D. W. P. M. Wilson, D. A. Peptide-functionalized nanomotor as efficient cell penetrating tool. *Chemical Communications*, 2016, DOI: 10.1039/C6CC09169E.

Tu, Y. F.‡ **Peng, F.** ‡ Sui, X. F. Men, Y. J. White, P. B. van Hest, J. C. M. Wilson, D. A. Self-propelled supramolecular nanomotors with temperature-responsive speed regulation. *Nature Chemistry*, 2016, DOI: 10.1038/NCHEM.2674 (‡ contributed equally as first author)

Tu, Y. **Peng, F.** Adawy, A. Men, Y. J; Abdelmohsen, L.K.E.A.; Wilson, D. A. Mimicking the cell: Bio-inspired functions of supramolecular assemblies. *Chemical Reviews*, 2016, 116, 2023-2078.

Men, Y. J. **Peng, F.** Tu, Y. F. van Hest, J. C. M. Wilson, D. A. Methods for production of uniform small-sized polymersome with rigid membrane. *Polymer Chemistry*, 2016, 7, 3977-3982.

Men, Y. J. Peng, F. Wilson, D. A. Micro-/Nanomotors via self-assembly. *Science Letters Journal*, 2016, 5, 219.

Peng, F. Tu, Y. van Hest, J. C. M., Wilson, D. A. Self-guided supramolecular anticancer drug loaded polymeric nanomotors with chemotactic behavior. *Angewandte Chemie International Edition*, 2015, 54, 11662-11665.

Abdelmohsen, L. K. E. A. **Peng, F.** Tu, Y. Wilson, D. A. Micro- and nano-motors for biomedical applications. *Journal of Materials Chemistry B*, 2014, 2, 2395-2408.

Peng, F. Gao, P. C. Li, X. T. Hu, X. Acid sensitive doxorubicin-PAMAM with tumor targeting profile. *Journal of Chinese Pharmacuetical Sciences*, 2013, 1, 81-88.